2013

Positron Emission Tomography for Pre-Clinical Sub-Volume Dose Escalation

Christopher Bass
Virginia Commonwealth University

Positron Emission Tomography for Pre-Clinical Sub-Volume Dose Escalation

Christopher Paul Bass

Bachelors of Science, Randolph-Macon College 2008

Advisor: Andrei Pugachev

Doctor of Philosophy, Radiation Oncology

Virginia Commonwealth University

Richmond, Virginia

August 2013

Acknowledgements

The author wishes to thank and acknowledge others for their contribution to the completion of this work. Dr. Scott Robertson, Dr. Joseph Moore, Nicholas Anderson and David Hoffman for providing peer review of the document and discussion on the initial stages of the research. Dr. Andrei Pugachev, Dr. Geoffrey Hugo and Dr. Jeffrey Siebers for providing guidance and advice throughout the completion of this research. Dr. Sundaresan Gobalakrishnan for assistance in the acquisition of multiple PET/CT data sets and Jun He, who performed collection of biological data and immunofluorescence imaging. Lastly the author would like to acknowledge his fiancée Elizabeth O'keefe for multiple peer reviews and moral support.

Table of Contents

Table of Figures

Abstract:

POSITRON EMISSION TOMOGRAPHY FOR PRE-CLINICAL SUB-VOLUME DOSE ESCALATION

By Christopher Paul Bass

A thesis submitted in partial fulfillment of the requirements for the degree of Doctor of Philosophy in Medical Physics at Virginia Commonwealth University.

Virginia Commonwealth University, 2013

Major Director: Andrei Pugachev, Staff medical physicist, Radiation Oncology

Purpose:

This dissertation focuses on establishment of pre-clinical methods facilitating the use of PET imaging for selective sub-volume dose escalation. Specifically the problems addressed are 1.) The difficulties associated with comparing multiple PET images, 2.) The need for further validation of novel PET tracers before their implementation in dose escalation schema and 3.) The lack of concrete pre-clinical data supporting the use of PET images for guidance of selective sub-volume dose escalations.

Methods and materials:

In order to compare multiple PET images the confounding effects of mispositioning and anatomical change between imaging sessions needed to be alleviated. To mitigate the effects of these sources of error, deformable image registration was employed. A deformable registration algorithm was selected and the registration error was evaluated via the introduction of external fiducials to the tumor. Once a method for image registration was established, a procedure for validating the use of novel PET tracers with FDG was developed. Nude mice were used to

perform in-vivo comparisons of the spatial distributions of two PET tracers, FDG and FLT. The spatial distributions were also compared across two separate tumor lines to determine the effects of tumor morphology on spatial distribution. Finally, the research establishes a method for acquiring pre-clinical data supporting the use of PET for image-guidance in selective dose escalation. Nude mice were imaged using only FDG PET/CT and the resulting images were used to plan PET-guided dose escalations to a 5 mm sub-volume within the tumor that contained the highest PET tracer uptake. These plans were then delivered using the Small Animal Radiation Research Platform (SARRP) and the efficacy of the PET-guided plans was observed.

Results and Conclusions:

The analysis of deformable registration algorithms revealed that the BRAINSFit B-spline deformable registration algorithm available in SLICER3D was capable of registering small animal PET/CT data sets in less than 5 minutes with an average registration error of .3 mm. The methods used in chapter 3 allowed for the comparison of the spatial distributions of multiple PET tracers imaged at different times. A comparison of FDG and FLT showed that both are positively correlated but that tumor morphology does significantly affect the correlation between the two tracers. An overlap analysis of the high intensity PET regions of FDG and FLT showed that FLT offers additional spatial information to that seen with FDG. In chapter 4 the SARRP allowed for the delivery of planned PET-guided selective dose escalations to a pre-clinical tumor model. This will facilitate future research validating the use of PET for clinical selective dose escalation.

Chapter 1: Introduction

This dissertation focuses on establishing pre-clinical methodologies for in-vivo validation of the use of PET in treatment planning; specifically, the utility of Fluorodeoxyglucose (FDG) PET imaging in guiding dose escalation to a tumor sub-volume. Additionally pre-clinical methods for examining the potential of novel PET tracers to provide additional information to FDG are established. This introduction provides background physics and summary of how PET imaging could be used to increase tumor control in radiation oncology.

1.1.Lack of Improvements in Cancer Survival Rate

Since the 1970s there have been many advances in the field of radiation therapy. Primary imaging modalities have changed from 2D radiographic x-rays to combined modality PET/CT tomographic images. Planning methodologies have improved from manually-placed forward calculated plans to inverse plans in which the desired dose can be specified by the dosimetrist and the plan is created and optimized by a computer. Beam collimation has shifted from the primary jaw collimation to multi-leaf collimators allowing for intensity modulation and more conformal beam shaping [1]. Despite all of the advances in the fields of radiation therapy and medical imaging since the 1970s, overall patient survival rates show only a small improvement [2], [3]. In head and neck cancer specifically, Pulte et al. showed that from 1982 to 2006 survival rates for head and neck cancer have gone from 52.7 % to 65.9% [4].

Reexamining the historical development of radiation therapy it becomes obvious that the one aspect that has never changed is the goal of treatment planning; to deliver a homogeneous radiation dose to a gross tumor volume (GTV) defined on anatomical imaging. This approach accounts only for the spatial extent of the GTV while neglecting the underlying tumor biology [5], [6], [7]. Histopathological studies of both patient tumor specimens [5], [8] and small animal tumor xenograft models have shown that tumors exhibit highly heterogeneous microscopic biological features (figure 1).

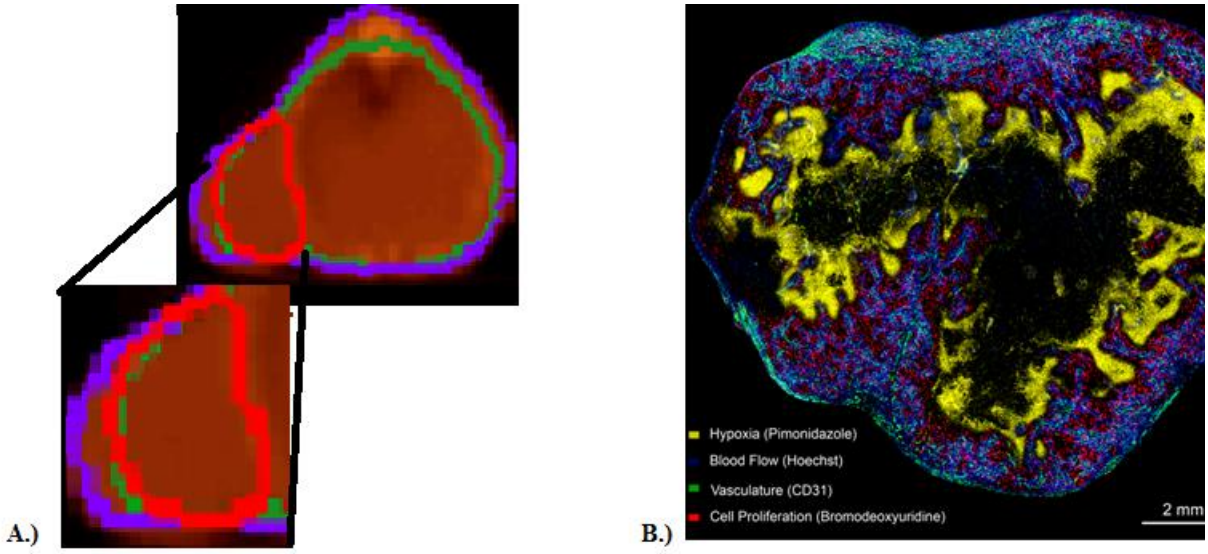

Figure 1 :A.) A CT image of a FaDu head and neck depicting a mass of homogeneous density. B.) An immunofluorescence image of a FaDu tumor which shows the heterogeneity of the underlying tumor biology. Both images are from a mouse xenografts model.

Unfortunately, while histological analyses can yield information regarding tumor biology, it is an invasive procedure and cannot be carried out prior to radiation therapy. In 2000, Ling et al. proposed to use PET imaging of multiple different novel PET tracers to gain insight into underlying tumor biology non-invasively. Ling proposed that cancer survival rates could be improved by treating each tumor with a heterogeneous dose distribution sculpted to the specific radio-resistances of tumor cells as derived from PET images [9].

1.2.Introduction to PET physics

Unlike computed tomography (CT) and magnetic resonance imaging (MRI), which are principally utilized for anatomical imaging, positron emission tomography (PET) is a functional imaging modality which provides visualization of underlying molecular processes within the biological tissues. For PET imaging, a positron-emitting imaging probe, a chemical compound labeled with a positron emitter, is injected into the subject and is taken up more avidly by tissues expressing specific biological properties. Following the uptake period, the patient is scanned using a dedicated scanner which uses scintillation crystals aligned in a ring around the patient. When the radio-nuclide decays, a positron is emitted. The positron travels through the tissue for some distance within tissue, eventually coming to rest and annihilating with an electron (figure 2).

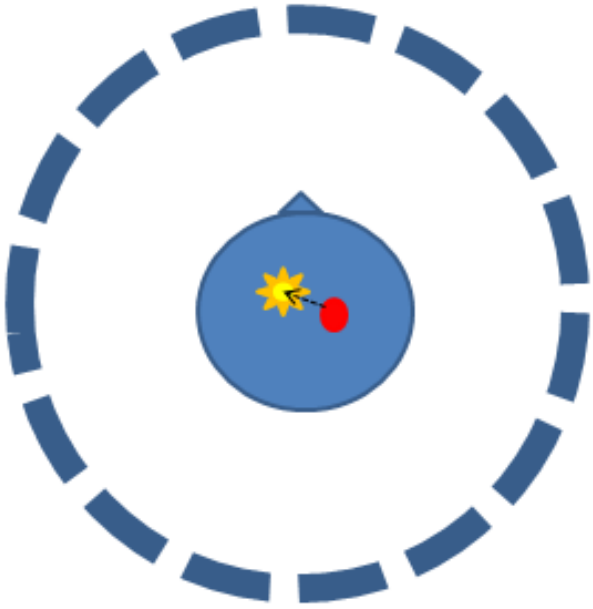

Figure 2: Depiction of a positron emitter (red) emitting a positron (< - - -) which annihilates with an electron ( )

The positron-electron system produces two nearly parallel-opposed 511 KeV gamma rays. When the scintillation crystals detect two coincident 511 KeV gamma rays, a single positron annihilation event is registered between the two detector crystals. After detection of the two gamma rays, a line between the detectors along which the annihilation event occurred, known as the line of response, is identified (Figure 3).

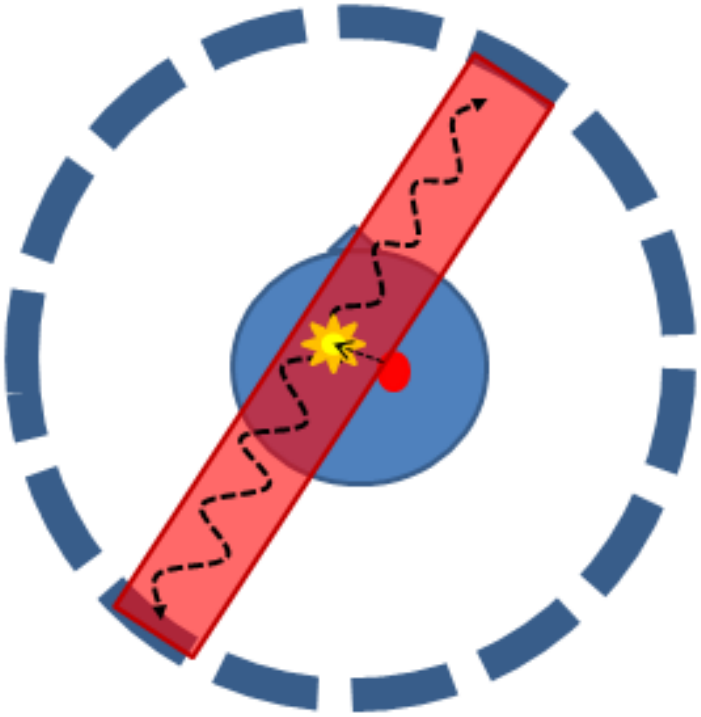

Figure 3: Depiction of a hypothetical line of response (red line) resulting from the detection of two co-incident 511 KeV photons ( )

After the detection of many annihilation events, the various lines of response are used to estimate the distribution of PET tracer within the image space.

While PET imaging does provide insight into the underlying biological properties of tissues it suffers from a lower resolution when compared with anatomical imaging modalities such as CT or MRI. Resolution-limiting factors can be broken into two categories, intrinsic

factors, factors that are inherent to PET imaging, and extrinsic factors, factors that are specific to scanner design. The three for the most dominant resolution limiting factors for PET imaging are positron range in tissue, the emission of non-parallel opposed gamma rays and scintillation detector related factors [10], [11].

Positron range in tissue is an intrinsic limitation of PET resolution. Due to the fact that positrons emitted from 18F travel some distance in tissue before annihilating, the system is detecting the position of the positron annihilation event, which is at best an approximation to the location of the positron-emitting probe. This phenomenon introduces a resolution-limiting uncertainty into the location of the tracer. Another intrinsic resolution-limiting factor is the non-parallel opposed emission of gamma rays. In creating a line of response it is assumed that the positron and electron pair were at rest when annihilation occurred, resulting in two gamma rays emitted parallel opposed to one another because of conservation of momentum. It is possible, however, for the positron to annihilate with an electron without coming to complete rest. In this case the two gamma rays emitted from the annihilation event will not be parallel opposed; resulting in a line of response that is not representative of the location the annihilation occurred (Figure 4).

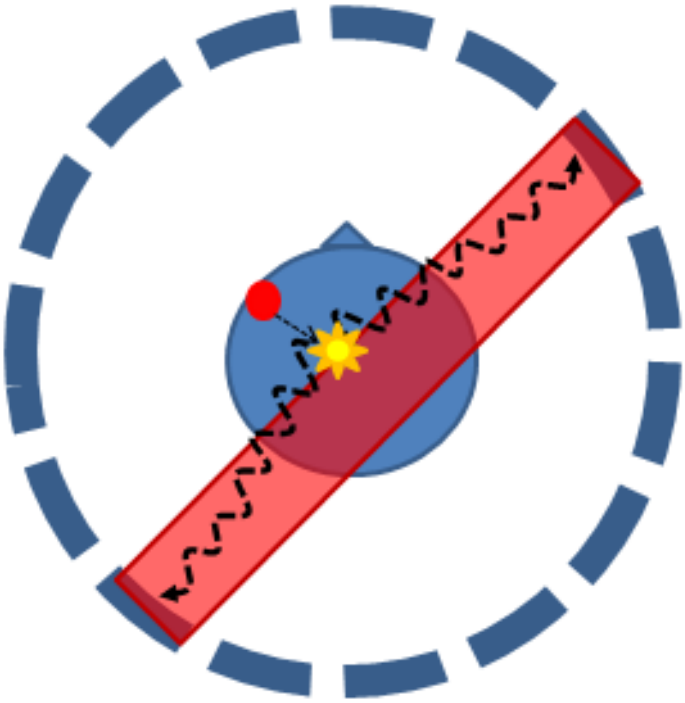

Figure 4: Figure depicting the emission of non-parallel opposed photons and resulting skewed line of response which is not representative of the position of the annihilation event.

Resolution is also limited by extrinsic, machine specific factors, such as the choice of detectors of the PET system. Due to the fact that scintillation detectors cannot be infinitely small, there is a resolution limitation introduced by the finite size of the detector crystal. Due to the design of most commercial PET systems, the gamma rays incident upon a detector are localizable only within the size of the detector. In other words, if two gamma rays were incident upon the same detector but 1 cm apart from one another, both incidents would be spatially indistinguishable. As a result the line of response drawn from two detectors is limited in width by the size of the detector (Figure 5).

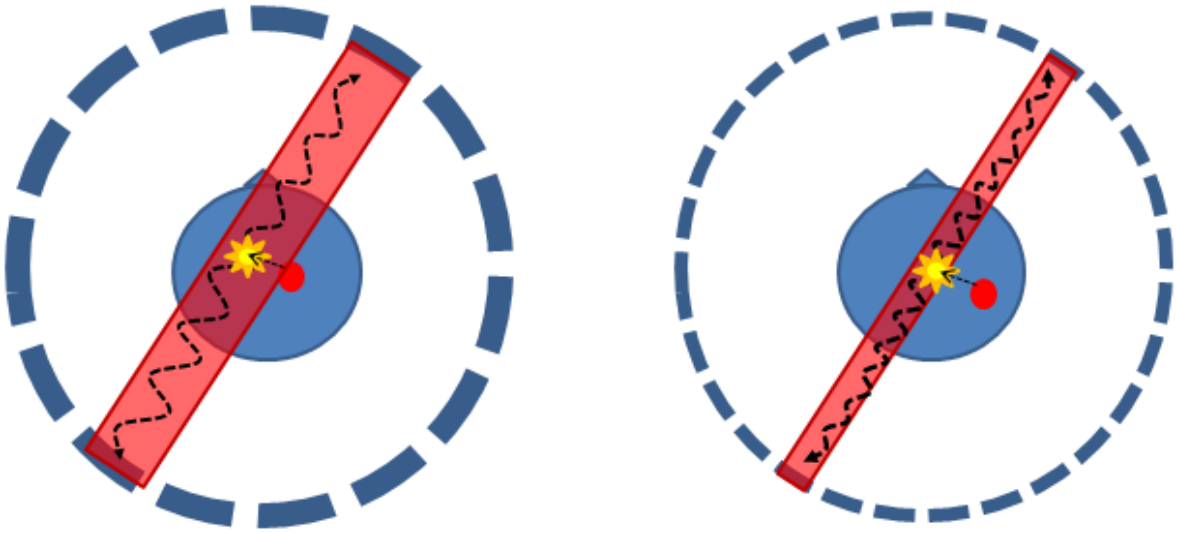

Figure 5: The effect of detector size on the intrinsic line of response modeled with a large detector (Left) and a small detector (Right)

In addition to these resolution-limiting factors, random coincidences and scatter within tissue can also introduce uncertainties into PET images. Random coincidences occur when two separate annihilation events produce gamma rays and the system misregisters the arrival of two gamma rays originating from two different annihilation events as coincident gamma rays from a single event (Figure 6).

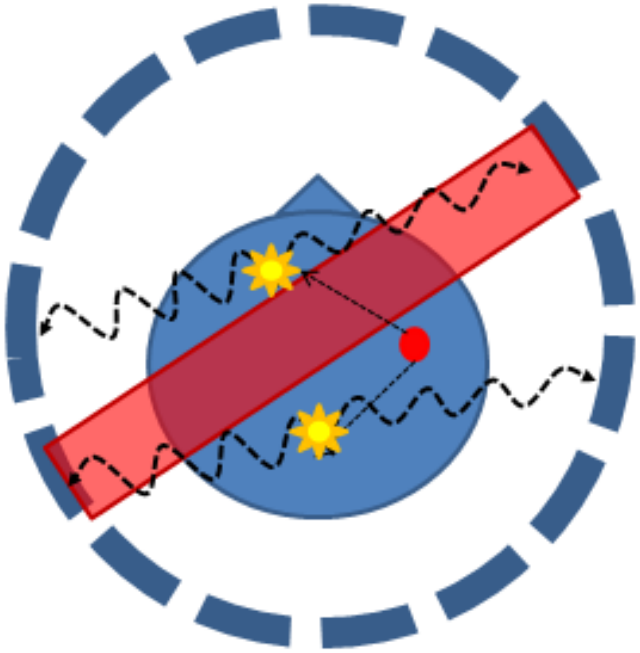

Figure 6: Figure depicting the occurrence of a random coincidence (photons from two separate annihilations registering as the same event) and the resulting line of response which is not representative of the position of either annihilation

This misregistration results in a line of response that does not correspond to either of the annihilation events, introducing uncertainty into the results of imaging.

Gamma rays from a single annihilation event can also be scattered either in tissue or in the detectors themselves. In tissue, gamma rays in the 511 KeV energy range can collide with electrons in the tissue. After collision, the incident gamma ray transfers some fraction of its energy to the electron and the gamma ray is deflected by an angle theta given by the equation for Compton interaction:

$$\lambda' = \frac{h}{m_e c}(1 - \cos\theta) + \lambda$$

Where h is Planck's constant, m_e is the mass of an electron, c is the speed of light, theta is the angle the gamma ray scatters, lambda is the original gamma ray energy and lambda prime is the new energy of the gamma ray after collision. In order to limit the effects of noise and scattering events, PET systems have a specific energy window for coincidence detection. An energy window is a specific range of energies that are accepted as products of annihilation events. Only accepting incident gamma rays with energy of exactly 511 KeV can minimize the effect of these scattering events but could also potentially increase the time needed to complete a scan (Figure 7).

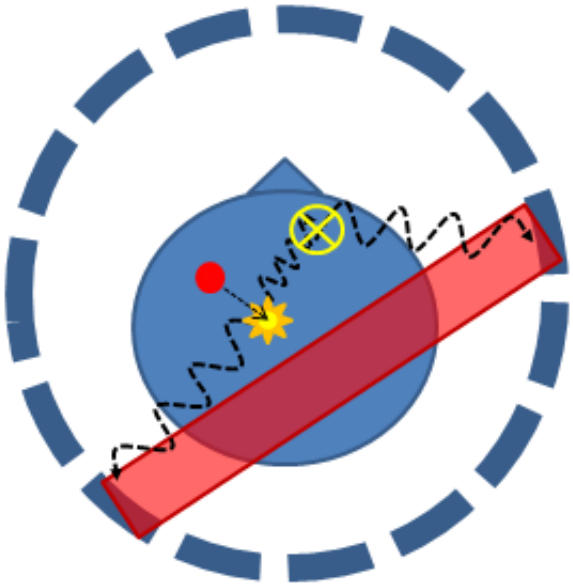

Figure 7: Figure depicting a scattering event of a single photon (⊗) and the resulting line of response which is not representative of the position of annihilation event

Overall, these effects result in a resolution of approximately 5 mm for clinical whole body patient scanners and approximately 1.5 mm for dedicated small animal scanners [10]. Despite the limited resolution compared to anatomical imaging modalities like CT, PET provides a non-invasive method for gaining insight into the underlying biological processes in tumors prior to treatment. Pairing PET with CT anatomical imaging allows for these biological processes to be localized within the resolution of the PET scan.

1.3.Current uses and limitations of PET and Molecular Imaging in the clinic

Outside of clinical trials, most clinics exclusively use ^{18}Fluorine-Fluorodeoxyglucoe or FDG, which is a glucose analogue. Tissues exhibiting high glucose metabolism do not differentiate between glucose and FDG and subsequently uptake more FDG than normal tissues. Once in a cell, however, FDG is phosphorylated and becomes trapped due to a missing hydroxyl group needed for glycolysis. In this way FDG can be accumulated over time. The differences in amount of FDG retention in cells produces the image contrast seen in PET images.

Differences in glucose metabolism from cell to cell in tumors have been shown to have a variety of causes including: the presence of hypoxia, cells with high proliferation rates, and local differences in tumor cell density [7]. Consequently, FDG is not a specific tracer of any one biological phenomenon. Rather, it represents a complicated interplay of multiple biological phenomena within the tumor. This increase in glucose metabolism and consumption does not necessarily more aggressive disease or higher risk of recurrence. Due to its non-specificity to any one underlying biological property, PET images are typically used in the clinic as binary indicators of lymph node involvement as sub-clinical and metastatic disease.

Despite its limitations, multiple studies suggest that FDG has potential for other clinical uses such as therapy response monitoring, primary tumor delineation, a basis for treatment planning, and making clinical decisions on treatment modality using tracer uptake [12], [13], [14]. However, it has also been suggested that FDG be combined with tracers of other biological phenomena by labeling substances other than Fluorodeoxyglucose with ^{18}F. It has been suggested that performing multiple PET studies using different novel PET tracers would overcome the limitations of FDG alone and provide additional information useful for clinical decision making [9].

1.4.Potential for using multiple PET tracers for radiotherapy guidance

1.4.1. The rationale for multiple-tracer PET imaging

In order to achieve an improvement in tumor control it has been suggested that PET imaging be used to escalate doses to CT defined GTVs [9], [15]. The current strategy for dose escalation

using PET imaging is to escalate dose to the entire tumor as it is defined on FDG PET imaging [16], [17], [18], [19]. The rationale behind the escalation of the entire tumor is that on PET-positive volumes are significantly smaller than CT defined GTVs. This smaller target volume has been shown to allow for the delivery of a slightly escalated dose to the tumor before organs at risk reach their dose-limiting constraints [16], [17], [18], [19]. As previously stated, however, FDG is not indicative of increased radioresistance within a tumor. Increasing the dose to the entire FDG-avid tumor is likely to be excessive and normal tissue structures will reach toxicity sooner than with smaller escalation sub-volumes.

Ling et al. suggested the implementation of a multiple-tracer PET imaging protocol that would allow for the identification of the specific biological heterogeneities within a tumor, for example areas of hypoxia or proliferating cells [9], [15]. Hypoxic cells and proliferating cells both exhibit distinctly different radiosensitivities. During radiotherapy well oxygenated cells experience increased damage due to the production of free radicals. Hypoxic cells, however, do not experience any of this increased cellular damage when irradiated and as a result are more radioresistant. Rapidly proliferating cells also exhibit different radiosensitivity than normal cells. Cells undergoing rapid proliferation are more likely irradiated in M and G2 phases of the cell cycle. In these phases it is much easier to achieve double strand DNA breaks and as such these cells are typically more sensitive to irradiation. Chemical compounds such as fluorothymidine and fluoromisonidazole can be labeled with radioactive fluorine and used to visualize areas of increased cellular proliferation and hypoxia respectively. By identifying these sub-populations of tumors cells, Ling proposed to create a map of the underlying tumor biology prior to treatment. This map of biological features could then be used to modify the dose prescription in such a way as to treat the underlying biological and radiological properties of

each individual tumor [9]. Identifying these specific sub-populations of cells prior to radiation therapy would allow physicians to escalate doses to areas of increased risk of recurrence rather than to the entire tumor unilaterally and could decrease toxicity associated with escalated doses.

1.4.2. The need for validation of novel PET tracers

The use of non-FDG PET tracers to obtain multiple PET images representative of different biological features of interest, is still an area of continuing research. The benefits of using multiple PET tracers to acquire information that would benefit clinical practice have yet to be evaluated in detail [15], [20]. While the biological mechanisms of uptake are different between FDG, FLT and F-Miso, for example, biological factors such as vascularization of the tumor and necrosis can potentially limit the benefit of using multiple tracers. Large areas of necrosis and poorly vascularized tumors can cause the distribution of tracers to be limited within the tumor. When these tracers are then imaged, the limited resolution of PET combined with the limited tracer distribution within the tumor could result in very similar tracer distributions. To this end, it is important to ensure that the effects of tumor morphology do not force tracers of different biological properties to exhibit the same spatial distributions. This is not an easy phenomenon to examine, however, because changes such as physical mispositioning of the subject and anatomical changes confound the ability to compare the true spatial distributions of PET tracers within tumors. Prior to attempting further validating of novel PET tracers, a methodology must be set to remove the effects of these confounding factors.

1.5.Specific Aims of the research

In order to achieve better tumor control and patient survival rates Ling et al. suggest that the underlying biological features of a tumor need to be taken into consideration when creating a treatment plan. Specifically, the radioresistances of cells within the tumor should be determined and dose should be assigned accordingly. The specific aims of this dissertation discuss the tools and methodologies needed to perform biologically-guided dose escalations using a pre-clinical model. Chapter 2 discusses the difficulties associated with comparing images acquired at different points in time for use in treatment planning, and the role deformable image registration can play in alleviating mispositioning errors and changes in anatomy between imaging sessions. Specifically, deformable registration algorithms are validated for the accuracy needed to deform small animal pre-clinical PET images. Chapter 3 uses the deformable registration protocol explored in the previous chapter to compare the spatial distribution of FDG to the distribution of other novel tracers. For the purposes of establishing the methodology ^{18}F-Fluorothymidine (FLT), a novel PET tracer of proliferation, is compared with FDG. The co-localization of the two tracers is analyzed to determine the utility of FLT in conjunction with FDG. Chapter 4 outlines a protocol for planning and delivering PET-guided dose escalations on a small animal model using the Small Animal Radiation Research Platform (SARRP), image-guided small animal irradiator. As an illustration, a pilot study comparing FDG-guided dose escalation and an arbitrarily placed dose escalation was also carried out to test the efficacy of this protocol.

Chapter 2: Validation of deformable registration algorithms for PET images

2.1.Background and Rationale

Differences in the spatial distributions of PET tracers can be attributed to three main causes: Changes caused by deforming internal anatomy, changes caused by physical mispositioning and changes in the underlying biological processes governing tracer uptake. The goal of most imaging used in radiation oncology is to observe differences in anatomy caused by positioning or anatomical changes. The comparison of functional images, however, is confounded by these sources of change. In order to properly compare functional medical images acquired at two different times it is important to have an objective methodology for removing effects of changes induced by anatomical and positioning differences (Figure 8).

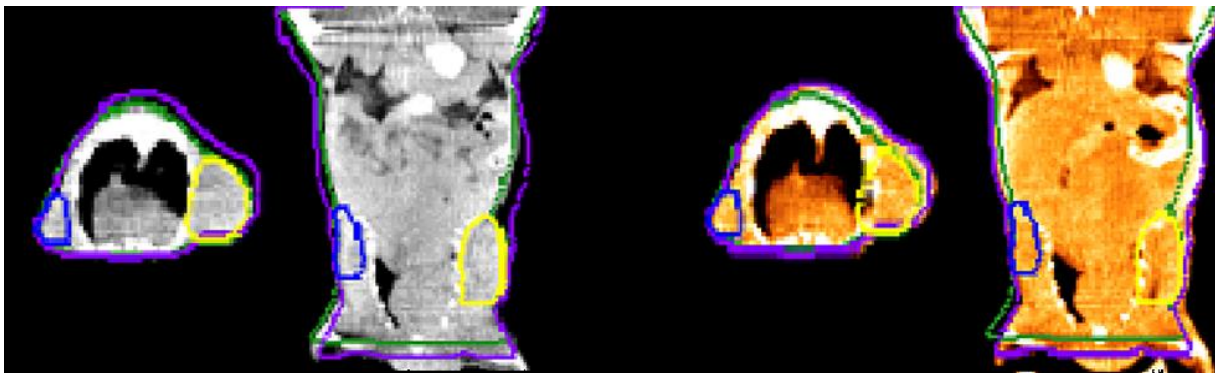

Figure 8: A comparison of Two CT images of the same animal on consecutive days depicting the changes in anatomy and positioning from day to day. The green contour signifies the first day's body contour, purple the body contour on the second day. The yellow and blue contours represent the first day tumor positions.

2.2.Deformable Image Registration

Deformable image registration can serve as a method for alleviating the effects of errors in positioning and anatomical changes. Image registration is an iterative process in which an estimated transformation is determined by the results of the optimizer and the transformed image is compared to the fixed image. If the fixed and transformed images meet a defined similarity criteria and the optimizer can find no better result, then the image is considered registered from the program's point of view.

There are three main components of any deformable registration algorithm [23], [24], [25]:

1. **The deformation model**, which determines how the moving image can be changed
2. **The cost function**, which is a measure of agreement of the transformed image registration and the fixed image set
3. **The optimizer**, which is the methodology used to iteratively minimize or maximize the cost function until an acceptable value is reached

These components are further described in the following sections.

2.2.1. The Deformable Model

The registration model determines the physical properties and constraints on the registration. A registration model must be selected for the appropriate application for the scale of the changes needed: large global changes or small local changes. Some of the most

commonly discussed models include Basis-spline (B-spline) and the diffusion-based Demons' [23], [24], [25], [26]

2.2.1.1. Basis spline models

The two major spline-based models are the thin-plate spline model and the B-spline model. The B-spline model defines a grid of control points on both images. The resolution of this control point grid is defined by the user, with sparse grids resulting in large-scale deformations and finer grids contributing to small local changes. The deformable transform in three dimensions is represented as a series of cubic piecewise polynomials which are centered on the control points [24], [25]. The deformation is determined by summing the polynomials across small local regions of the image. The weighting at each of these control points controls the magnitude of deformation in the image. It is important to note, however, that with a large number of control points, changing the coefficient of a single control point will have a limited range of influence and will not affect the global image [23], [24], [25].

2.2.1.2. Demons' deformation models

Thirion et al. proposed to approach the problem of image registration as a diffusion problem in their 1998 paper [27]. In the paper, Thirion describes the fixed image as being a semi-permeable membrane. The moving image is considered a deforming grid and is pulled into the semi-permeable fixed image by hypothetical forces at each of the grid control points. Thirion defines the process of deforming medical images in four steps.

1. A control point called a demon is placed at the center of each voxel in the moving image

2. The "Demon's force", v ,responsible for the displacement for each point in the moving image is calculated using the optical flow equation for instantaneous velocity:

$$v = \frac{(m-s)\nabla s}{(\nabla s)^2 + (m-s)^2}$$

Where m is the intensity of the point in the moving image and s is the intensity of the point in the fixed image

3. A free form deformation is then established by repeating the calculation of the Demon's force for each voxel in the moving image

4. A Gaussian smoothing function is used to smooth the free form deformation over the entire image to regularize the transformation

This general algorithm formulation is known as the Demons' deformation algorithm [27].

2.2.2. Cost Functions

The cost function of the algorithm is a mathematical expression which is designed to maximize the similarity between the fixed and transforming images. The optimizer of the algorithm iteratively attempts to minimize the value of the cost function to achieve the best registration. In general the cost functions compare either pre-defined physical landmarks in the images or the gray scale image intensities. Landmark-based algorithms use manual or automatically selected features that are present in both images to drive the registration. This is beneficial because anatomical landmarks ensure that the image registration remains anatomically correct. In contrast, image registration algorithms using intensity-based cost functions only take into account the grayscale intensities of the pixels of the image without knowledge of anatomical structures. Without any sort of constraints on the transformation, it would be possible for an intensity-based algorithm to exacerbate the misalignments of structures.

Common cost functions include sum of squared distances, correlation coefficient methods and mutual information. Mutual information, the cost function implemented in this dissertation, involves maximizing the concordance of areas with similar gray scale intensities. Klein et al. describe the mutual information cost function as:

$$C\ (\mu) = -\sum_{m \in Lm} \sum_{m \in Lf} P(f,m)x\ \log_2\left(\frac{P(f,m)}{P_F(f)P_M(m)}\right)$$

Where μ is defined as a vector containing the b-spline coefficients and is a function of the intensity of the moving image, I_m, and the intensity of the fixed image, I_f. L_m and L_f are intensity bins of the moving and fixed images, p is defined as the joint probability function of the fixed and moving images and P_F and P_M are the probability of the fixed and moving images. Additional details about the Thevenaz method are described in Klein's paper [29]. Another method of computing the mutual information metric seen in the review paper by zitova et al. defines MI as:

$$MI = H(M) + H(F) - H(M,F)$$

Where H(M) is the entropy function of the moving image, H(F) is the entropy function of the fixed image set and H (M,F) is the joint entropy function of both image sets [22]. Both of these methodologies have been tested and are commonly used for multimodal image registration. In a study of similarity measure efficiency Boyd et al. determined that mutual information was ideal due to its ability to register images of different anatomical modalities and was efficient enough for quick image registrations.

2.2.3. Optimizers

There are a great number of optimization methods available for implementation in deformable image registration. The optimizer used throughout the most of this dissertation is a steepest gradient descent approach. The steepest gradient descent algorithm attempts to minimize the cost function by finding the greatest rate of change in the B-spline coefficients to drive the cost function iteratively towards a minimum value quickly. Klein et al. describes the process mathematically as:

$$\mu_{k+1} = \mu_k + a_k g(\mu_k)$$

Where μ_k is the previous set of B-spline coefficient parameters selected by the optimizer, a_k is a factor limiting the step size that the algorithm may take and $g(\mu_k)$ is the derivative of the cost function with respect to the current set of B-spline parameters [29]. This process is performed until the cost function reaches a local minimum. In a review of optimizers by Maes et al., the steepest gradient descent optimizer was suggested to be the easiest to implement optimizers [30]. This optimizer doses, however, suffer from the fact that the local minimum of the cost function is not always going to be the global minimum. This implies that is could be possible for better solutions for the registration than what algorithm is returning at any given time. In addition, Klein et al. found the steepest gradient descent method to function more slowly than other methods [29]. Despite this the gradient descent method used in this research performed registrations in less than 3 minutes on average depending on parameters selected. It may be possible to improve this time by implementing other optimization schemes.

2.3.Algorithm selection

The application of deformable image registration to pre-clinical biological images requires an algorithm which can handle primarily large shifts in anatomy due to mispositioning and anatomical change of structures. In the context of this work, the selected deformation algorithm must also be efficient enough to be used while a mouse is under anesthesia and positioned on the machine for treatment.

The BRAINSFit algorithm (http://www.slicer.org/slicerWiki/index.php/Modules:BRAINSFit) was chosen for registration of small animal CT images. This algorithm is an implementation of the B-spline algorithm available through Insight Tool Kit (http://www.itk.org/), a popular open source library of image registration tools. The BRAINSFit implementation of the B-spline algorithm uses a mutual information-based cost function with a gradient descent optimizer. The BRAINSFit algorithm was selected for testing for the following features:

1. Modeling of soft-tissue flexibility and elasticity due to elastic deformations
2. The inherent smoothness and regularity of b-spline deformations when compared to Demon's deformations [29]
3. Mutual information's utility for registering images of different modalities and applicability to different severities of deformation [31]
4. The established accuracy of the ITK B-spline implementations using mutual information in pre-clinical imaging [31], [32], [33], [34], [35]
5. The ability to control the scale of the deformation by changing the grid size

In order to use deformable registration to compare pre-clinical PET images, it is important to ensure that the selected algorithm can produce results with sufficiently small errors. For the purposes of this research, algorithmic errors must be small enough for two applications:

1. For the comparison of two different PET images, the algorithm must be accurate to within the inherent PET resolution of 1.5 mm
2. For treatment planning of small (approximately 3 to 5 mm) sub-volume dose escalations, the algorithm must display errors smaller than the size of the intended escalation

The stricter requirement of registration errors being less than 1.5 mm was used as the benchmark for a good algorithm. Not only should the algorithm be accurate but it must also be capable of performing registration in soft-tissue regions with few visible landmarks. Previous validation studies have focused on well-defined landmarks or areas of specific anatomical structures [31], [32], [33], [34], [35]. Within tumors, however, there is usually very limited soft tissue contrast In order to successfully use deformable registration to recover the proper biological distributions of PET tracer, the algorithm must be capable of accurate registration even in these less distinct areas. In order to evaluate the performance of these algorithms in low contrast regions, landmarks must be introduced to these regions without affecting the performance of the algorithm. The following methods and materials discuss this process.

2.4.Methods and Materials

2.4.1. Tumor model

Nude mice inoculated with human tumor xenografts were used for the measurement of the errors in deformable registration algorithms. Tumors were implanted on the left and right flank of the mice and averaged 1 cm in the longest dimension. Prior to the implantation of any object within the tumors, the animals were sacrificed. All Imaging procedures were performed as quickly as possible to assure that rigor mortis had not set in during positioning of the sacrificed mouse on the scanner.

2.4.2. Marker implantation

One of the difficulties evaluating algorithms for registering tumors with CT anatomy is that the performance of the algorithm within the tumor is difficult to evaluate. Tumors contain no internal landmarks on CT scan for the algorithms to use for registering the images; there are also no landmarks with which to verify accuracy. In order to validate the ability of different deformable registration algorithms to generate proper deformation vector fields (DVFs) inside these tumors, landmarks had to be introduced into the tumor for the purposes of measuring registration errors.

The landmarks used as fiducials in this work were selected from a large number of different materials. As the primary purpose of these markers is to provide contrast against soft tissue, the ideal marker should have an effective Z higher than 6, the approximate effective Z of soft tissue. However, high Z materials can be excessively attenuating at lower diagnostic imaging energies. In the case for small animal studies, images as low as 65 kV are used for imaging. At these lower energies the problems of marker artifact are exacerbated greatly compared to normal human imaging. A set of pilot studies was carried out to determine a material that produced good

contrast with soft tissue but did not create large density-related artifacts. In order for the marker to be visible on CT but leave minimal artifact, the ideal effective Z of the material should not only be greater than that of soft tissue but also less than that of bone, approximately 20. For these pilot studies, varying gauges of Aluminum (Z = 13), Copper (Z = 29) and stainless steel ($Z_{eff} \approx Z_{iron} = 26$) were implanted into phantoms comprised of beef to qualitatively assess the artifacts induced by the marker. Copper and stainless steel were used, despite their high Z, because incredibly thin gauge (sub millimeter) wires were available and were still somewhat rigid compared to the aluminum alternatives. It was hypothesized that these thin gauge wires would not be excessively attenuating because of their small diameter, despite their high density. Figure 9 shows the results of one imaging these different markers in a slab of beef.

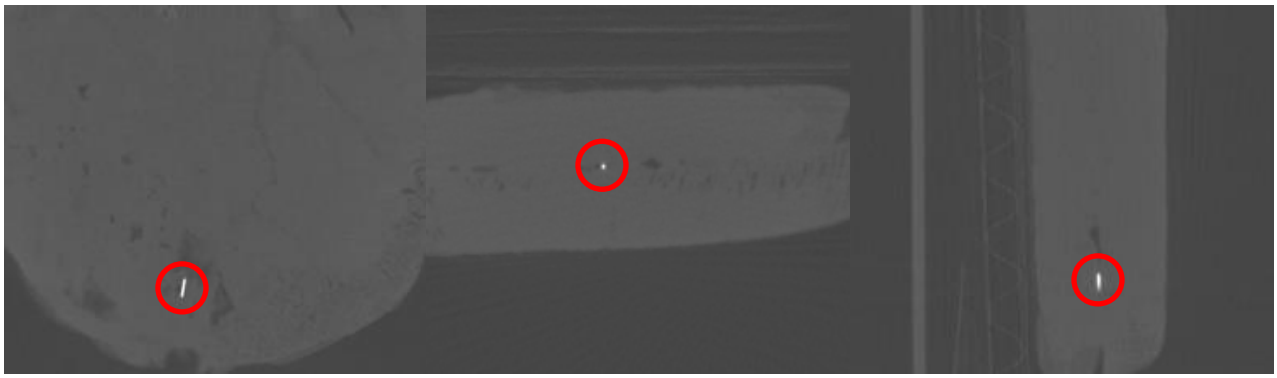

Figure 9: A 28 gauge steel marker (circled in red) shown on a CT of a phantom causing little artifact

A thin gauge composite copper magnet wire (diameter < 0.321 mm) was determined to give the best contrast with soft tissue with an acceptably small amount of metal artifact in the images. Further details on the selection of appropriate marker material can be found in Appendix I. After the best marker in the beef phantom images was determined a similar experiment was conducted using a sacrificed mouse to verify the marker's performance in the small animal tumor model. After selecting the marker, sacrificed mice bearing subcutaneous xenografts were implanted with three pre-constructed markers of approximately 3 mm in length. Implantation was done using a modified pre-loaded 25 gauge needle with a 28 gauge steel obdurator threaded through the needle. Once implanted, the markers create a landmark on CT images inside the tumor. The thin gauge of the wire allowed the markers to be imaged without leaving extreme image artifacts (Figure 10).

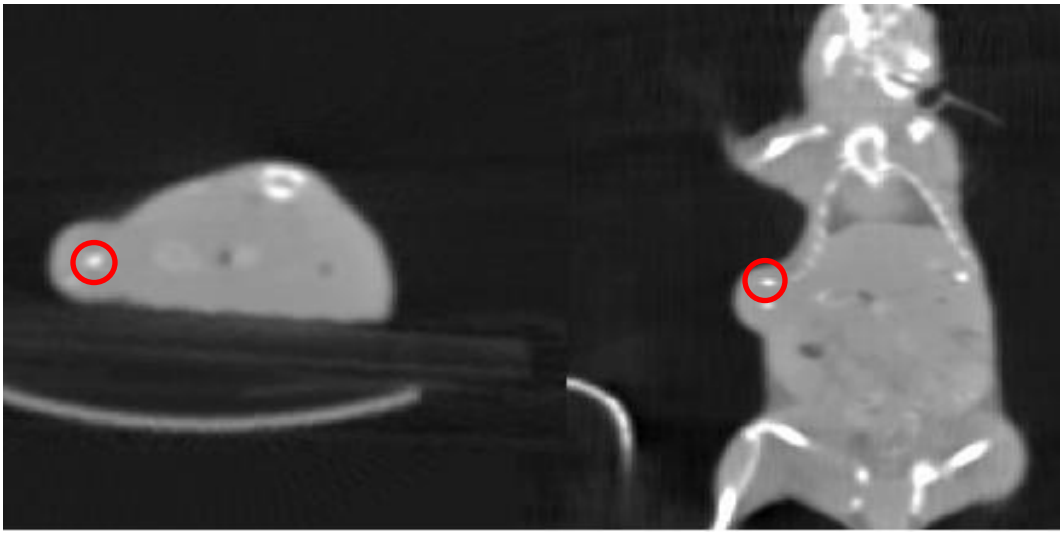

Figure 10: CT image of a sacrificed mouse with implanted metal markers (shown in red circles)

2.4.3. Small animal PET imaging

In order to compare the position of the markers, CT images were acquired using a Siemens Inveon small animal PET/CT/SPECT. Each mouse was positioned feet-first, prone on an animal specific pad (Figure 11) and imaged for 5 minutes. Animals were imaged at .5 mA and 75 kV as

Figure 11: An animal specific pad used for repositioning

described in the protocol for all of our small animal experiments. The animal's body was contoured and the tumors were marked on the pad for purposes of repositioning. After imaging, the mouse was removed from the scanner and repositioned on the animal specific pad. As the mouse had already been sacrificed, the subcutaneous tumor could be intentionally subjected to mispositioning and deformation prior to re-imaging. The animals were then imaged a second time with the same imaging protocol.

2.4.4. Image post-processing to remove markers

CT images were segmented in Slicer 3D, an open source environment for medical image analysis. All markers were manually contoured using the slicer 3D segmenting tools. In order to achieve an unbiased image registration, the CT markers were removed using post processing

prior to deformable registration. In order to facilitate the marker removal, large ROIs of tumor tissue were contoured in areas of the tumor containing no marker or artifact. The contours and images were then imported into MATLAB where the ROIs were used to generate a histogram of pixel intensities representative of tumor tissue free from artifact or marker. Values were then selected from the markerless tumor tissue histogram and used to overwrite the image intensities within the contour of the marker. The histogram for the new marker-free images was then compared against the markerless tumor histogram to ensure that the post-processed image did not contain any artifacts prior to saving the post-processed images for deformation (Figure 12)

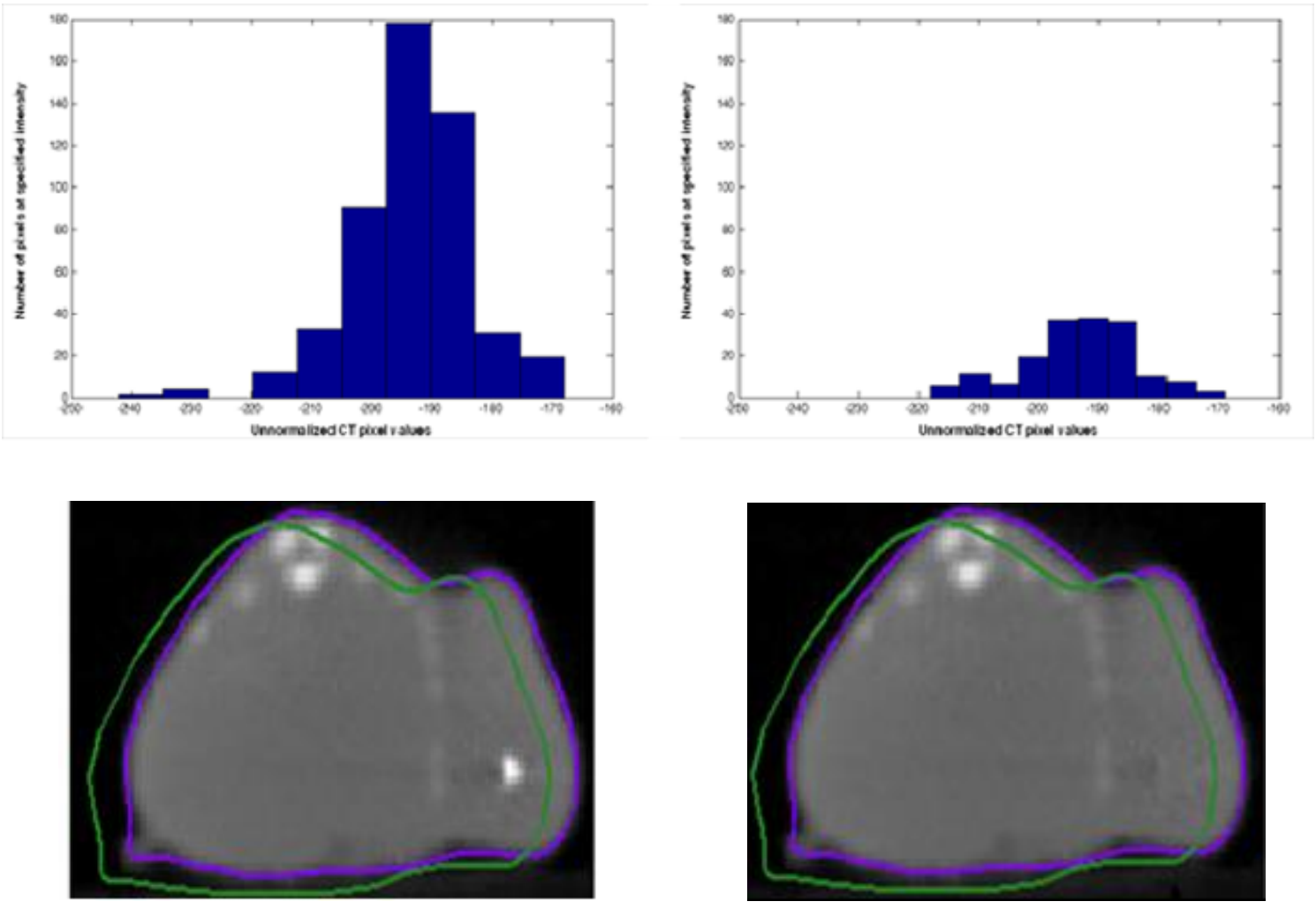

Figure 12: TOP: The histogram of a large region of normal tumor tissue on CT (Left) and the histogram of values used to replace the CT marker randomly selected from the normal tissue ROI histogram (right). BOTTOM: a CT image containing an implanted marker (Left) and the same CT image after post-processing to remover the marker (Right).

2.4.5. Deformable Image registration and registration parameters

Prior to image registration there were multiple parameters which needed to be optimized in order to achieve a successful image registration. In order to ensure the process was unbiased, region of interest options used for image registration were set to the auto-generate option, which contours the body of the animal using the greyscale contrast between the image background and the surface of the animal. Since the density of soft tissue remains constant between both imaging sessions, the histogram matching options were also used to improve the registration between the two CT images. The different initialization options available in slicer were examined to determine their utility in small animal CT-to-CT registrations. The non-manual registration options in slicer failed because the Inveon PET/CT and the SARRP have different fields of view which limit the extent of the animal shown in each image set. Since the extent of the animal imaged is different in each image set, initialization measures which are derived from anatomical geometry like center of mass measurements will not provide good initialization As a result, manual rigid initialization was used prior to all registrations. The two main parameters tested to ensure the best registration were the grid size and the number of samples. Selection of a grid size determines the number of control points on the image for use in deformation. The control points for this b-spline algorithm are uniformly spaced and define the points at which the hypothetical forces deforming the image are acting. Typically the more grid points introduced the more fine, local deformations are employed. This can lead to irregular transform causing unnatural transformed images. The fewer grid points used, the more global the deformation. The program guidelines suggest a starting grid size sub-dividing the image set into 14, 10, 12 segments respectively. In order to determine a suitable grid size for these deformations various grid sizes

were used to deform markerless images. Figure 13 shows the results of applying grid sizes of [14, 10, 12], [10, 6, 8] and [18, 14, 16].

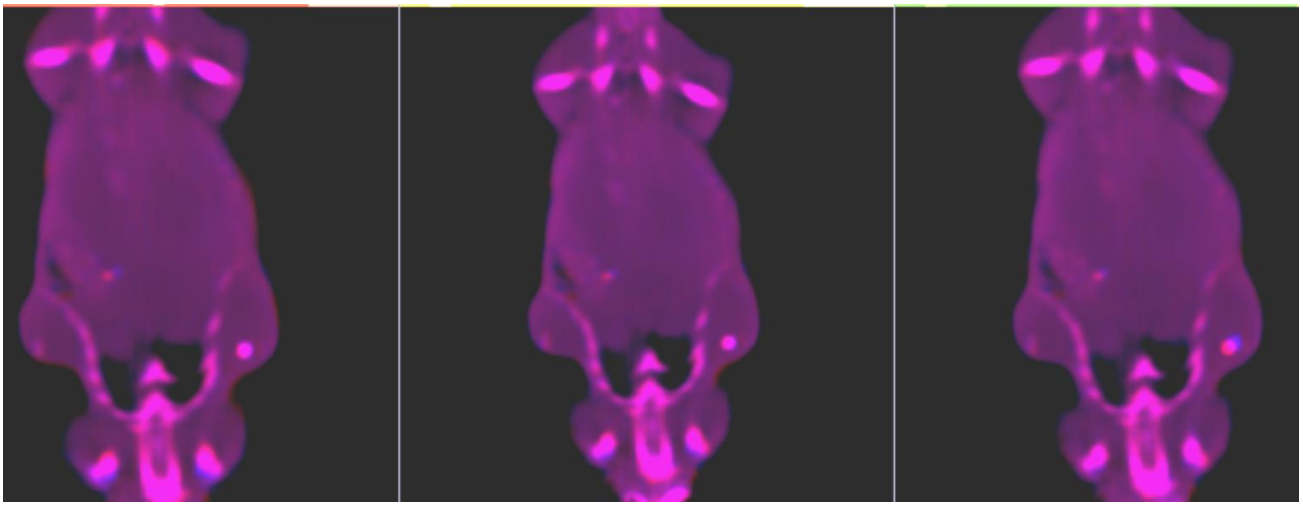

Figure 13: An overlay of deformed image (blue) and the fixed image (red) showing the effects of changing grid sizes of [10,6,8] (left) , [14,10, 12] (center) and [18,14,16] (right)

The smaller grid subdivisions seemed to align the marker reasonably but overall bony alignment suffered. The larger grid subdivisions performed well on the bony anatomy but registration of smaller structures like the markers suffered. The suggested default of 14, 10, and 12 seemed to provide a good middle ground between bony structure registration and marker registration. Ultimately the default grid size of 14, 10, and 12 was used as it produced the most successful deformations.

In addition to the grid size used for deformation, the number of samples is also an important determining factor to how well the deformation performs. The number of samples determines the number of voxels for which the mutual information between the two images is

compared. In other words, the number of samples selected directly affects both the global accuracy and the time required for computation. Slicer recommends a default value of 100,000 samples. The images used in the deformations were 384 x 256 x 256 and 256 x 256 x 256, implying that there were 16,777,216 voxels in the smaller of the two images. While 100,000 samples seem low when compared to the total number of voxels, the speed of the deformation is critical for the application of the algorithm to a small animal model where deformation must be performed while the animal is anesthetized. The time required for deformation for sample sizes ranging from 50,000 samples to 1,000,000 samples was recorded and the deformation errors were quantified. Figure 14 shows the effects of sample sizes of 100,000, 50, 000 and 1,000,000 on the quality of the deformations.

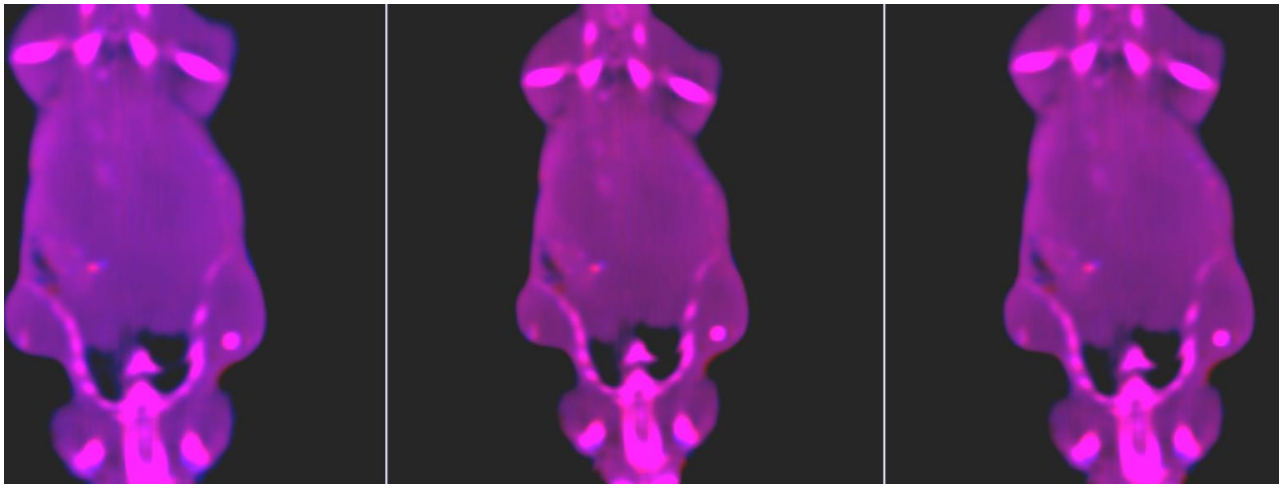

Figure 14: Overlay of deformed image (blue) and the fixed image (red) depicting the effect of changing the number of samples from 50,000 (left) to 100,000 (middle) to 1,000,000 (right)

The suggested 100,000 sampling points gave acceptable registrations of both the markers and the bony anatomy in 2.6 minutes. Using fewer sampling points (50,000) reduced registration time to 51.34 seconds but the bony anatomy accuracy and the accuracy of the marker registration suffered. Increasing the number of sampling points to 1,000,000 increased computational time

significantly to 15.1 minutes and did not show a noticeable improvement in registration quality. For the purposes of image registration while the animal is anesthetized on the SARRP, a sample size of 100,000 was well within the 1.5 mm desired accuracy and was faster than 5 minutes.

After determining a suitable set of parameters for image registration, the post-processed marker-free CT images were used as input into the registration algorithm. By using these images, the B-spline transform is free of the influence of the implanted markers. The unbiased B-spline transform can then be applied to the original moving image containing the markers. Using this methodology, the images containing markers can be registered to one another without the registration being driven by the presence of the markers (Figure 15).

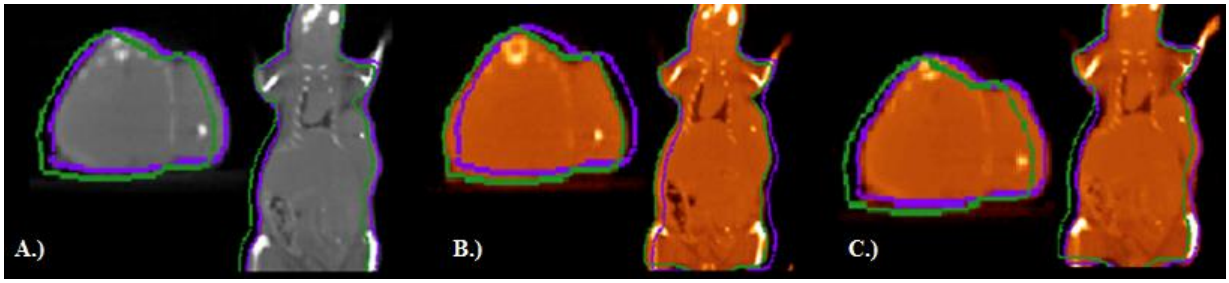

Figure 15: the difference in CT images from day 1 (A.), day 2 (B.) and the deformed day 2 image (C.). The green contour represents the second day's body contour and the purple represents the first day's body contour.

2.4.6. Analysis of marker displacements

After image registration, the images containing markers were imported into Slicer 3D. The images were overlaid with one another and set to different color maps to allow for easier analysis. In order to ascertain the error inside the tumor, the maximum displacement between the marker borders was determined by evaluating the displacement in fractions of pixels using slicer 3D measurement features and then multiplying by the pixel size to convert to an approximate distance (Figure 16). In this way, the largest displacement in millimeters was determined for the XY, YZ, and XZ planes were determined for each marker.

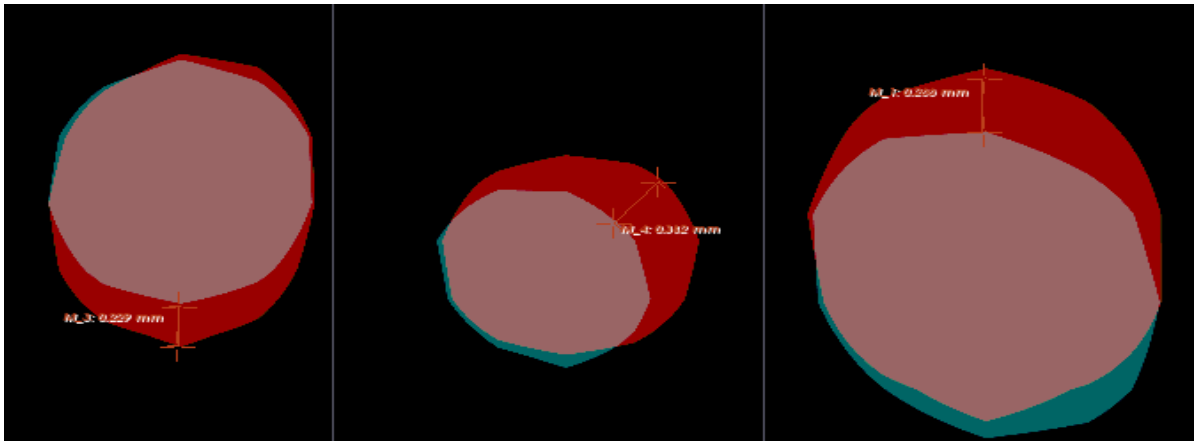

Figure 16: Axial (left), sagittal (middle), and coronal (right) planar displacements for a single marker

2.5.Results

The errors in transformations produced by the BRAINSFit implementation of the ITK B-spline algorithm in Slicer 3D were smaller than the resolution of PET and allowed for an objective image registration. The measurement of the differences in marker position for the BRAINSFit yielded maximum displacements in any plane below 2 CT voxels or 0.67 mm (Figure 17).

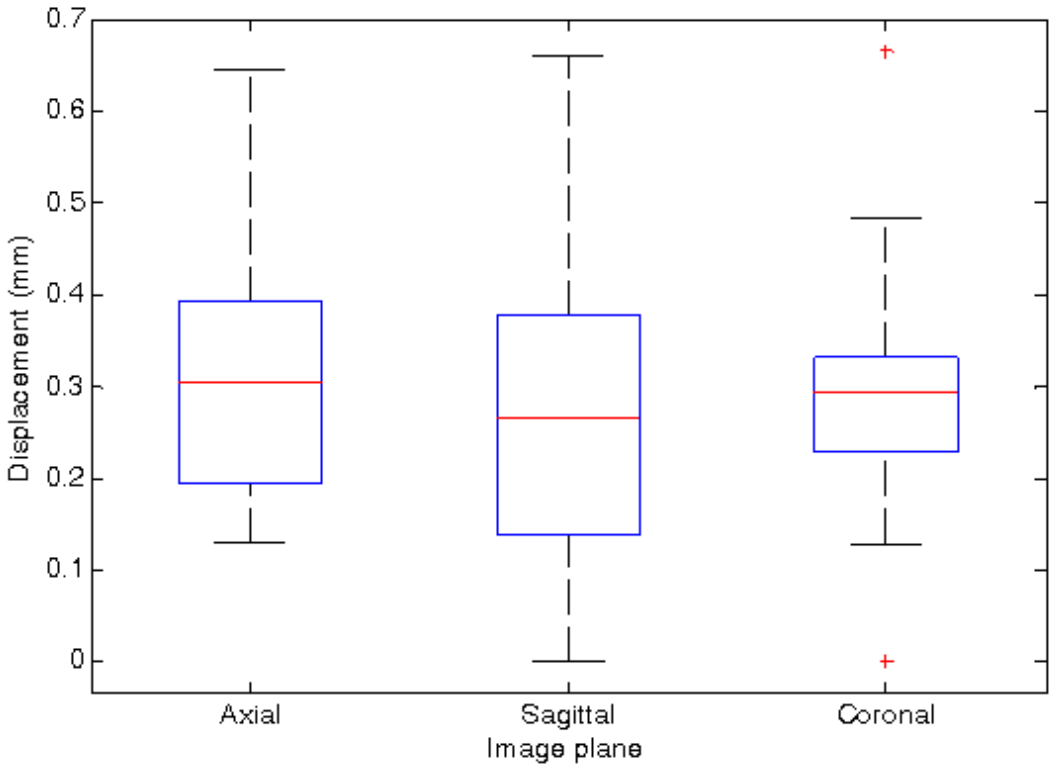

Figure 17: Figure 16: Axial (left), sagittal (middle), and coronal (right) planar displacements for a single marker

This is well below the nominal small animal PET voxel resolution of approximately 1.5 mm. 61 percent of all markers in the Slicer analysis were aligned with a maximum error of less than one CT voxel (0.335 mm) and 90 percent of all markers were aligned within 1.5 CT voxels (0.5025 mm).

2.5.1. Error Analysis

2.5.1.1. Contouring and displacement measurement errors

In order to ensure the error in marker registration was sufficiently small, errors associated with measuring the marker displacement were also analyzed. In order to determine the observer contouring error, the same sets of markers were blindly contoured multiple times and the reproducibility analyzed. In a similar manner, a single observer used the Slicer 3D measurement tools to estimate displacement for a single marker multiple times and the error was determined. Due to the incredibly small size of the markers, less than two voxels in the largest dimension, the contouring of the markers was done with a 1 pixel brush and was very reproducible. The marker size, however, was under two voxels in the largest dimension. As such, the 1 pixel brush was only capable of estimating the marker location within .37 mm. The final displacement of the markers was performed by using the measurement tools in Slicer 3D to assess the marker differences manually. Repeated measurements of markers yielded maximum measurement deviation of .03378 mm and an average variance of .000188 mm showing good reproducibility.

2.5.1.2. Analysis of B-spline transformations

To further validate that the marker registration process was being carried out properly, the transforms in the vicinity of the markers was analyzed. If the markers are properly masked there should be reduced deformation in the area of the markers. In order to verify this visually, B-spline deformable transforms were generated registering two images containing markers and the

same two images without markers. The transforms were then applied to a 3D binary grid to see the effect of the transforms. Figure 18 shows the overlays of the two transformed grids overlaid with the transformed images and a comparison image between the two transformed grids.

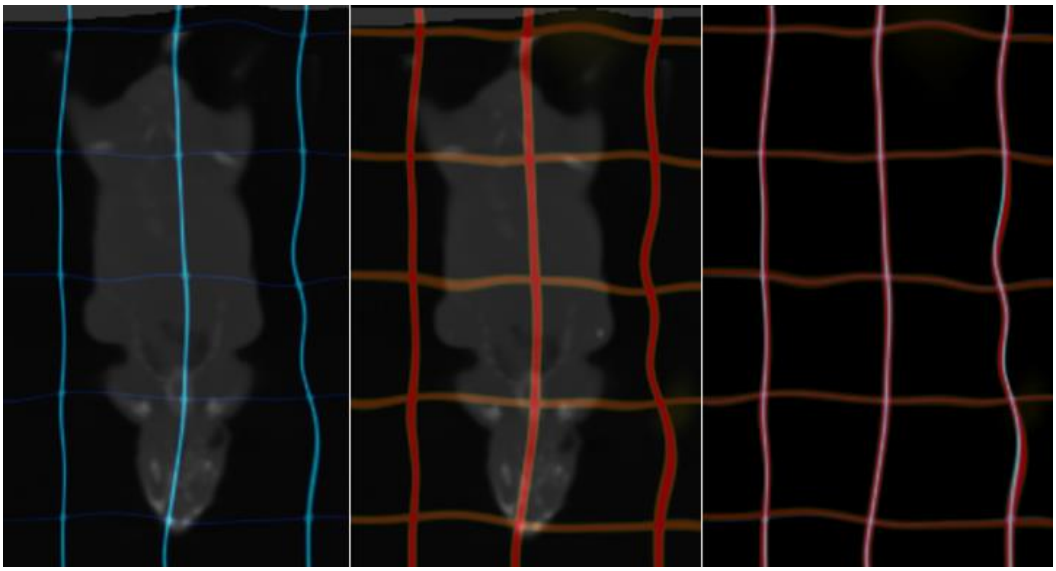

Figure 18: Image showing the effect of the markers on the B-spline transform. The markerless transform is shown in blue (left), the marker-driven transform is shown in red (middle) and an overlay of the two transforms (right).

Given the size of the grids for deformation the markers are hypothesized to have little effect on the image. Upon inspection of the transforms there was little difference between the marker and markerless transforms. The transform produced with the markers present showed slightly more deformation in the area of the tumor. This supports the idea that the markers have been removed as there is less deformation in the area of the tumor when the markers are removed. Additionally any problems with marker removal are mitigated by the fact that a sparse grid is used.

2.6.Conclusions

The combined error of the B-spline transformations and measurements of marker deviation was shown to be well below the inherent PET resolution of 1.5 mm. Given these results, the Slicer3D's BRAINSFit deformation algorithm was determined to be acceptable for use in small animal CT-CT image registration. In addition, two PET/CT data sets can be deformably registered by registering the accompanying CT images with the Slicer BRAINSFit package and applying the transforms to the PET image. As the errors in registration accuracy are smaller than resolution of the PET image, errors in the PET image will be sub-voxel and should not have a detrimental effect on data analysis of two registered PET images.

Chapter 3: In-vivo analysis of the spatial distributions of ^{18}F-FDG and ^{18}F-FLT

3.1.Background

FDG PET imaging is used clinically to evaluate nodal involvement for tumor staging and grading. Due to the possibility of FDG uptake in areas of inflammation and the desire to target halmarks of increased tumor aggression, it has been suggested that other novel PET tracers could be useful in radiation oncology. Fluorothymidine (FLT), a tracer of cell proliferation, is one of many novel PET tracers that have been suggested as a potential clinical tracer for PET imaging. This chapter discusses the previous attempts at validating novel PET tracers and the need for the validation of the spatial distribution of novel PET tracers. FLT is compared to FDG to illustrate the efficacy of the proposed methodologies.

FLT was introduced to the clinic as a drug for HIV treatment; however the necessary concentrations of the drug proved to be toxic. Shields et al. conceptualized the use of a smaller, non-toxic concentration of the compound tagged with radioactive flourine-18 for use as a novel PET tracer of proliferation [36]. FLT is structurally similary to thymidine but lacks one of the hydroxyl groups nessecary for full integration into DNA. As it is not a direct analogue of thymidine it becomes trapped within cells after phosphorylation by thymidine kinase one (TK1). The level of TK1 present in a cell is proportional to the phase of the cell cycle a cell is currently in with the highest concentrations of TK1 present during proliferation [36]. Given the relationship between FLT and TK1, and the relationship between TK1 and cellular proliferation, an increase in FLT uptake has been demonstrated to correlate with increased proliferation [36], [37].

In 2002 Toyohara et al. published their validation of FLT as a marker of cell proliferatin. 22 cell cultures of different tumor cell lines were exposed to FLT for 60 minutes. After the uptake period cells were removed from the FLT solution. Liquid scintillators were then used to acquire counts for FLT uptake of each sample. Flow cytometry was used to determine the stage of the cells in each culture. A correlation analysis was then performed between the FLT uptake and number of cells in S-phase of the cell cycle. Toyohara found that FLT uptake showed a strong positive correlation with the total number of cells in S-phase [38].

Muzi et al. carried out an in-vivo kinetic analysis of FLT uptake in lung cancer in 2005. Patients were imaged sequentially using FLT PET over a period of 120 minutes in order to acquire FLT uptake at different time points. In addition to PET imaging performed at multiple time points, the ammount of radiotracer in the blood was assayed by venous blood sampling throughout the same 120 minute period. After imaging, specimens were ressected and mounted for immunoflourescene staining and histological analysis. Specimens were stained for Ki-67, a cell proliferation index. Standardized uptake value or SUV was used to characterize the uptake of FLT within the tumor at each time point. SUV was calculated as the normalization of activity in the tumor to the injcted dose and the patients body weight. The fluctuation of FLT levels in the blood was also determined for different time points using blood sampling assays performed. Muzi then correlated the change in levels of FLT in the bloodstream to both Ki-67 index and FLT SUV. In addition, FLT SUV was also compared to Ki-67 index for each patient as well. Muzi et al. reported an incredibly strong spearman rank correlation of .92 between FLT SUV and fKi-67 labeling index and concluded that FLT was preferentially uptaken in proliferating tissues [39].

In 2010, Troost et al. carried out a histopathologic validation of FLT. Seventeen patients with oral cavity carcinoma were imaged using FLT PET following a 60 minute tracer uptake period. After imaging, tumors were resected for histological analysis. PET images were normalized to the injected tumor activity and the patient body weight. Troost et al. looked specifically at the maximum and mean SUV values within the tumor. Prior to aurgical ressection of the tumor, iododeoxyuridine was injected intravenously. Three different blocks of each tumor were mounted for sectioning. After sectioning, tumors were stained for iododeoxyuridine, Ki-67 and TK-1 expression. TK-1 images were visually assesed by two researchers blinded to the PET results. Statistical correlation analysis of SUV maximum, mean, TK-1 expression, Ki-67 index and iododeoxyuridine staining was performed. Troost concluded that FLT could be a useful tool in patient response monitoring to therapy but required further validation before clinical use [40].

Zhang et al. published a pre-clinical analysis of FLT uptake in xenograft tumor models in 2012. FLT micro PET/CT was performed after a tracer uptake period between 60 and 80 minutes. In addition, Bromodeoxyuridine (BrdU), an extreinsic marker of cell proliferation for histological analysis was injected. FLT PET SUV values were then compared to BrdU, Ki-67 and TK-1 staining of sectioned tumors. Zhang saw a positive correlation between FLT SUV and [^{3}H] thymidine. While Zhang saw an agreement between TK-1 expression and FLT uptake, not all cells expressing increased TK-1 levels exhibited increased FLT uptake. Ultimately, Zhang concluded that FLT could be a useful clinical tool but would require more careful validation [41].

Since the original publications by Shields et al. FLT, has been thouroughly validated as a tracer of proliferation using ex-vivo, in-vivo and histological analyses. It has been shown, however, that FLT alone may not be sufficient as a stand-alone tracer for PET imaging due to its

low uptake compared to FDG [14], [42], [43]. The exception to this occurs in brain lesions where FDG does not perform well [44]. In general, it has been suggested that FLT's primary use may be as a tracer for use in conjunction with the information provided by FDG [45], [46], [47]. Specifically, it has been suggested that FLT and other novel PET tracers can be used to treat underlying features of tumor biology. Prior to attempting multiple-tracer image guidance of radiotherapy it is important that the tracers are thouroughly compared to one another.

In 2004, van Waarde et al performed a study using FLT to distinguish between clinical disease and inflammation in a small animal model. Animals were inoculated with a subcutaneous flank xenograft and inflammation was also induced using an injection of turpentine. After establishing the tumor and inducing inflammtion, animals were imaged using FDG and FLT. Visual comparison and comparison of SUV values of both image sets were performed. Ultimately Van Waarde reported better contrast between normal tissues and high uptake regions for FDG PET images. FLT, however, did not show evidence of inflammation that was present in the FDG images [43].

In 2005, van Westreenen carried out a comparative study of FDG and FLT uptakes in ten patients with esophogeal cancer. FDG was allowed a 90 minute uptake period and FLT was allowed a 60 minute uptake period prior to scanning. After imaging, tumors were ressected and sectioned. Sectioned tumors were stained with Hematoxylin and eosin (H&E) for mophologic features and with Ki-67 for cell proliferation. The mean and maximum SUV values were calculated for both tracers and compared to the histological analysis. Van Westreenen observed that FDG was able to detect all primary cancers while FLT alone missed two of the ten cases. Quantitatively, the max and mean SUV values between FDG and FLT were used to compare the

two tracers. Van Westreenen concluded that FLT was not suitable to be used as a stand alone tracer in the clinic [48].

Also in 2005, Chen et al. examined the differences between FLT and FDG for use in gliomas. Twenty five patients were initially imaged with FDG and then imaged again with FLT on the following day. All scans were dynamic PET scans acquired over a period of 30 minutes. In addition to PET imaging, specimens were resected and stained for Ki-67. For the purposes of analysis, PET images acquired over the 30 minute timeframe were summed and the mean SUV of the highest 20% of voxels and SUV max were calculated. FLT and FDG SUV values were compared using wilcoxon statistical test and were also compared with Ki-67 labelling indices. Ultimately Chen concluded that FLT was a more suitable clinical tracer for high-grade gliomas. Herrmann et al. conducted a very similar study of patients with gastric cancers in which very similar results were observed. FLT was shown to be more sensitive that FDG for gastric tumors [49].

Hoshikawa et al. carried out a comparison of FDG and FLT in 43 head and neck cancer patients in 2011. In a procedure similar to the previously described methods, patients were imaged using FDG and FLT PET on back to back days. The mean and maximum SUV values were calculated for both tracers. Hoshikawa found that the contrast between normal tissues and disease was better in FDG images than in FLT images. Quantitative analysis between FDG, FLT and sectioned tumors stained for Ki-67 was performed using the mean and maximum SUV values. From the analysis Hosikawa concluded that FLT was as sensitive as FDG for head and neck cancers [50].

While all of these studies have compared the efficacy of FDG and FLT at segmenting tumor volumes, the only major quantitative comparison has been through mean and maximum SUV values. All of the aforementioned approaches neglect the spatial distributions of the two tracers in favor of assigning tumors a single numerical quantifier. While this approach can validate the ability of FLT to discern between FDG uptake in tumors and in areas of inflammation it is insufficient validation for using multiple tracers to plan therapy treatments. Despite the biological uptake mechanisms of novel PET tracers, poor vascularization and areas of necrosis limit the availability of the tracer to the tumor and have an equal effect on all PET tracers. The effects of these features could potentially overshadow the mechanisms of biological uptake and force both tracer distributions to be similar. To this end it is important to determine that a novel PET tracer contributes additional information to the information gained through FDG PET imaging. As previously mentioned, the effects of mispositioning and anatomical changes confound the ability to compare tracer distributions. Bowen et al. have attempted to circumvent this by analyzing only spontaneous canine tumors of the nasal cavity [bowen]. These tumors are largely rigid and do not deform between imaging sessions leading only to rigid translations. This does not mimic most clinical cases in which internal structures can shift and deform on a daily basis. In order to circumvent the confounding effects of deformations between imaging sessions, sequential scans performed over two separate days can be deformably resgistered and analyzed to determine the value of FLT as a tracer to be used with FDG in a small animal model.

3.2.Methods and Materials

3.2.1. Establishing tumor lines

Human head and neck tumor xenografts were used for the imaging and comparison of in-vivo PET tracer spatial distributions. Nude mice were inoculated with FaDu or SQ20B tumor cells in the left and right shoulders. Xenografts were allowed to grow for 25 days on average prior to imaging. Two tumor lines, FaDu and SQ20B were used in order to compare the effect of two vastly different tumor morphologies on tracer distribution. FaDu tumors tend to be fast growing and exhibit large necrotic cores. The FaDu tumor line also exhibits very compartmentalized biological features with defined regions of hypoxia and proliferation. In contrast, SQ20B tumors tend to exhibit a slower growth and the biological features are more difficult to define (Figure 19)

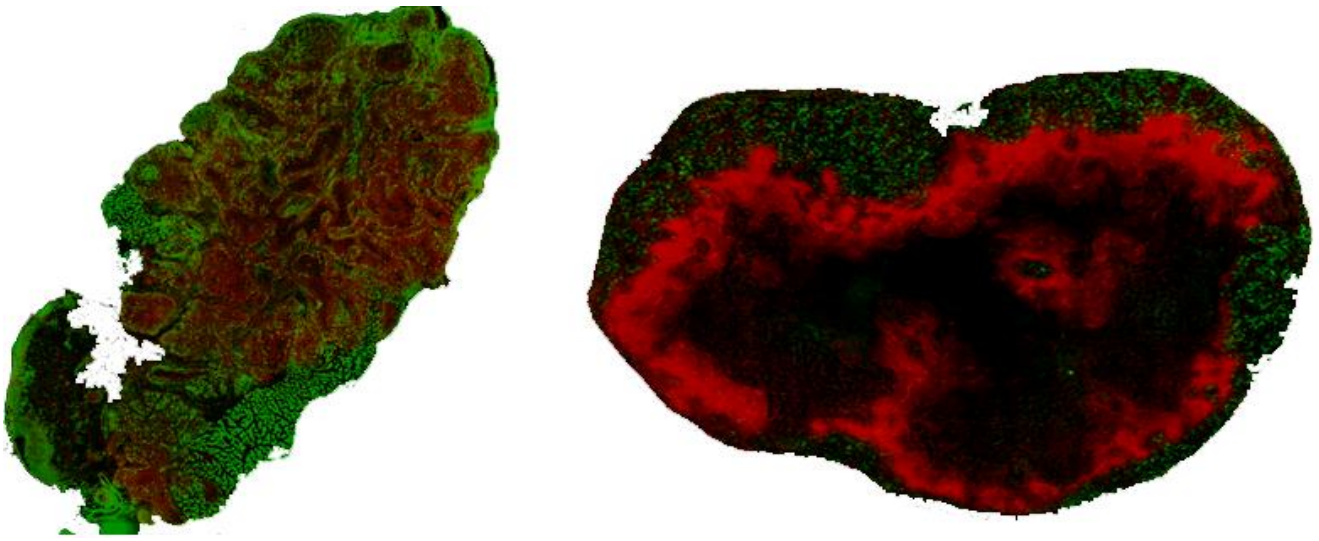

Figure 19: Immunofluorescence images of an SQ20B tumor (Left) and a FaDu tumor (Right) showing the differences in the distribution of hypoxia (red) and increased cell proliferation (green).

3.2.2. Small animal imaging

Each animal was fasted for 6 hours prior to FDG imaging to simulate clinical protocol. Animals were allowed a 60 minute tracer uptake period prior to imaging. The animals were

maintained under 3% isoflurane anesthetizia during the uptake period to prevent FDG accumulation in active muscle groups. After uptake, each mouse was situated on an animal specific pad marked with the body contour and tumor locations (Figure 11).

Images were acquired using a Siemens Inveon dedicated small animal PET/CT/SPECT scanner. PET images were acquired for 10 minutes and the accompanying CT images were acquired for 5 minutes at .5 mA and 75 kV. The following day, animals were fasted again for 6 hours to simulate the same conditions under which animals were previously imaged. Animals were injected with FLT and allowed the same 60 minute uptake period under 3% isoflurane despite FLT uptake being unaffected by active muscle groups. The animal was repositioned on the animal specific pad and imaged using the same protocols as the previous day.

3.2.3. Deformable registration of FDG and FLT images

After image acquisition, images were imported into the Slicer 3D for image registration and analysis. The PET images cannot be used as the inputs for the deformation as this would bias the results and force the FLT PET to mimic the FDG PET rather than preserving the biological tracer distribution. In order to achieve a registration that alleviates errors caused by mispositioning and anatomical changes while preserving the integrity of the true tracer distribution, the CT anatomy was used to generate a deformable registration transform. The CT accompanying the FLT PET image (moving image) was registered to the CT of the FDG data set (fixed image) using the BRAINSFit B-spline implementation in the Slicer package. As described in the registration protocol, no automatic image set initialization was allowed in Slicer registration and all contours used as inputs to the algorithm were generated automatically through the auto-generate ROI option. All images were initialized manually prior to registration to ensure the overlap of the images in the SARRP CT coordinate system. All tumor contours used for analysis were

manually contoured on the original fixed CT image set. The B-spline transform generated by deforming the moving image set was then applied to the FLT PET image to achieve an unbiased and objective registration of the FLT and FDG PET images.

3.2.4. Voxel-by-voxel tracer analysis

A voxel-by-voxel analysis of PET image sets was performed to analyze the changes in FDG uptake with regards to changes in FLT uptake on a voxel-by-voxel scale. All image sets and manual contours were imported into matlab. The tumor contours were used to mask out all non-tumor data voxels during analysis. FDG and FLT intensities for each voxel were plotted on a scatterplot. Additionally the values were also binned by FLT intensity and an average value was calculated for each bin to visualize the trends in the data (Figure 20).

.

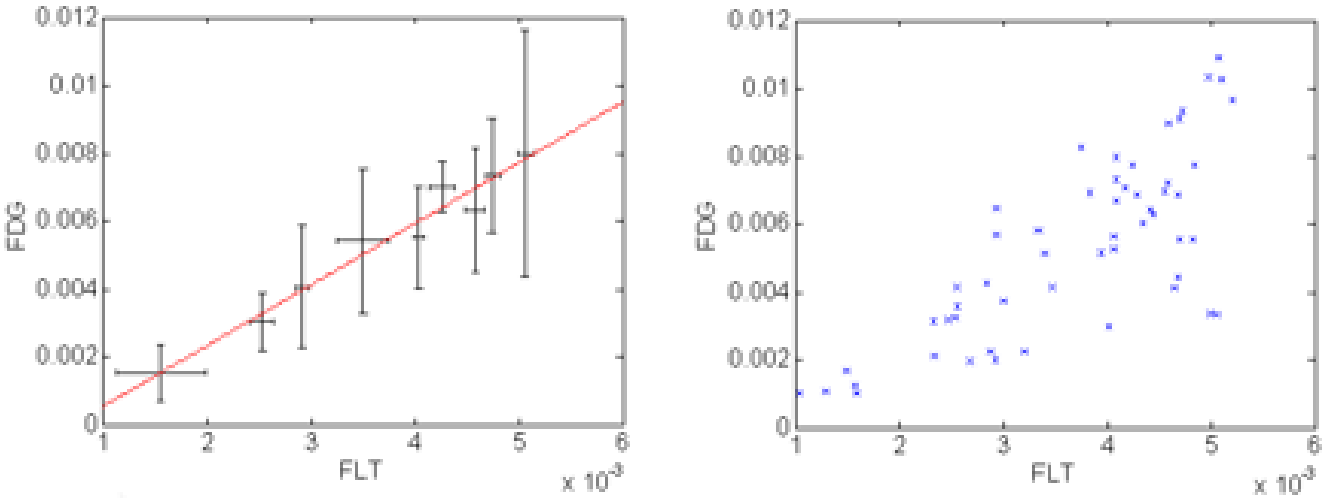

Figure 20: Binned and scatterplot representations of the correlation between FLT and FDG on a voxel-by-voxel basis in a FaDu tumor model

The Pearson correlation coefficient, rho, was also calculated for each data set and is defined as:

$$\rho = \frac{\mathrm{cov}(X,Y)}{\sigma_x \sigma_y}$$

Where cov(X,Y) is the covariance of the FDG and FLT voxel intensities and sigma x and sigma y are the standard deviations foreach data set respectively. The Pearson correlation coefficient is a statistical test measuring the similarity between two data sets assumed to be Gaussian data sets sharing similar means. The values of rho range from -1 to 1 with perfectly correlated data showing a 1 and perfectly anti-correlated data showing a -1. This measure explores the differences in how the two tracers change with one another spatially but does not preserve the spatial information in the final correlation coefficient.

3.2.5. Threshold-based tracer analysis

In order to take a look at the spatial distribution of the tracers a threshold-based approach was used. FDG and FLT images were thresholded between 1 and 100% of maximum image intensity and intensity values below the threshold percentage of maximum were omitted. The Dice similarity coefficient was used to compare the overlap of the thresholded FDG volume with the thresholded FLT volume. The Dice similarity coefficient is defined as:

$$d = \frac{|X \cap Y|}{|X| + |Y|}$$

Where X and Y are the number of elements in each data set. The Dice similarity coefficient returns a value of 1 if the volumes are perfectly concordant and a value of 0 if the two volumes never overlap. These Dice ceofficients were tabulated for all threshold values between 1 and 100% and a three dimensional "Dice surface" was created by plotting the values (Figure 21).

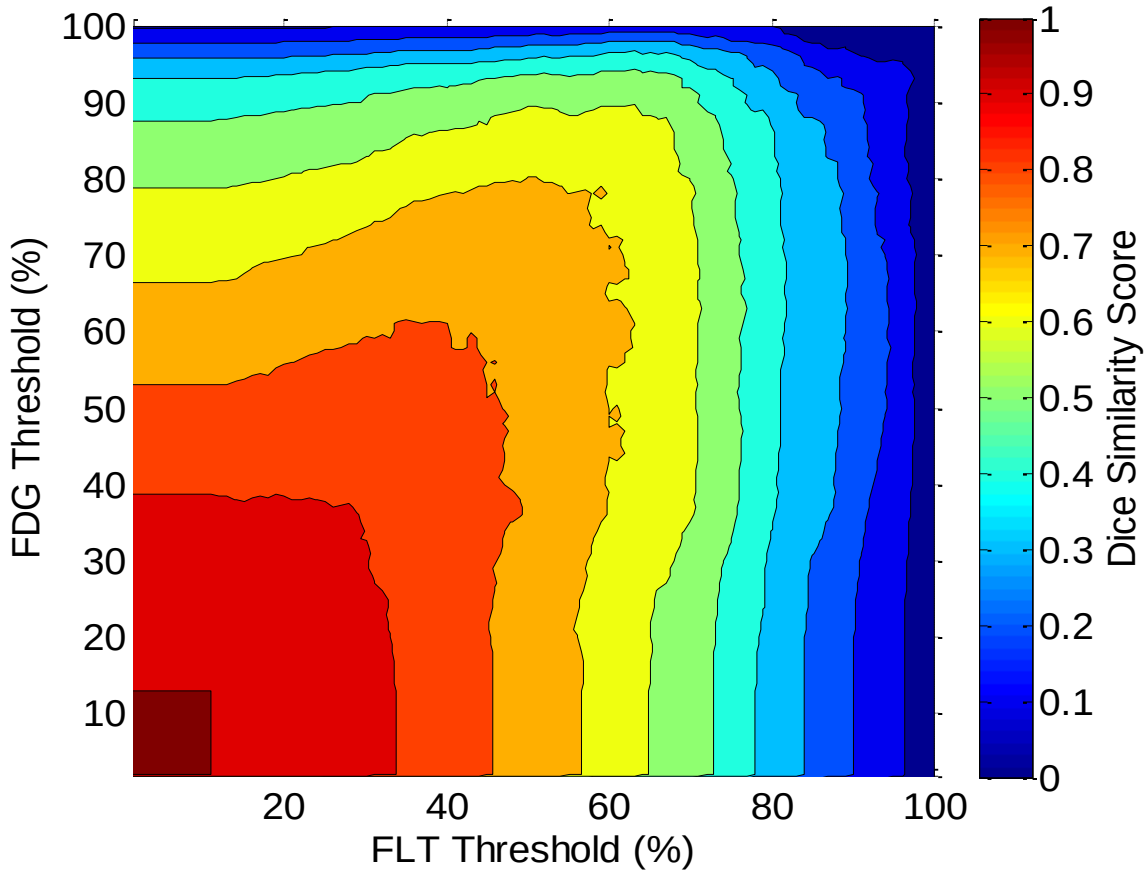

Figure 21: A "Dice similarity surface" created by varying FDG and FLT thresholds and plotting the Dice Coefficient

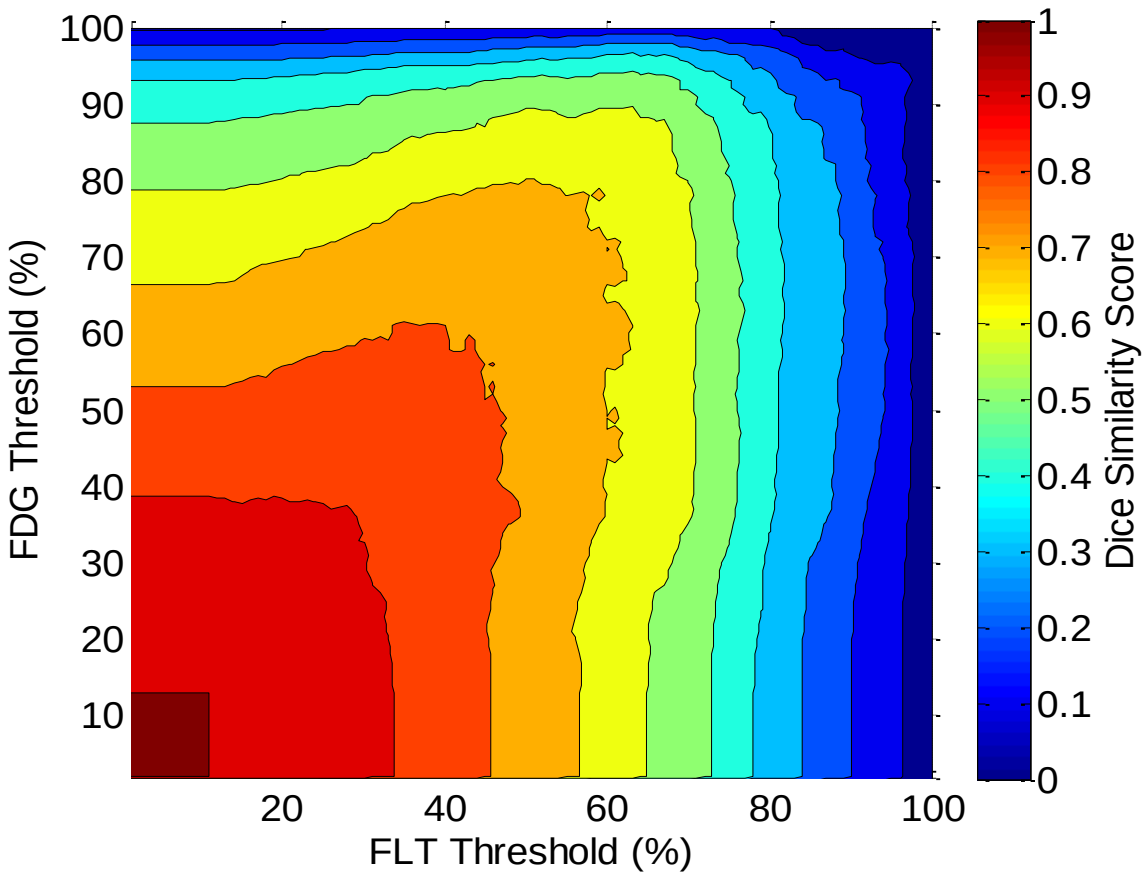

3.3.Results

The Slicer 3 Analysis revealed a positive correlation between the uptake of FDG and FLT within the tumor for both tumor lines. FaDu tumors exhibited a statistically significant average

correlation coefficient of r = .468 while SQ20B exhibited an average correlation coefficient of r = .704. The strength of correlation between FDG and FLT in FaDu and SQ20B tumors was statistically significant with a stronger correlation seen in the SQ20B tumors. This is likely due to the intermixed heterogeneous biology of the SQ20B cell line. There are typically no regions of interest within the tumor can be specifically selected as exclusively hypoxic or highly proliferating. Taking into account the inherent blur of the PET detector as well as biology, the FDG and FLT distributions appear more similar in the SQ20B images than in the FaDu images which exhibit a more compartmentalized geometry.

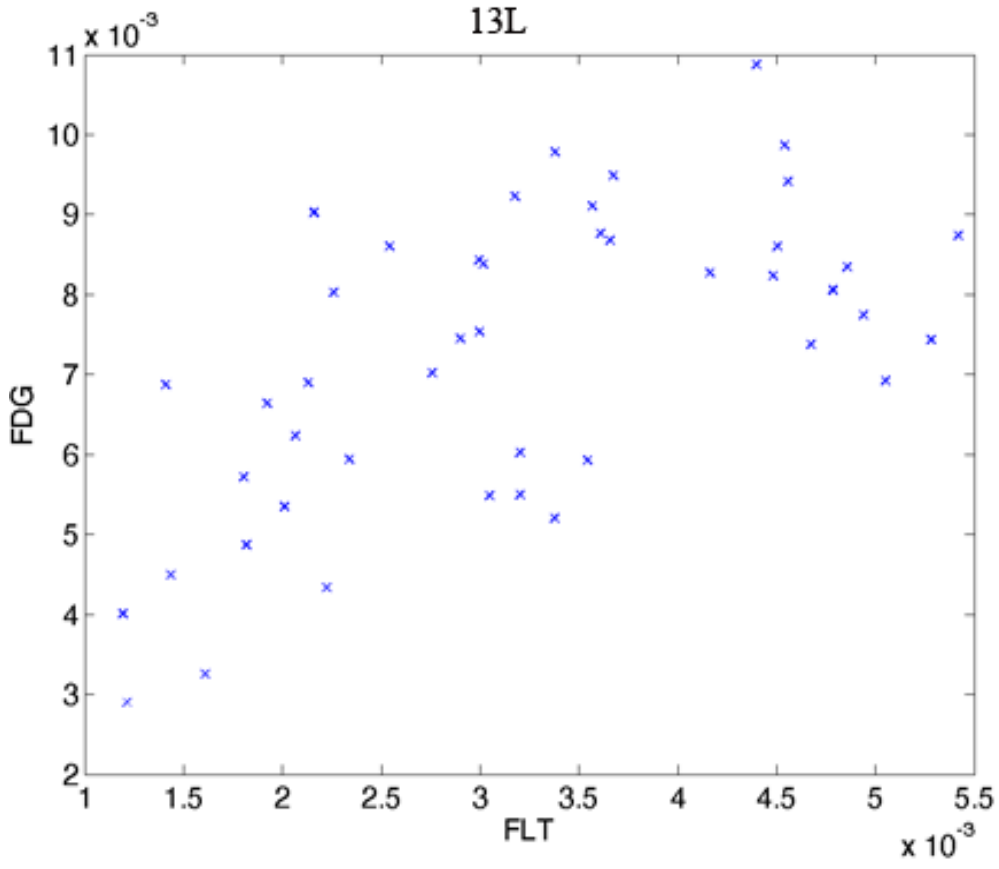

Figure 22: Scatterplot showing the changes in FLT and FDG uptake in each voxel of the PET image for the FaDu tumor 13L

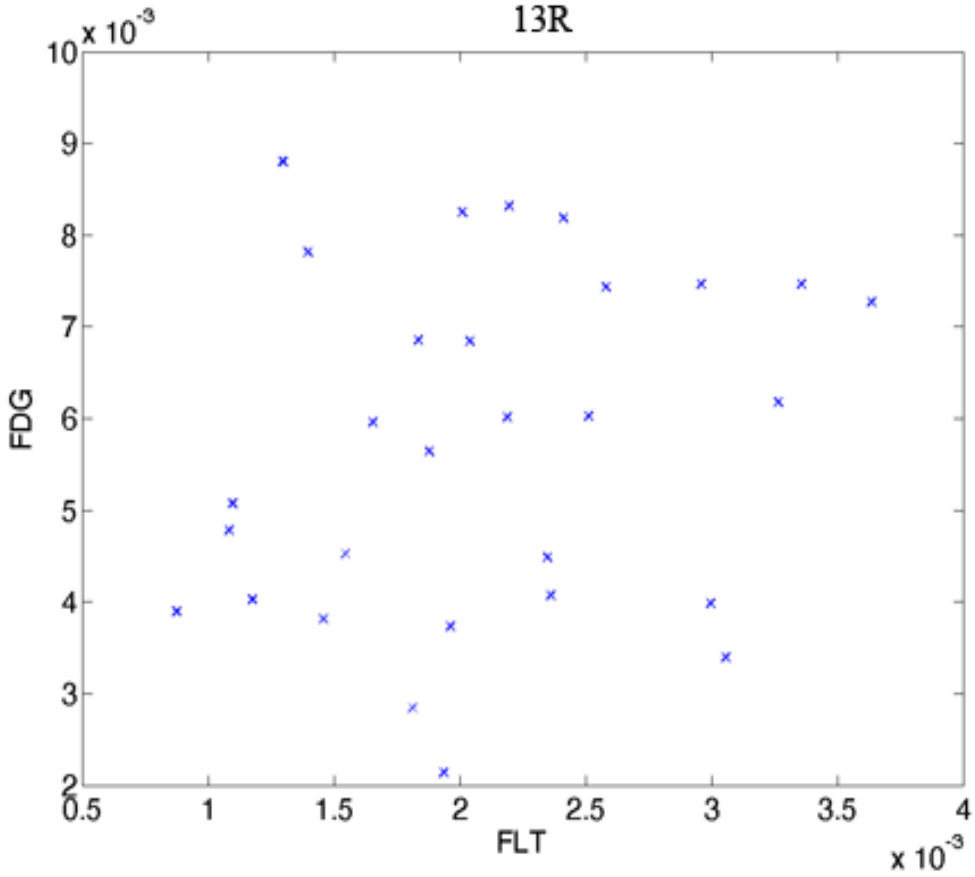

Figure 24: Scatterplot showing the changes in FLT and FDG uptake in each voxel of the PET image for the FaDu tumor 13R

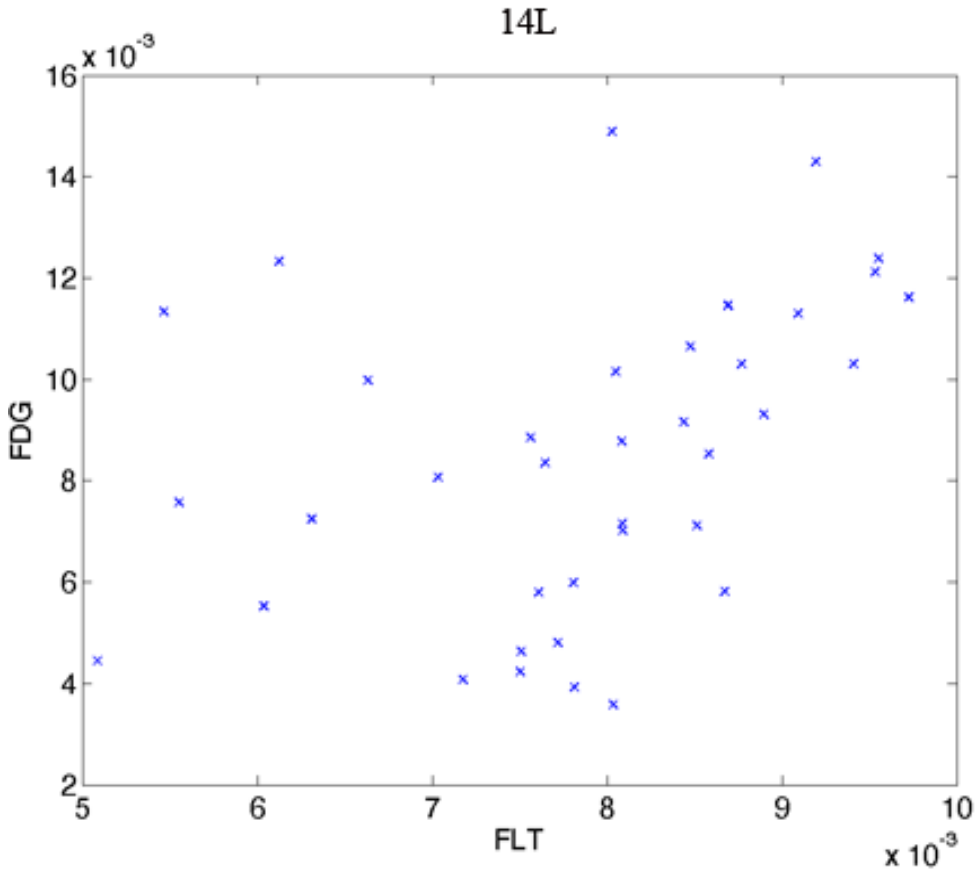

Figure 23: Scatterplot showing the changes in FLT and FDG uptake in each voxel of the PET image for the FaDu tumor 14L

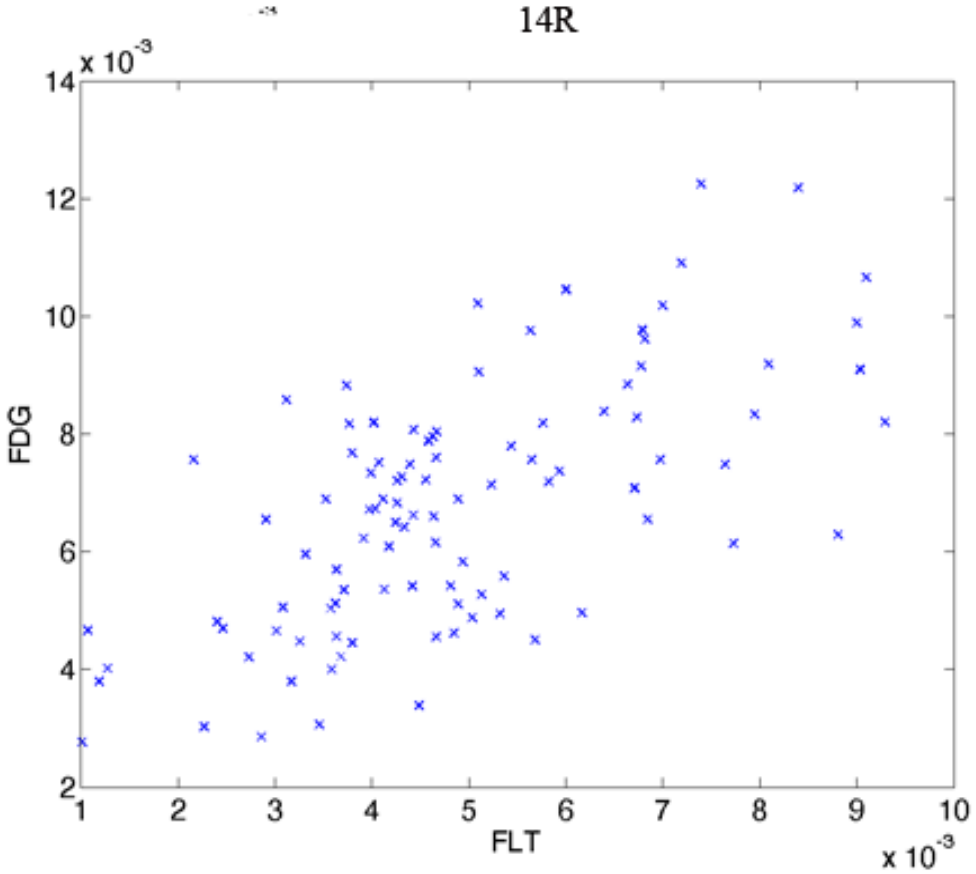

Figure 26: Scatterplot showing the changes in FLT and FDG uptake in each voxel of the PET image for the SQ20B tumor 14R

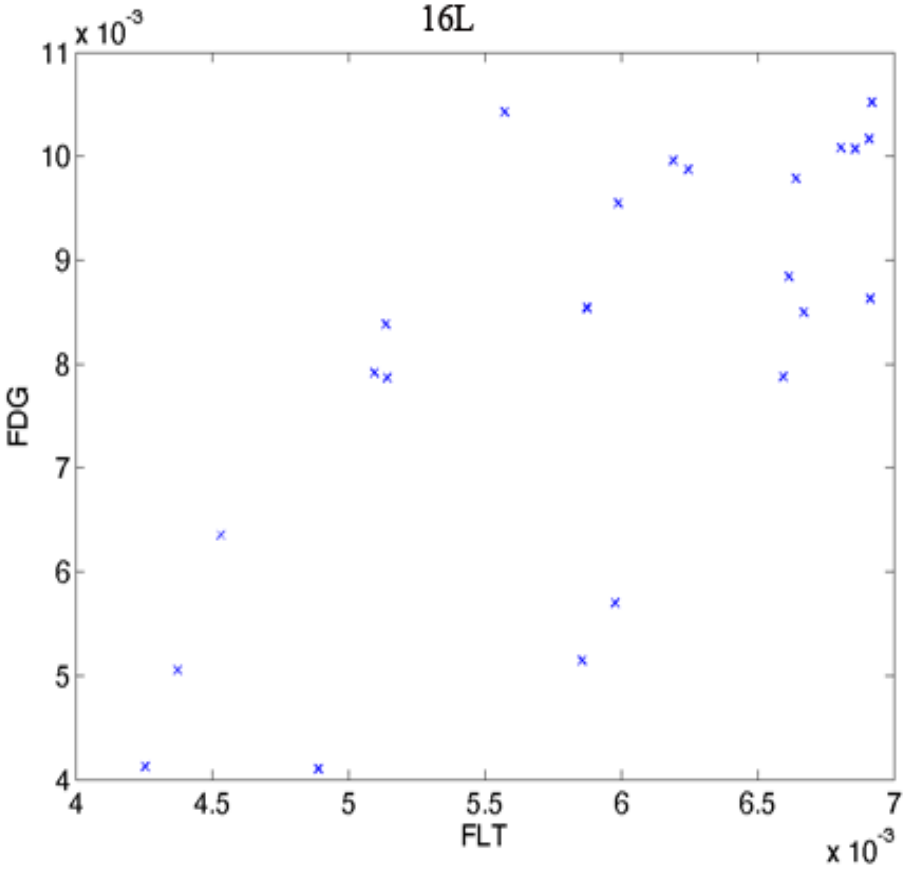

Figure 25: Scatterplot showing the changes in FLT and FDG uptake in each voxel of the PET image for the FaDu tumor 16L

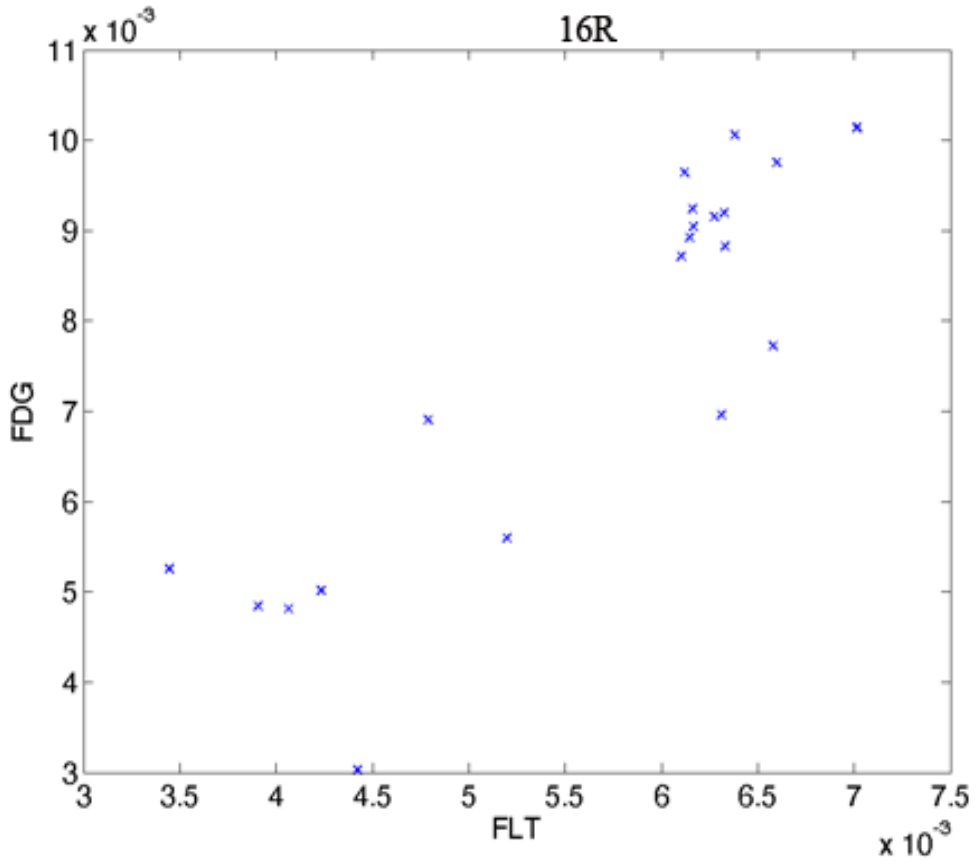

Figure 27: Scatterplot showing the changes in FLT and FDG uptake in each voxel of the PET image for the SQ20B tumor 16R

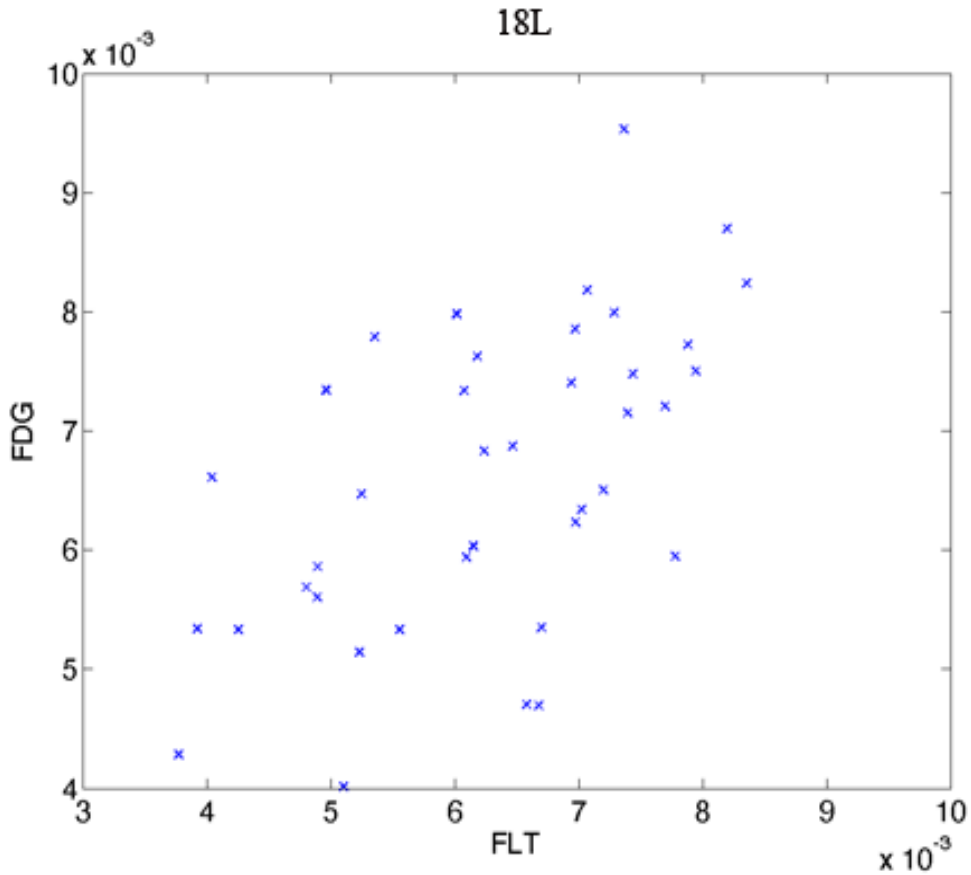

Figure 28: Scatterplot showing the changes in FLT and FDG uptake in each voxel of the PET image for the SQ20B tumor 18L

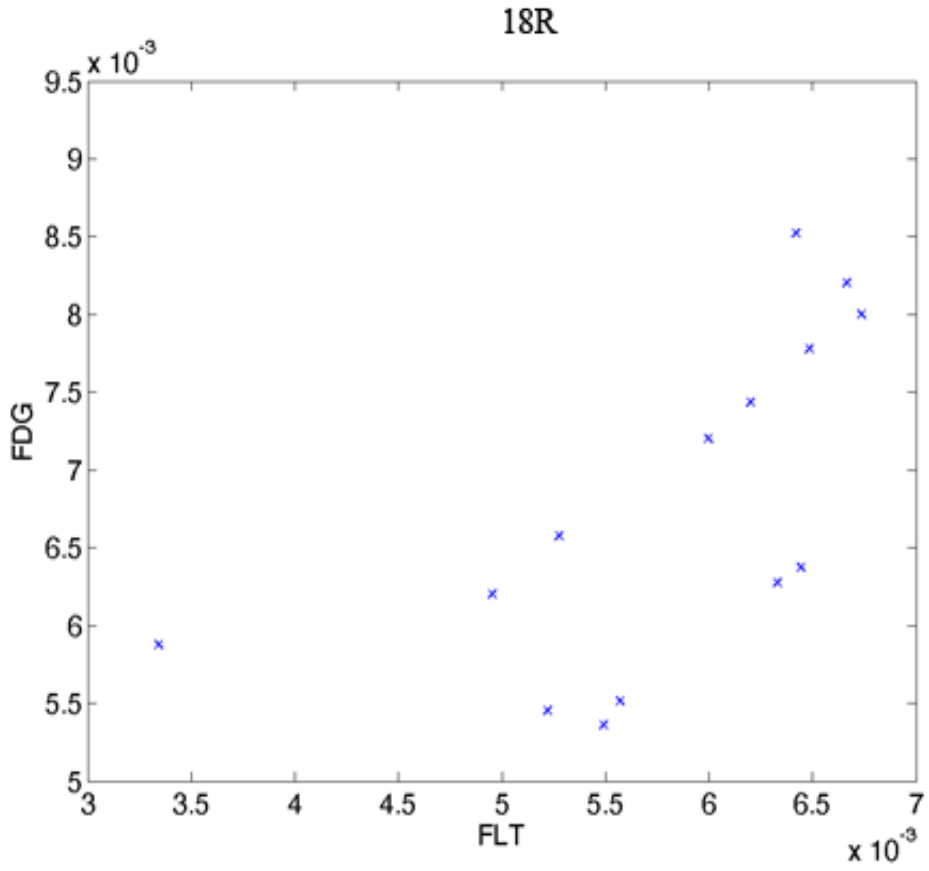

Figure 29: Scatterplot showing the changes in FLT and FDG uptake in each voxel of the PET image for the SQ20B tumor 18R

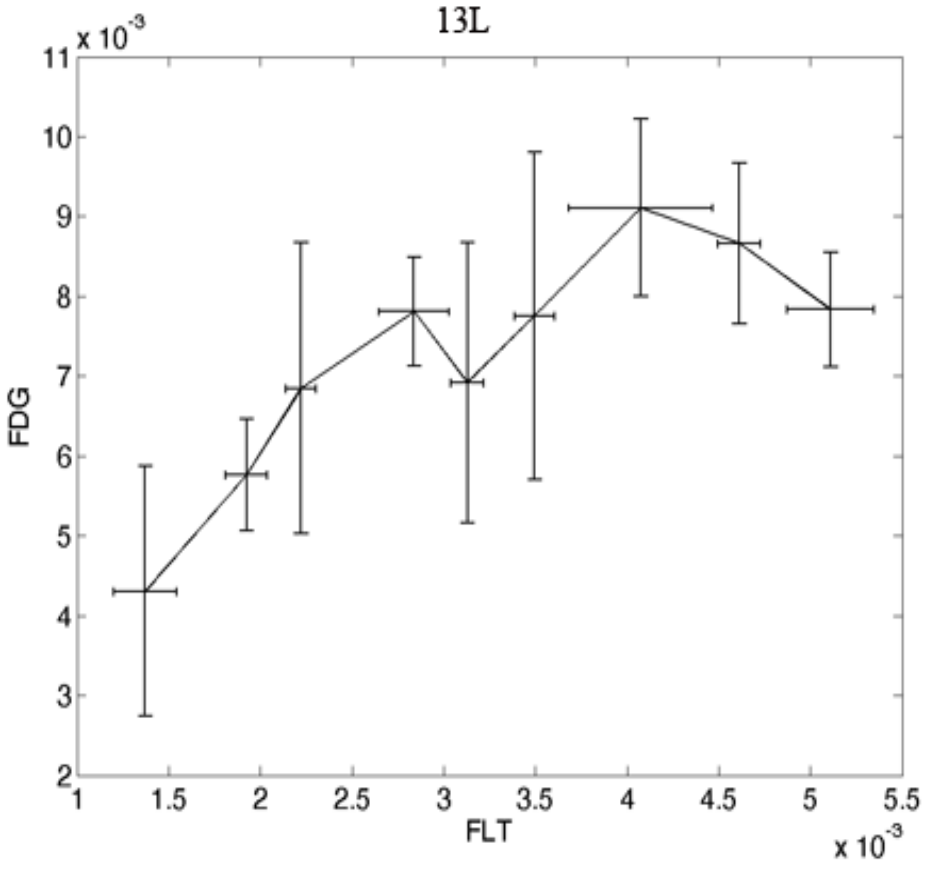

Figure 30: The scatterplot data binned and averaged by FLT intensity illustrating the change in FLT with FDG for the FaDu tumor 13L

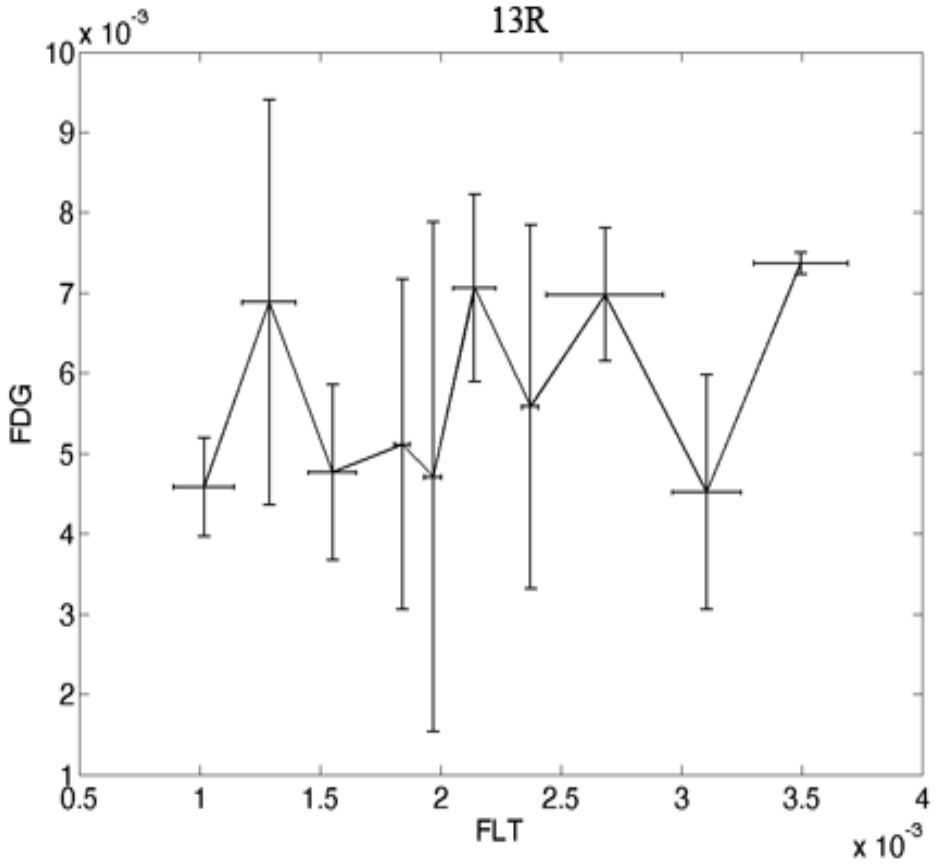

Figure 31: The scatterplot data binned and averaged by FLT intensity illustrating the change in FLT with FDG for the FaDu tumor 13R

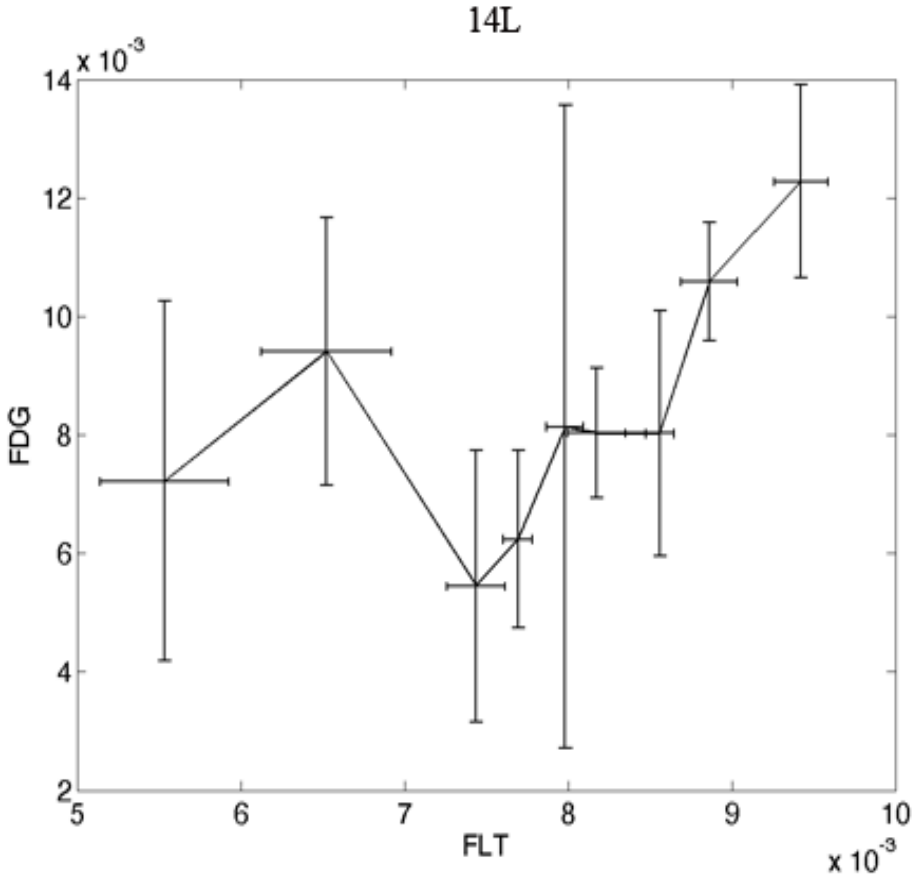

Figure 32: The scatterplot data binned and averaged by FLT intensity illustrating the change in FLT with FDG for the FaDu tumor 14L

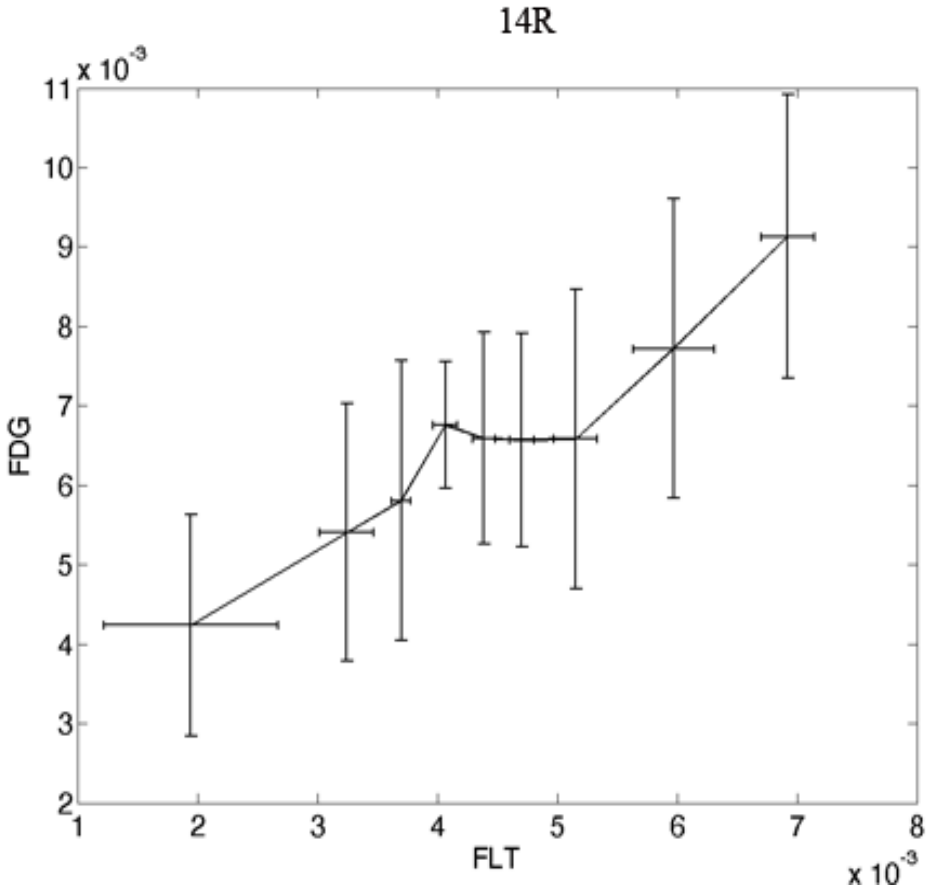

Figure 33: The scatterplot data binned and averaged by FLT intensity illustrating the change in FLT with FDG for the FaDu tumor 14R

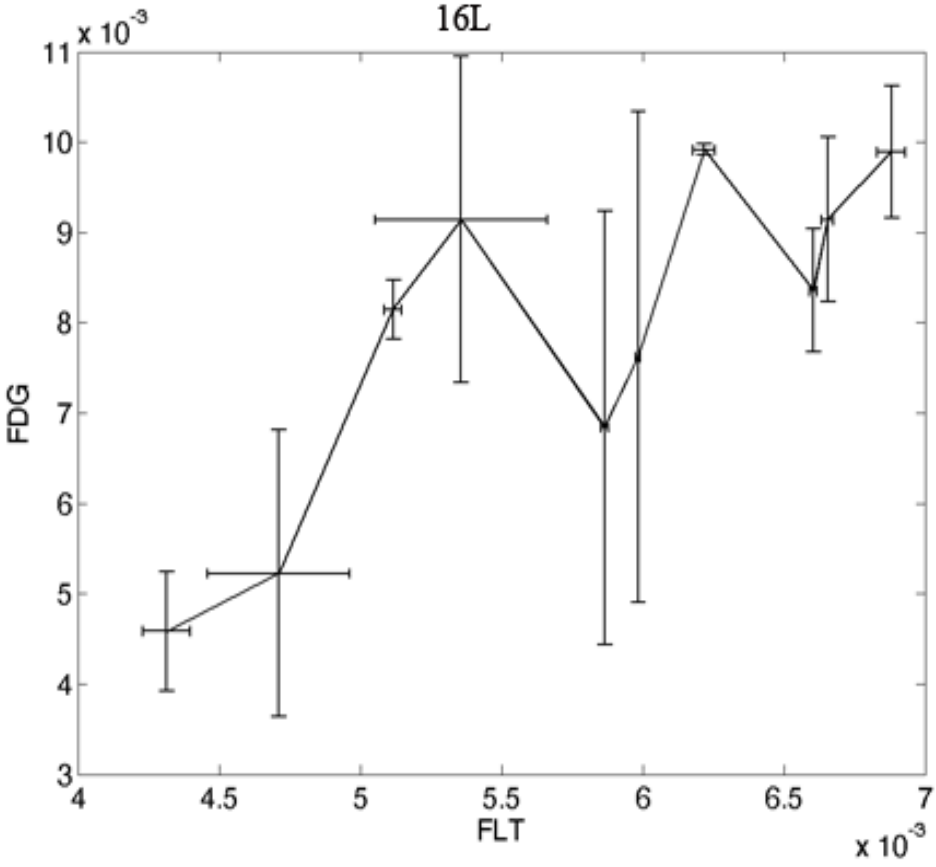

Figure 34: The scatterplot data binned and averaged by FLT intensity illustrating the change in FLT with FDG for the SQ20B tumor 16L

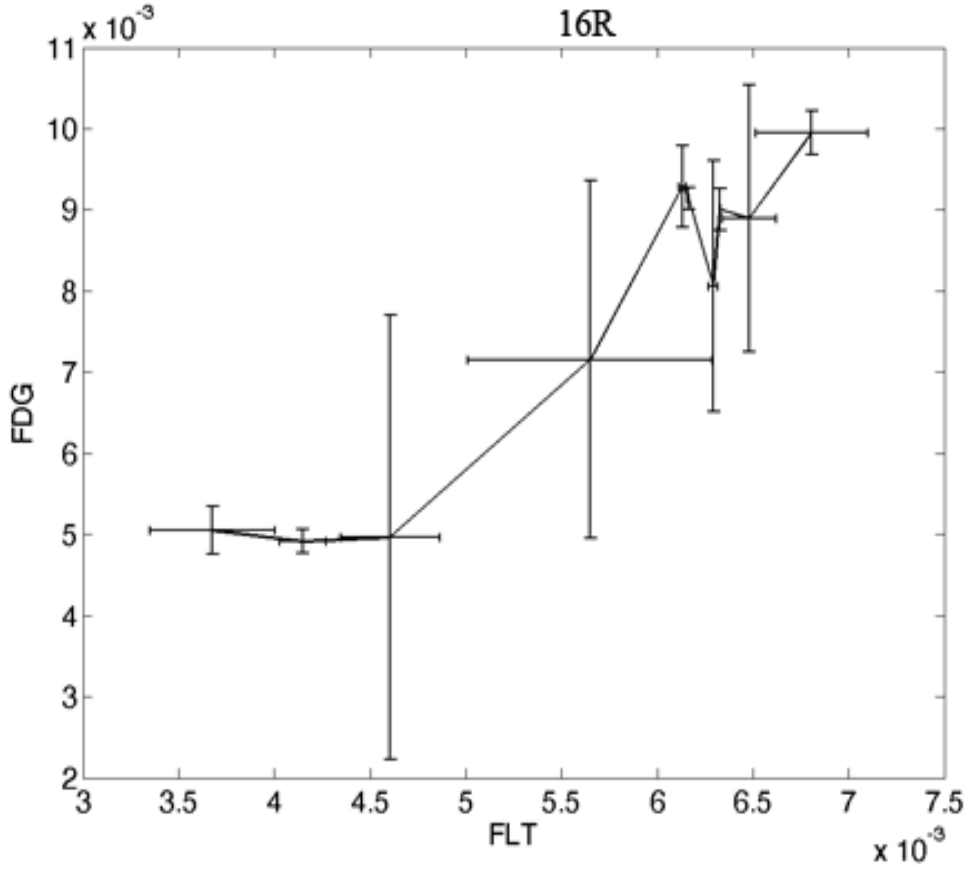

Figure 35: The scatterplot data binned and averaged by FLT intensity illustrating the change in FLT with FDG for the SQ20B tumor 16R

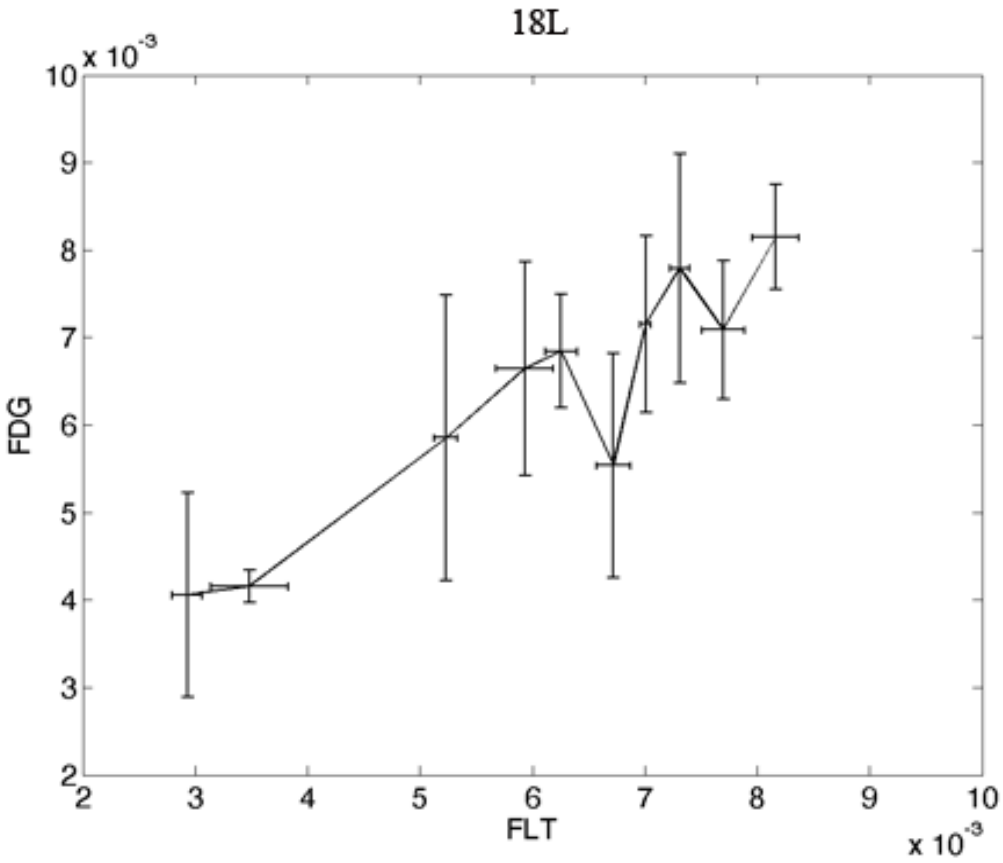

Figure 36: The scatterplot data binned and averaged by FLT intensity illustrating the change in FLT with FDG for the SQ20B tumor 18L

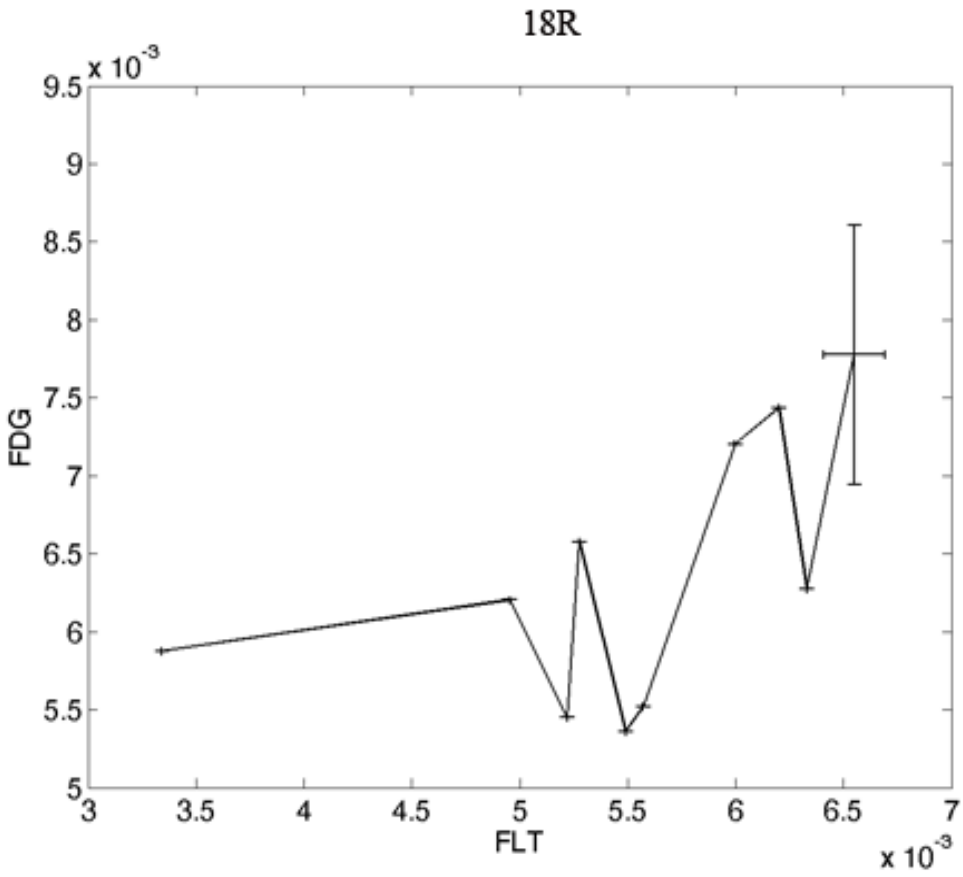

Figure 37: The scatterplot data binned and averaged by FLT intensity illustrating the change in FLT with FDG for the SQ20B tumor 18R

The Slicer 3 overlap analysis showed a lower overlap between the volumes at higher thresholds. At thresholds of 50% for both images, the high intensity regions overlap on average by 78% for FaDu and by 89% for SQ20B. At 75% threshold for both images the overlap drops to only 47% for FaDu and 68% for SQ20B. If one were to begin thresholding FDG, it is obvious that the volumes of FDG and FLT diverge and at higher uptakes of FDG, FLT in some cases is an almost an entirely separate volume. This is likely due to the fact that FDG is specific to glucose metabolism which is upregulated in many different cells; hypoxic cells for example show an increased glucose metabolism.

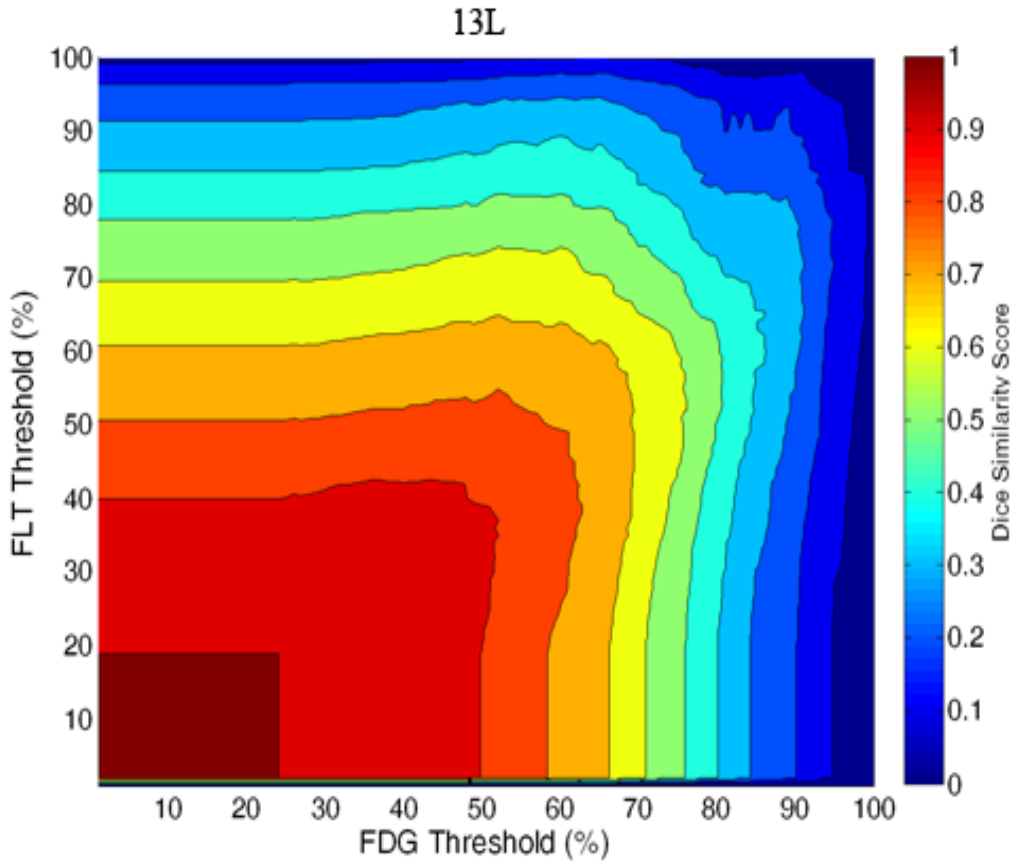

Figure 38: A plot showing the change the spatial overlap between FDG and FLT sub-volumes defined by thresholding PET images at different percentages of maximum intensity for FaDu tumor 13L

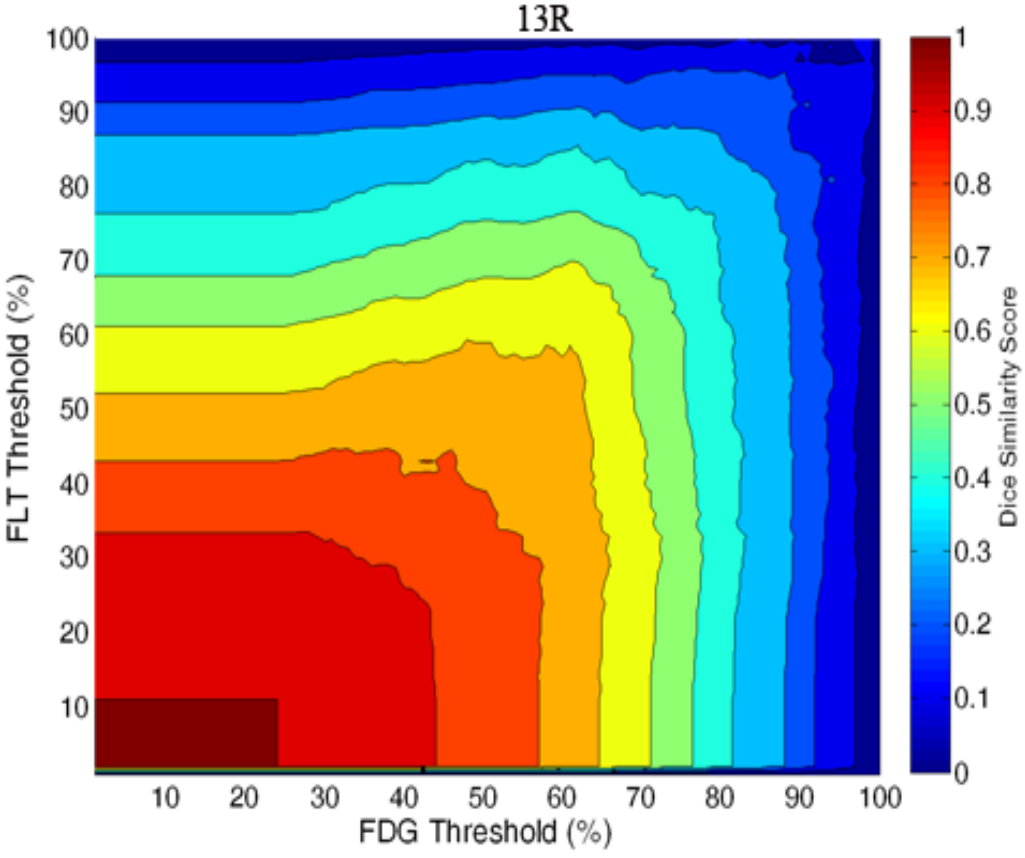

Figure 39: A plot showing the change the spatial overlap between FDG and FLT sub-volumes defined by thresholding PET images at different percentages of maximum intensity for FaDu tumor 13R

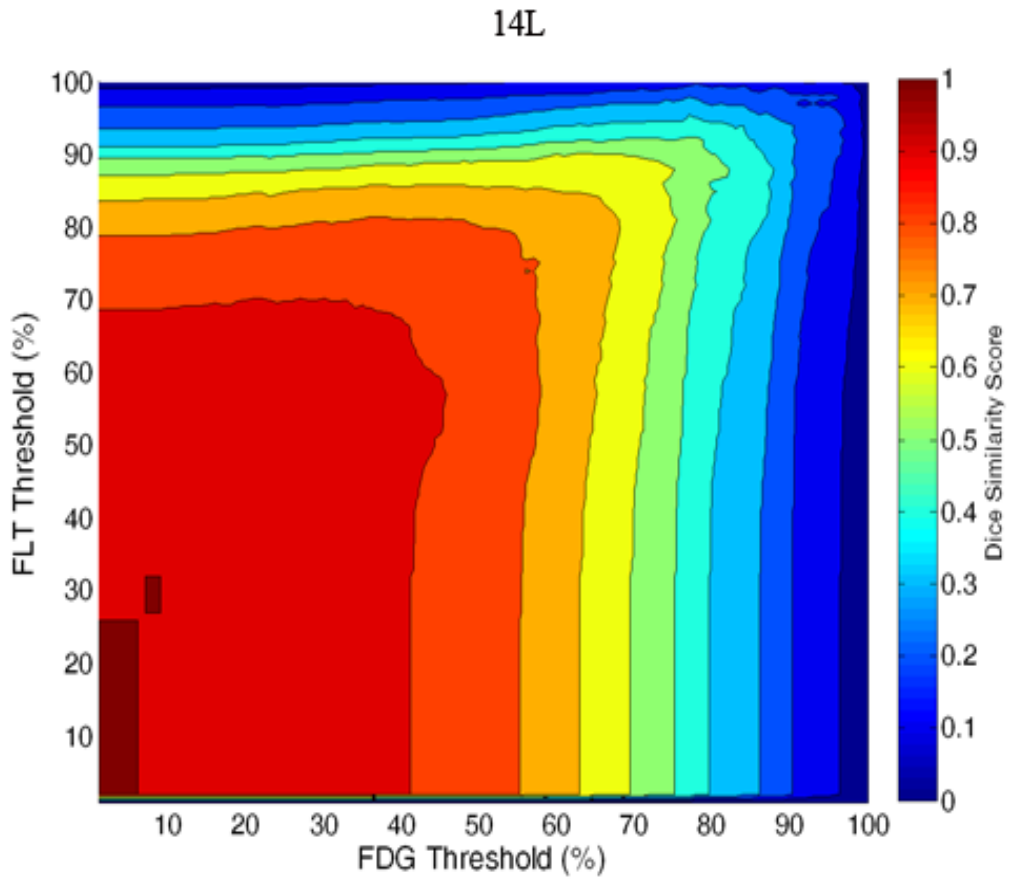

Figure 40: A plot showing the change the spatial overlap between FDG and FLT sub-volumes defined by thresholding PET images at different percentages of maximum intensity for FaDu tumor 14L

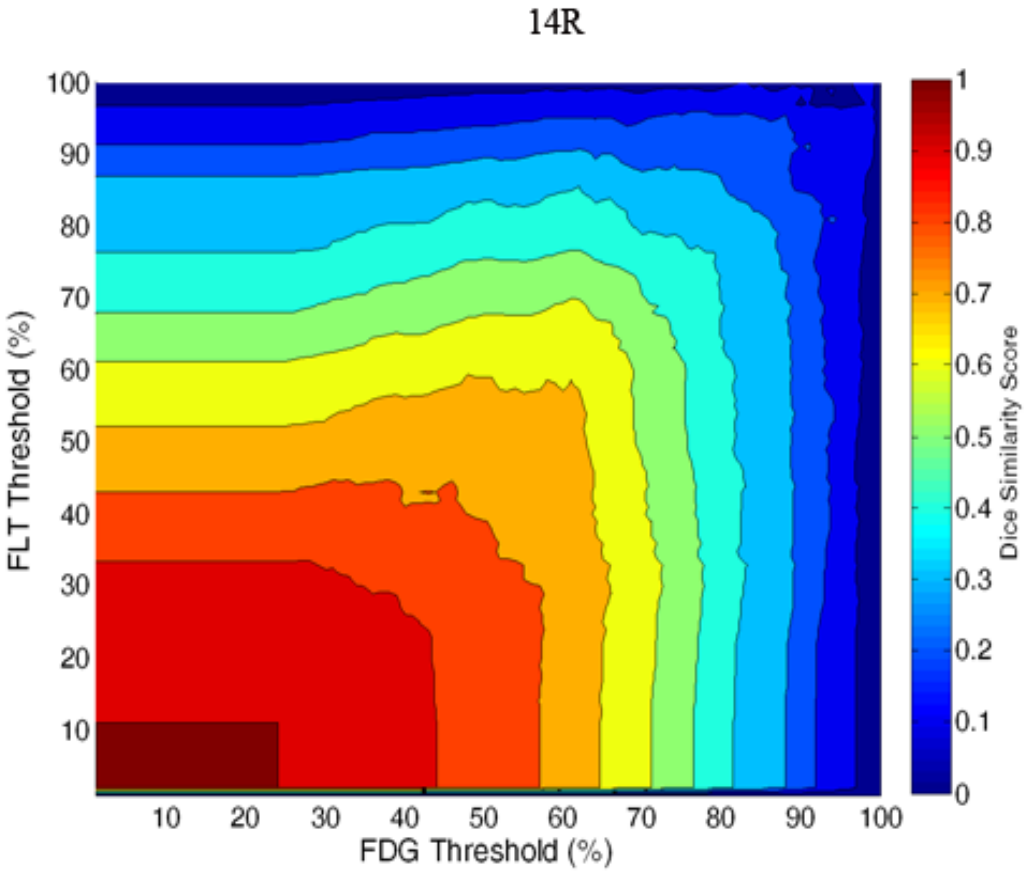

Figure 41: A plot showing the change the spatial overlap between FDG and FLT sub-volumes defined by thresholding PET images at different percentages of maximum intensity for FaDu tumor 14R

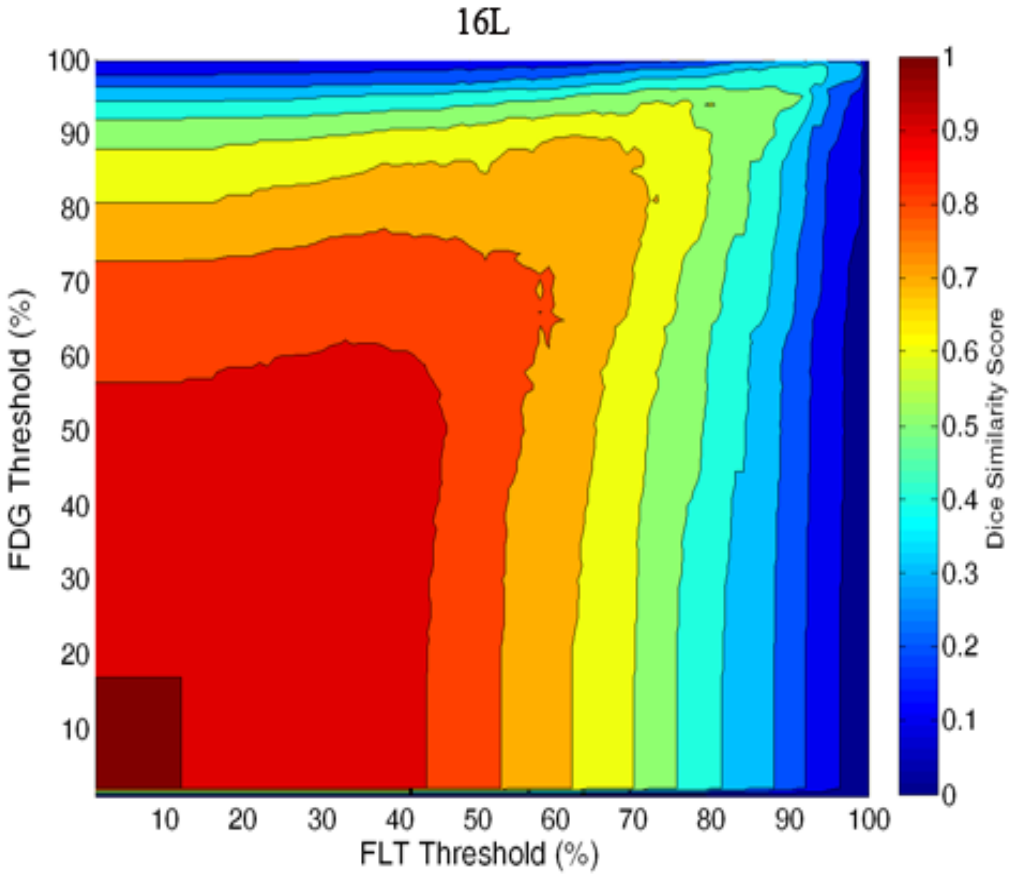

Figure 42: A plot showing the change the spatial overlap between FDG and FLT sub-volumes defined by thresholding PET images at different percentages of maximum intensity for SQ20B tumor 16L

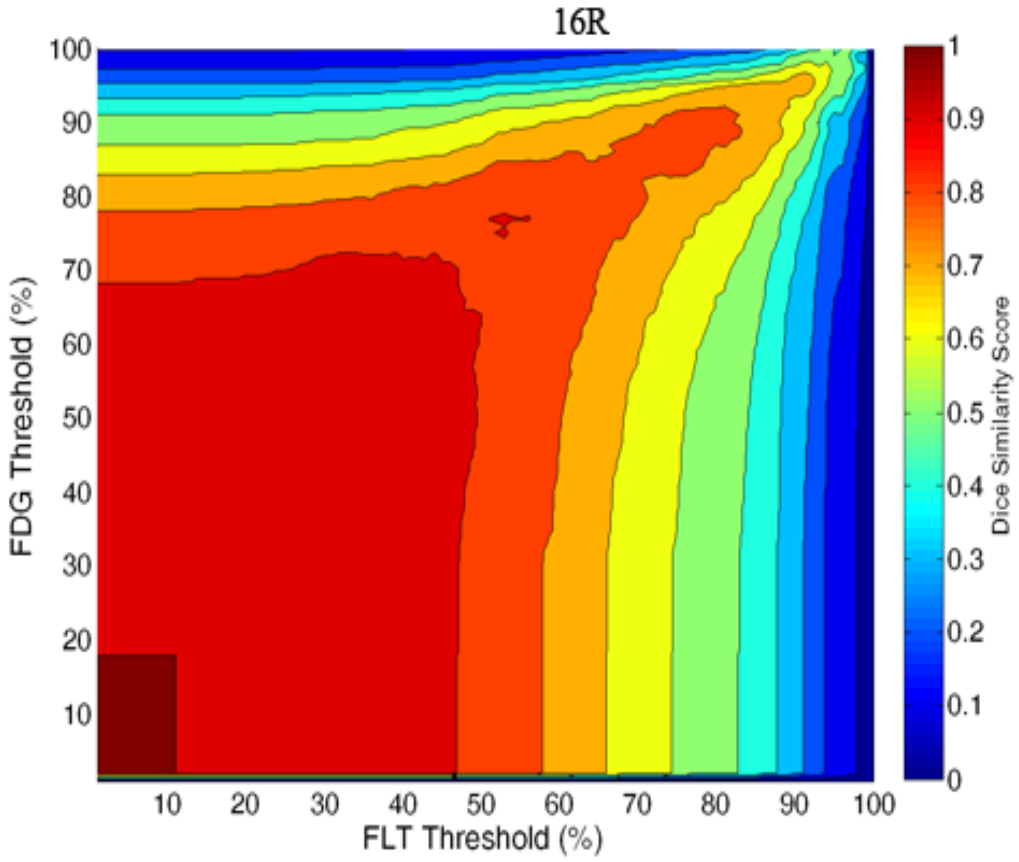

Figure 43: A plot showing the change the spatial overlap between FDG and FLT sub-volumes defined by thresholding PET images at different percentages of maximum intensity for SQ20B tumor 16R

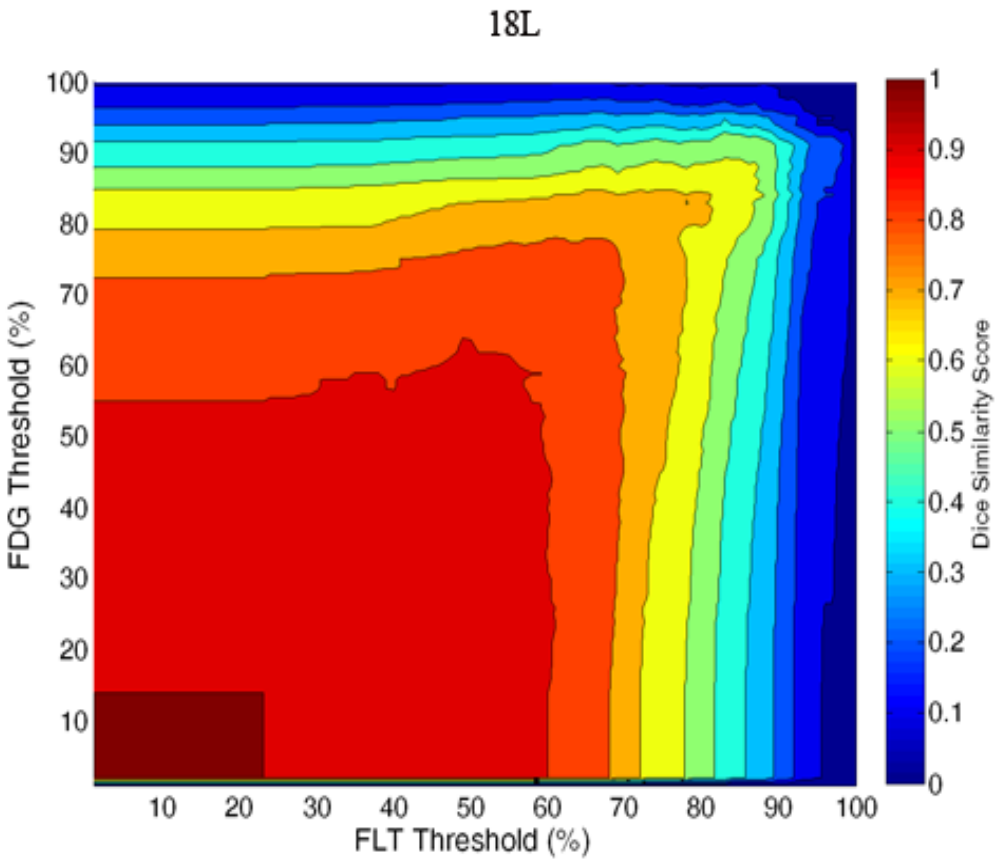

Figure 44: A plot showing the change the spatial overlap between FDG and FLT sub-volumes defined by thresholding PET images at different percentages of maximum intensity for SQ20B tumor 18R

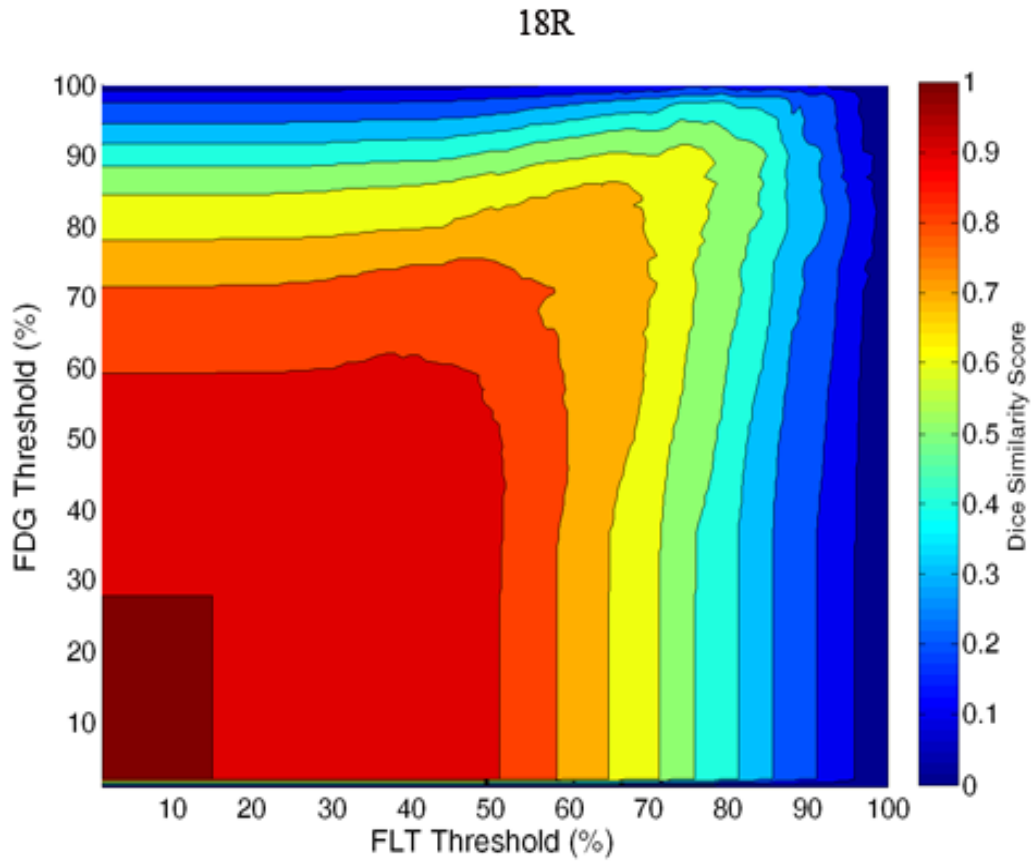

Figure 45: A plot showing the change the spatial overlap between FDG and FLT sub-volumes defined by thresholding PET images at different percentages of maximum intensity for SQ20B tumor 18L

This data implies that the higher intensity FDG values are not indicative of proliferation but are more likely indicative of some other phenomenon, though the verification of this would require the same analysis with more tracers in future works. FaDu tumors also show more disagreement between FLT and FDG than the SQ20B tumor line. These results seem to agree logically with an analysis of the morphology of the two tumors. Histological analysis of the SQ20B tumor line exhibits a largely heterogeneous distribution of areas of small, intermixed hypoxic and proliferating cells. This would result in uptakes of FDG and FLT that would be largely concordant. The PET image resulting from these distributions would logically yield very similar images as the inherent resolution of the PET image would cause blurring and create two similar images. The FaDu images, on the other hand, show a greater difference between the two tracers. For FaDu tumors, the histology shows a much more compartmentalized model with areas of high proliferation being better defined and isolated from areas of hypoxia and normal cell metabolism. The resulting lower correlations in FaDu tumors supports the idea that FLT and FDG would be more encapsulated and less likely to uptaken in identical volumes despite the effect of large areas of necrosis forcing tracers into specific regions of the cell. This analysis implies that FDG and FLT do exhibit similar volumes but FLT yields additional spatial information that is not exhibited in FDG images. While these volumes may be small, in radiation oncology leaving any tumor cells untreated can be considered a failure of treatment.

Clinically these results imply that FDG and FLT images could be acquired sequentially to gain additional insight into the microbiology of a tumor. The extent of additional information available is dependent on the tumor cell line with SQ20B tumors showing significantly more overlap of the FDG and FLT tumor volumes. The differences in overlap between FDG and FLT avid volumes determined by thresholding images above 50 percent of maximum imply that any

clinical approaches suggesting PET thresholding as a tool for tumor delineation should add additional margins to account for FLT avid regions not encompassed by FDG. Additional spatial analysis will be required in the future to determine the extent of these margins.

In conclusion, FLT images yield additional useful information regarding the distribution of proliferating tumor cells. This becomes even more apparent when thresholding and auto-segmentation of FDG images is used. In order to ensure treatment of these sub-volumes FLT should be considered for biological treatment planning assuming the introduction of a reliable clinical system for image registration of PET images. In addition, the inclusion of tracers of cell hypoxia in this same kind of analysis could yield to a better understanding of FDG tracer uptake in the tumor.

Chapter 4: PET imaging as an image guidance tool for placement of dose escalation for pre-clinical models

Chapter 4 of this thesis provides the background literature review of PET's role in treatment planning and discusses establishing a procedure for PET-guided selective radiation dose escalation in small animal tumor models. It is hypothesized that utilizing new small animal treatment technologies and deformable image registration it is possible carry out PET dose escalation on a small animal tumor models.

4.1.Background

Histological analysis of resected tumors has shown that underlying tumor biology is highly heterogeneous in nature and the radio-sensitivity of cells may vary across the tumor. Advances in imaging techniques and the advent of novel PET tracers have facilitated non-invasive evaluation of this underlying biology for radiotherapy treatment planning. In 2000 Ling et al. proposed to use PET imaging as a non-invasive method for acquiring information about tumor microbiology [9]. Ling suggested that utilizing the spatial distributions of FDG, FLT and Fluoromisonidazole (F-MISO) and the CT-delineated gross tumor volume (GTV) that treatments could be individualized for each patient. The addition of PET images to the anatomical GTV would allow physicians to consider the radio-resistance of different areas of the tumor rather than the entire tumor as a single mass.

Since the publications of Ling et al. in 2000, many studies have explored the feasibility of PET image guidance. In 2003, Tralins et al. carried out a clinical trial using PET, MRI and CT to guide dose escalations to 38 patients with glioblastoma multiforme brain tumors. Tralins defined the PET tumor volume as any area within the CT and MRI defined GTV with higher PET tracer

uptake than normal white matter outside the GTV. The comparison of the CT-, MRI- and PET derived tumor volumes revealed that high FDG uptake defined a volume which was 25% smaller than the volumes defined by MRI and CT Additionally Tralins et al. found that the uptake of FDG tracer was a predictor of treatment outcome [19].

Schwartz et al. carried out an investigation of the potential role of FDG PET in head and neck cancer dose escalation in 2004. 20 patients with various head and neck cancers were imaged using a dedicated PET scanner and a separate dedicated CT scanner. After imaging, b-spline deformable image registration was used to alleviate the effects of mispositioning. Schwartz et al. defined the PET-avid region, or GTV PET, as any area within the CT-contoured GTV exhibiting higher FDG uptake values than normal tissue. Only 5 patients underwent treatment in this study, receiving 66 Gy to gross disease in 30 fractions. The GTV PET was then escalated by repeatedly treating with 2.2 Gy fractions until a dose limiting normal tissue constraint was reached. Ultimately this study produced no results regarding improvement of tumor control or patient survival. Schwartz et al. did conclude that dose escalation up to doses of 72.4 Gy were feasible for escalation of a PET GTV [18].

In a 2005 study of locally advanced non-small cell lung cancer patients, De Ruysscher et al. used a dedicated dual-modality PET/CT scanner to acquire intrinsically fused PET/CT image sets. These image sets were used to generate and compare treatment plans using CT information and plans using PET/CT information. De Ruysscher et al. concluded that PET-avid regions produced smaller treatment volumes than CT-contoured target volumes and as such could be treated to higher doses before normal tissue complications were observed [16]. Van Der Wel at al. also reported similar findings in their 2005 modeling of PET--contoured radiotherapy planning [17].

All of these studies have produced results supporting the escalation of dose to sub-volumes of CT-defined GTV without compromising normal tissue. They all exclusively use FDG PET to delineate an active tumor volume within the GTV for treatment. As FDG images are representative of increased glucose metabolism they are typically used to define the entire tumor rather than radio resistance sub-volumes. As such, all of the presented studies neglect the heterogeneity of the underlying biological properties of the tumor. The goal of treatment planning for all of these studies was to deliver a homogeneous dose to the tumor volume as defined by PET. Dose escalation, in the context of these studies, refers to the researcher's ability to treat the tumor to higher homogeneous doses while achieving the same organs at risk dose due to the smaller clinical target volumes as determined by PET. This differs greatly from the scenario proposed by Ling et al. in which the dose was escalated to regions of interest (ROI) throughout the entire tumor with the goal of treating specific cells to a dose determined by their respective radio-resistances.

Vanderstraeten et al. proposed the concept of prescribing dose to individual voxels using the intensities in the PET image to determine dose. The intensity in each voxel of the PET image is directly related to the activity of FDG in each voxel at the time of imaging. This approach assumed a positive correlation between tracer uptake and radio-resistance. To this end, Vanderstraeten assigned higher doses to voxels with higher intensity relative to other voxels within the GTV. This approach became known as dose paint-by-numbers in contemporary research studies. In this study the dose paint-by-numbers approach was compared to a more conservative method in which the PET image was broken into regions of interest by binning voxels into discrete groups and prescribing dose to regions rather than voxels. Vanderstraeten ultimately concluded that their modeling of both voxel-defined and region of interest-defined

dose prescriptions showed no significant effect on the organ at risk doses. These results imply that the dose to the tumor can be redistributed to treat features of interest within the image preferentially without detrimental effect to the organs at risk. Vanderstraeten did, however, point out that in order to be able to improve local control it would be necessary to establish the relationship between PET tracer uptake and cell radio-sensitivity in a voxel [52].

Madani et al. carried out the first dose paint-by-numbers phase I clinical trial in 2007. 41 patients were treated using the voxel-defined dose assignment method published by Vanderstraeten et al. to treat areas of higher PET uptake to higher doses and areas of lower PET uptake to reduced doses. Madani et al. reported an average patient one year survival rate of 83.5%. In general, Madani concluded that PET dose escalation is achievable in patients. It is important to note, however, that Madani et al. did report a treatment-related death at higher dose levels. The specifics of this treatment related death were not disclosed in the paper [53].

Overall, research towards biologically-guided treatment has been slowly progressing towards the vision presented in the Ling's 2000 publication. Still, there is little evidence supporting a relationship between increased FDG uptake on a PET image and increased radio-resistance within the tumor [52]. Aerts et al. argue that previously published studies have shown that FDG alone can provide a map of viable tumor cells. Aerts suggests that escalating dose to an FDG-positive volume will deliver sufficient dose to increase cell kill in radio-resistant sub-populations without the need to explicitly identify them as radio-resistant [2]. Aerts' suggested PET-guided treatments which assume that all glucose avid cells are radio-resistant are inefficient in the redistribution of delivered dose as FDG can be taken up in radio-sensitive cancer cells. Unilaterally escalating dose to the whole tumor will result in increased dose to these radio-sensitive cells which do not require an escalated dose. The escalation of dose to areas of radio-

sensitivity is unnecessary as these cells are rendered non-viable by original, non-escalated prescription dose. Selective dose escalation, or preferentially increasing dose only to regions of high radio-resistance or biological importance, would allow for a lower organ at risk dose in regions bordering radio-sensitive tumor cells.

Due to the lack of data to support the co-localization of high FDG uptake and cells displaying increased radio-resistance and the subjectivity of defining high-uptake regions of interest it seems premature to proceed with selective dose escalation. It would be ideal to perform treatments on a small animal model in order to verify that PET-guided selective escalation confer a benefit in treatment outcome. Unfortunately, using currently available technology, it is not possible to perform intensity modulated radiotherapy (IMRT) treatment of small animal tumor models. However, it is possible to carry out the planning and delivery of CT image-guided selective radiation dose escalation of small animal tumor models using a dedicated CT-guided small animal irradiator such as Small Animal Radiation Research Platform (SARRP) developed by Johns Hopkins University and Xstrahl.

4.2.Small Animal Radiation Research Platform

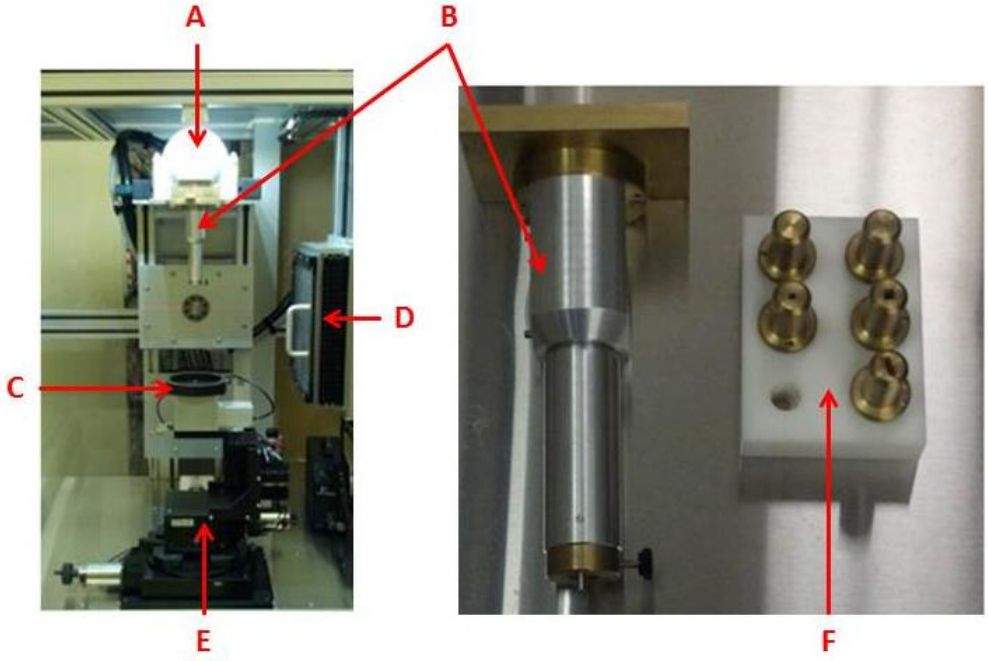

Figure 46: The SARRP (left) system comprised of a dual-filament x-ray tube (A), a collimating cone of 15 mm diameter (B), a rotating couch for the animal to be positioned on (C), a Perking Elmer flat panel detector for acquiring cone-beam CT images (D), a robotic stage capable of shifting the couch in the X, Y, and Z directions (E) and the selection of static collimators (F) which range in size from 5 x 9 mm to 1 x 1 mm

The SARRP system allows for the precise delivery of radiation to a pre-clinical model. Precision irradiation is delivered using small-field (down to 1 x 1 mm) and the rotation of both the gantry-mounted x-ray tube and the animal treatment couch. The system is capable of delivering both static and dynamic beams with a static collimator system with a maximum dose rate of approximately 3.5 Gy per minute. In addition to irradiation capabilities for treatment, the SARRP is also capable of on-board cone-beam CT and portal imaging during treatment. These imaging techniques can be used to guide the delivery of radiation. CT images can be used for treatment planning while portal imaging can be used for online imaging.

The machine consists of a robotic stage and treatment couch which can shift in the X, Y and Z dimensions by approximately 50, 50 and 38 mm with a positional accuracy of .065 mm. The stage is also designed for rotation from -180 degrees to 180 degrees with a default position of 0 degrees and a rotational accuracy of .05 degrees. The gantry of the machine can be rotated from 0 degrees, completely vertical, to approximately 127 degrees. There are two imaging units on board the SARRP, a small CCD camera for portal imaging and minor fluoroscopic imaging as well as a flat panel cone-beam CT imaging detector. The x-ray tube can supply up to 225 kV x-rays using a large 3mm focal spot and 13 mA of current for treatment. Using a smaller .4 mm focal spot, the system produces x-rays in the rage of 50 – 150 kV for imaging. The addition of a Perkins Elmer flat panel detector allows for cone-beam CT images to be acquired with the animal in treatment position (Figure 47) [54] .

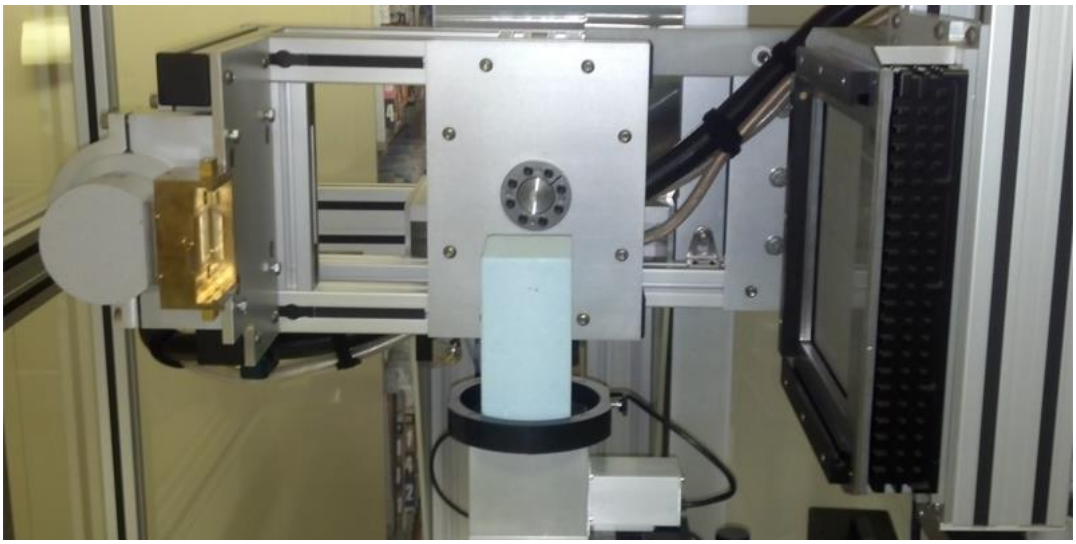

Figure 47: The SARRP in position for cone-beam CT imaging. The lead shield has been removed from the flat panel detectors, the gantry is rotated to 90 degrees and the collimating cone has been removed.

In order to acquire a CT image, the animal and treatment couch are rotated 360 degrees while the x-ray tube and flat-panel detector are kept stationary to acquire projections. Images are

reconstructed in real-time and are made available to a proprietary treatment planning system. The images acquired on the SARRP can then be used to plan treatments to be delivered on the machine. The system in its current form does not employ the use of multi-leaf collimators but uses a system of static collimators that are manually fitted to a collimating cone. The uncollimated field of VCU's SARRP system is approximately 30 x 30 mm. The collimating cone produces a 15 mm diameter circular field. The additional collimators range in size from a 5 x 5 mm collimator to a 1 x 1 mm collimator.

For treatments employing the use of multiple beams, multiple collimators or arcs a SLICER 3D treatment planning system is used. This system uses a fast GPU superposition-convolution algorithm that is detailed in a paper published by Jacques et al. from Johns Hopkins University [Jacques]. This algorithm allows for very quick dose distribution calculations, on the order of tens of seconds, for both static beam treatments and much more complicated coplanar and non-coplanar arc beam deliveries. The fast planning capabilities allow for planning to be completed while the animal is anesthetized on the treatment machine. The combination of this pre-clinical treatment planning system and the image-guided treatment delivery capabilities of the SARRP facilitate pre-clinical radiotherapy research.

4.3.Methods and Materials

4.3.1. Establishing tumor models and growth curves

FaDu human head and neck tumor xenografts were subcutaneously implanted and used as targets for the delivered radiation therapy plans. Tumors were established by inoculating nude mice with .5 *10^6 FaDu cells in the left and right shoulders. All animals maintained in compliance with the guidelines of Virginia Commonwealth University's Institutional Animal

Care and Use Committee. Every two days the tumor size was measured using calipers and the volume was estimated using the formula for a prolate spheroid:

$$\frac{\pi}{6} * Diameter_{Large} * Diameter_{small}^{2}$$

In order to keep measurement errors systematic and prevent adding inter-observer variations, all caliper measurements were performed by the same researcher.

4.3.2. Determining a suitable dose level

Prior to studying the effect of sub-volume dose escalation, the effect of single homogeneous fractions needed to be observed in order to select a suitable dose level for observing the effects of treatments. There has been extensive research on the use of FaDu tumors for fractionated regiments citing $\frac{\alpha}{\beta}$ values of approximately 15 Gy for fractionated treatment regiments in xenograft models [56], [57], [58]. However, there are few studies delivering single fraction large doses to FaDu tumor xenografts. In order to evaluate the response of the FaDu tumors to large single dose fractions, tumor bearing nude mice were treated with single fraction doses of 20, 35, 50 or 60 Gy. The non-coplanar arc capabilities of the SARRP allowed for the distribution of dose over a larger area of skin, preventing severe skin reactions. The flank tumor model also provided easy to access to the target tumor with no major critical structures to be concerned with.

After treatment tumor growth was measured for up to 25 days by caliper. Single fraction 60 Gy homogeneous deliveries showed almost complete regression of the tumor. An additional escalation of dose beyond 60 Gy would not produce observable results. Similarly, the 50 Gy treatments showed immediate tumor response which would not be useful in observing the

response of an additional dose escalation. The 35 Gy treatments showed a continued growth up to 5 days after treatment and then a significant reduction of the tumor volume. Single doses of 20 Gy also showed statistically similar results to that of 35 Gy single fraction treatments. It is likely that he large effect of these single fraction doses would overshadow any potential benefits of the dose escalation. In light of the initial results a homogeneous dose of 10 Gy was also tested for efficacy. It was observed that 10 Gy dose was less effective in controlling tumor growth and seemed to provide a good baseline homogeneous dose for studying the effect of dose escalation (Figure 48).

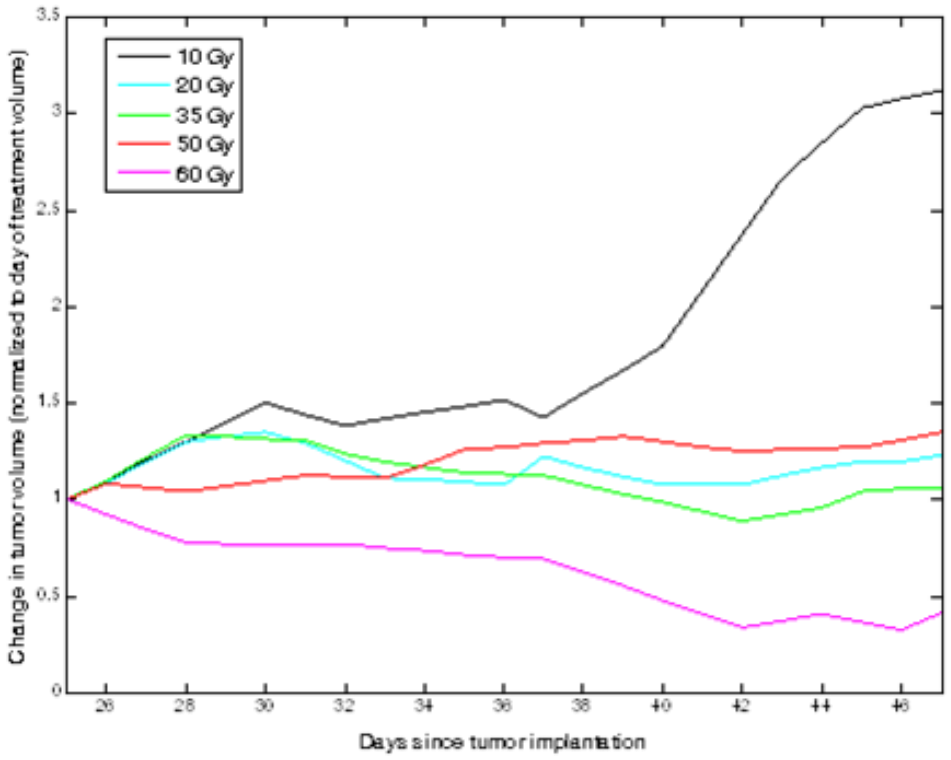

Figure 48: Tumor xenograft growth after treatments of 10, 20, 35, 50 and 60 Gy (normalized to day of treatment volume)

The differences between the effects of doses between 10 and 20 Gy led to the decision of using a homogeneous delivery of 10Gy and a small sub-volume escalation of another 10 Gy in order to view the effects of the dose escalation. Ideally this method would yield results somewhere between the 10 and 20 Gy single fraction treatments.

4.3.3. Small animal FDG PET imaging

On the 24th day after tumor implantation, the animals underwent the same PET/CT imaging procedures as described in the previous chapter. Each animal was fasted for 6 hours prior to tracer injection and imaging. A 60 minute tracer uptake period was allowed prior to scanning during which animals were anesthetized under 3% isoflurane. All animals were positioned on an animal specific pad on which body contours and tumors were marked for repositioning. The animals were imaged using CT at .5mA and 75 kV for 5 minutes and PET images were acquired for 10 minutes. After imaging, animals were allowed to recover and were fed normally.

4.3.4. PET dose escalation

The small animal PET/CT data sets acquired using the Inveon PET/CT scanner were imported into Slicer 3D (http://www.slicer.org/) and the tumors were manually contoured. After contouring, the image sets and contours were imported into Matlab where a custom script analyzed the PET image, comparing the uptake within spherical volumes, representative of the selected 5mm collimator, inside the tumor as defined by manual contouring. The average uptake was determined for every location of the 5mm sphere within the tumor and the sphere containing the highest FDG uptake was designated as the target for the dose escalation. A target PET image set was created by marking the center of the sphere of highest uptake with a pixel of zero

intensity. In this way, an animal specific selective dose escalation plan was made using only the FDG PET information (Figure 49).

.

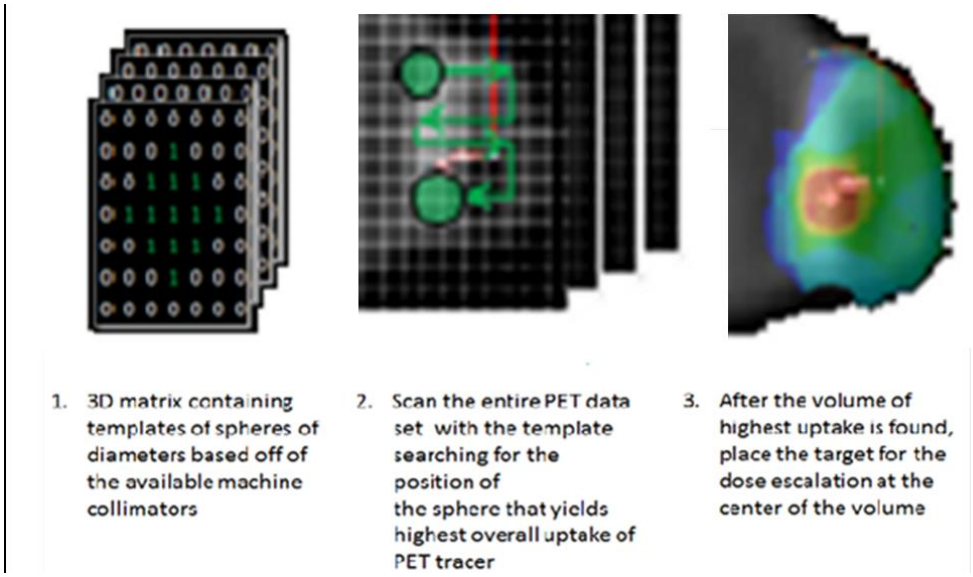

Figure 49: Workflow of determining the volume of highest PET uptake. An example of a binary matrix representative of the collimators (Left) a figure showing a circular template scanned through the area of the tumor (middle) and a planned treatment targeting the volume of highest PET uptake (right)

4.3.5. Treatment delivery

The day following the PET/CT imaging, the 25th day since tumor implantation, animals were irradiated using the SARRP. Animals were anesthetized using ketamine-xylazine and were repositioned on the animal specific pad. The SARRP lasers were used to align the animals and the on board flat panel detector was used to acquire cone-beam CT projections of the animal at 1 mA and 65 kV. After CT acquisition the images were opened in the SARRP graphical user interface (GUI) treatment planning plug-in and the delivery of homogeneous dose of 10 Gy was planned. A 15mm diameter circular collimator was positioned over the tumor to cover the entire

tumor volume as defined by CT while avoiding internal structures. During the delivery of the homogeneous 10 Gy dose, the PET/CT image set used for planning had to be registered to the CT data acquired on the SARRP in order to alleviate the effects of mispositioning and anatomical changes (Figure 50).

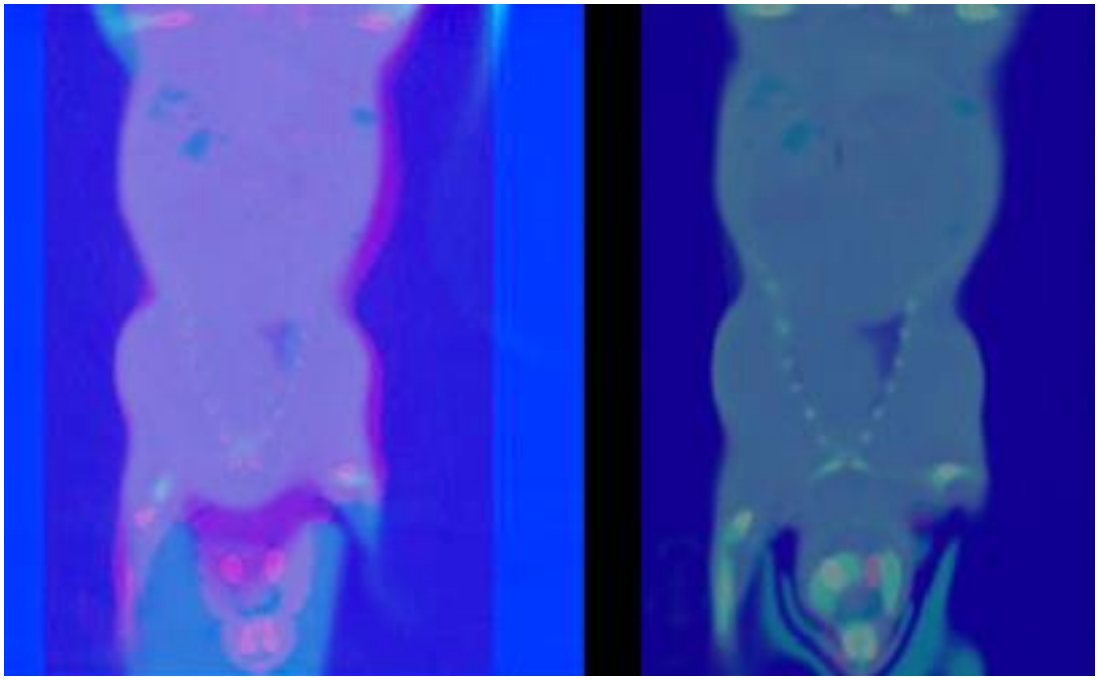

Figure 50: The alignment between treatment CT (in red) and planning CT (in blue) before (left) and after image registration (right)

The BRAINSFit algorithm was chosen for the purpose of registering the planning CT to the SARRP CT because of the algorithm's ability to handle small local PET deformations without introducing errors larger than 1.5 voxels. This algorithm is available in the Slicer 3D package used for treatment planning on the SARRP. The efficiency of this algorithm allowed for carrying out registration of the planning CT to the treatment position CT while the animal was

anesthetized. The only inputs that were required for registration were the planning and treatment position CT data sets. Registration of the images was initialized by means of manual rigid registration. The SARRP CT images were not normalized to Hounsfield units so in order to achieve the most accurate image registration histogram matching was used. The auto-ROI feature was used to generate the required ROIs for the registration and the ROIauto variables were set to .9mm for expansion and contraction of structure contour borders for small animal images instead of the 9mm used for human images. The transform produced by registering the planning CT to the SARRP CT was then applied to the planning PET image. In this way the PET image is registered with the SARRP CT from the treatment day and the offset isocenter for dose escalation can be placed over the area of highest PET uptake. Using non-coplanar arc delivery a 5mm approximately spherical dose of 10 Gy was then delivered to the selected sub-volume of the tumor.

4.3.6. Pilot study: PET dose escalation vs. arbitrary escalation

In order to illustrate the use of the proposed methodology, a pilot study was carried out comparing PET- and CT-guided dose escalations. Animals were randomly assigned to one of the two cohorts. The CT-guided cohort received a 10 Gy irradiation to the entire tumor and an additional 10 Gy irradiation to a 5 mm, approximately spherical, volume at the center of the tumor placed using only CT anatomy. The PET-guided cohort received the same 10 Gy initial irradiation as the previous cohort and a 10 Gy escalation to a 5mm sub-volume defined by the region of the highest FDG uptake within the tumor. A control cohort receiving no radiation was previously established for purposes of analysis and comparison. The measured change in tumor size was used as a surrogate for the ability of each treatment to control tumor growth (Figure 51).

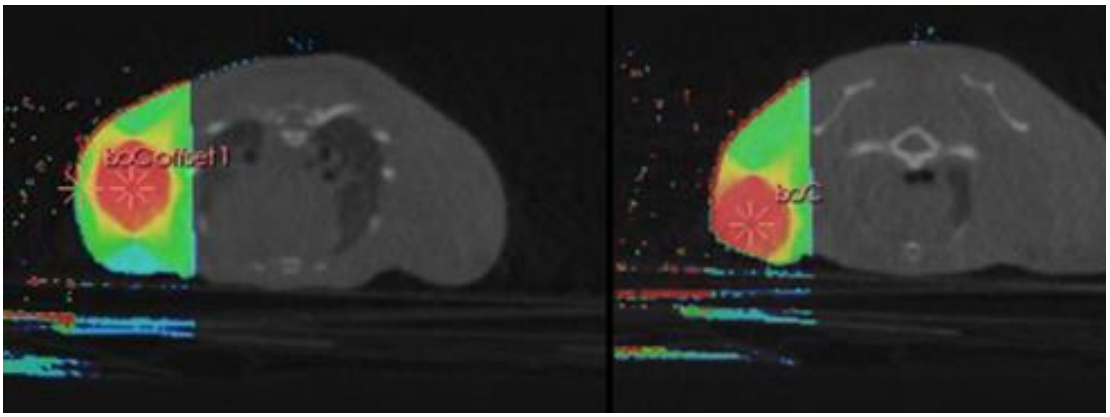

Figure 51: An arbitarary dose escalation of the center of a tumor (Left) and a dose escalation positioned on the volume of highest PET uptake (Right).

4.3.7. Post-treatment tumor growth and analysis

After treatment, the tumor growth was evaluated by caliper measurements. The animals were monitored for up to 50 days after treatment provided that the tumors did not grow beyond the limits established by VCU's animal care policies and that the animal was not experiencing any weakness or discomfort. The growth of the tumors was determined and the percent change in volume compared to the day of treatment volume was calculated and plotted (Figure 52).

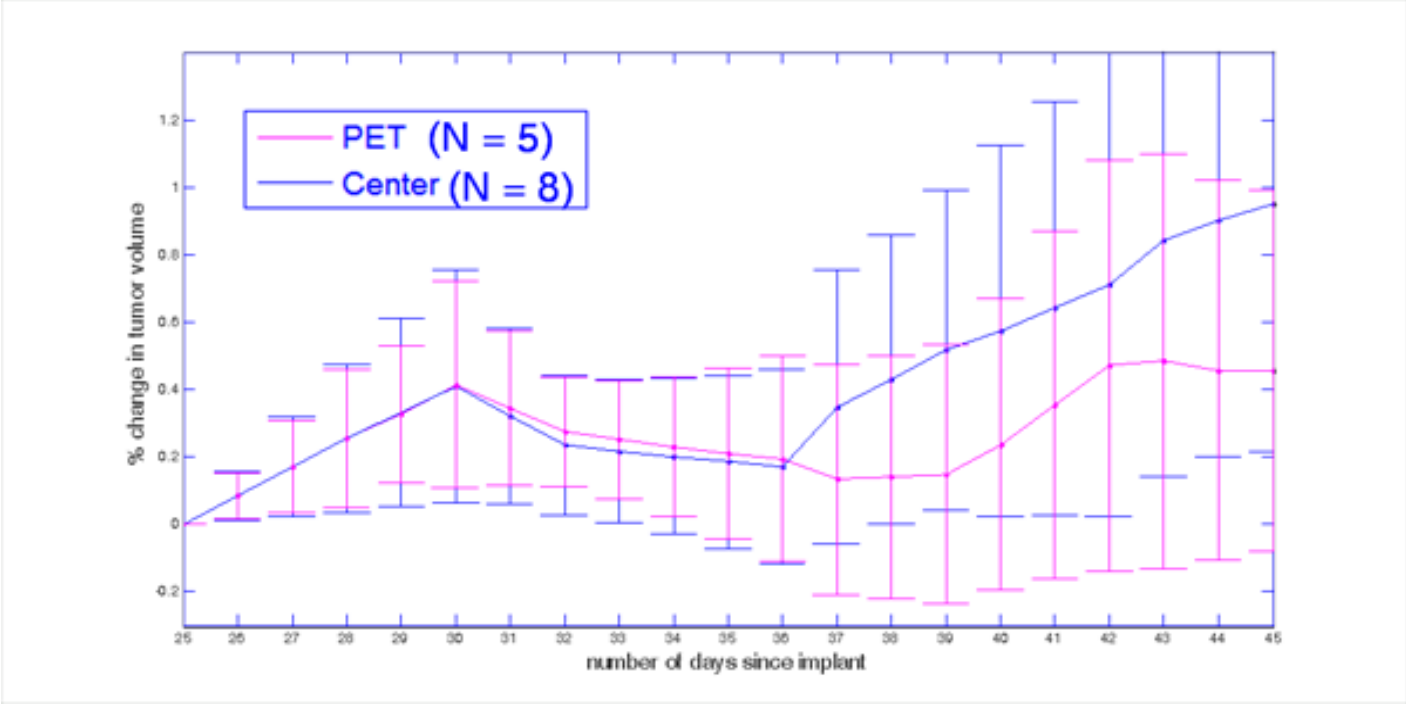

Figure 52: The percent change in tumor volume in tumors treated with PET dose escalations (Pink) and center of tumor dose escalations (blue)

In order to assess the benefit of each treatment, the delay in tumor growth was used. The time necessary for the tumor to achieve an increase in volume of 25, 40 and 50 percent relative to its pre-regression size was recorded and compared between the two cohorts.

4.4. Results

The average time for a tumor treated with a PET-guided dose escalation to reach a 25, 40 and 50% increase in tumor volume was 14 +/- 6.8, 16.2 +/- 5.1 and 16.7 +/- 5.4 days after initial treatment. The same times for escalations to the center of the tumor were 8.6 +/- 7.1, 11.3 +/- 7 and 14.3 +/- 7.14 days after initial treatment. On average the PET-guided dose escalation delayed tumor growth by 2 to 6 days when compared with dose escalations to the geometric center of the tumor (53).

Additionally, the PET-guided dose escalation controlled tumor growth so well in one tumor that an increase in volume of 25 % was never achieved in the 50 day observation period.

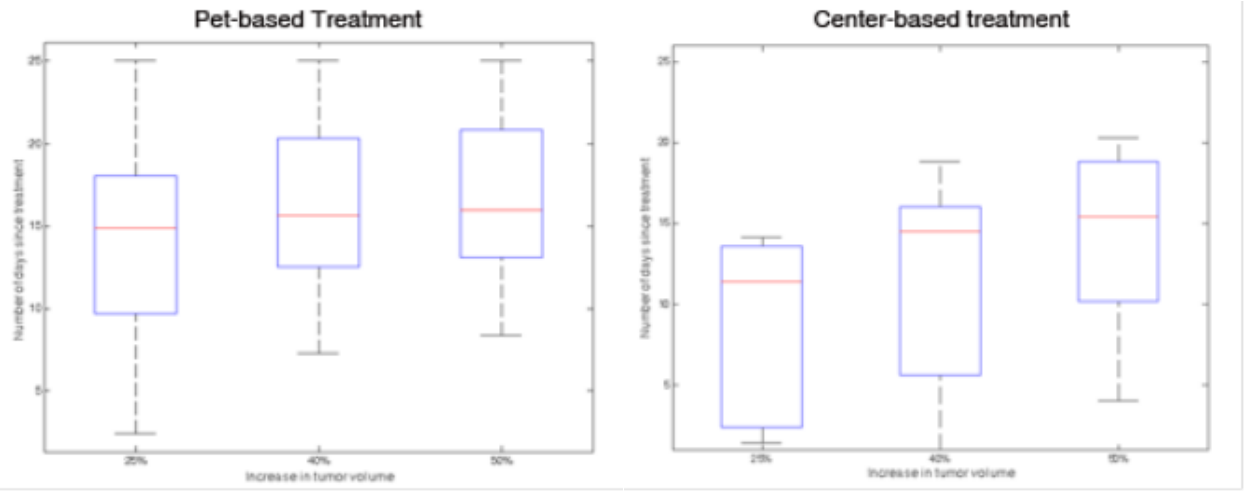

Figure 53: The average time required for tumors treated with PET-guided escalation (left) and CT-guided escalation (right) to reach a 25, 40 and 50% increase in volume

In general, both the PET-targeted and Center-targeted treatments were successful in delaying tumor growth. However, the number of tumors in each arm, 5 for PET and 8 for center boosting respectively, was too few to establish a statistically significant benefit for the PET-guided methodology.

Chapter 5: DISCUSSION

This thesis has set the ground work for the planning and delivery of PET-guided selective dose escalations for a pre-clinical research model. Additionally a pilot study was carried out comparing the efficacy of FDG -guided dose escalation with a dose escalation placed blindly in the geometric center of the tumor. While data from the trial was not statistically significant, the results of monitoring change in tumor volume implied a more favorable tumor control using the PET-guided methods. This method can be easily adapted for other PET tracers and other methods of image guidance using functional and anatomical imaging.

Currently the SARRP treatment planning system only allows for manual forward planning which hinders the delivery planning of advanced techniques like dose paint-by-numbers. Ford et al. have shown that it is feasible to commission clinically available treatment planning software with inverse planning capabilities for use with the SARRP [59]. More advanced treatments would require extensive pre-planning and adapting of the pre-plan to the day of treatment anatomy. The imprecision of repositioning small animals for treatment would also confound the delivery of complicated plans. Introducing an isoflurane system to the SARRP would extend the time the animal remains anesthetized and could make planning these more complicated plans feasible without extensive pre-planning.

Another potential limitation of this work includes the assessment of tumor growth using caliper measurements. If more precise measurements of tumor growth were required, any imaging technique could be used to acquire measurements of the tumor growth. There are drawbacks, however, to repeat imaging of small animal tumor models. In the case of CT, repeat imaging every over a month as a surrogate for physical measurement would result in a significant accumulation of dose to the animal which would confound the ability to gauge the

efficacy of treatments. In addition, while MRI would seem to be ideal for this scenario as it uses no ionizing radiation, it is also important to note that mice do not tolerate anesthesia well and repeatedly anesthetizing mice could severely weaken or even kill the animal.

Despite limitations in the currently available technology, this research provides methodology for pre-clinical research of biologically-guided selective dose escalation treatments. In the near future there will be many upgrades available for the SARRP system including new imaging methodologies and dynamic collimator systems. This protocol can also be easily adapted to include the addition of other imaging modalities, multi-leaf collimator systems, and any other relevant improvements in the machine and software. Using this approach with one or more PET tracers, data for biologically-guided treatment could be amassed prior to moving to clinical trials, leading to more successful trials and a greater acceptance of biological-guidance in radiotherapy.

Bibliography

[1] J. Bernier, E. J. Hall, and A. Giaccia, "Radiation oncology: a century of achievements," *Nat. Rev. Cancer*, vol. 4, no. 9, pp. 737–747, Sep. 2004.

[2] H. J. W. L. Aerts, P. Lambin, and D. D. Ruysscher, "FDG for dose painting: a rational choice," *Radiother. Oncol. J. Eur. Soc. Ther. Radiol. Oncol.*, vol. 97, no. 2, pp. 163–164, Nov. 2010.

[3] R. L. Bakst, N. Lee, D. G. Pfister, M. J. Zelefsky, M. A. Hunt, D. H. Kraus, and S. L. Wolden, "Hypofractionated dose-painting intensity modulated radiation therapy with chemotherapy for nasopharyngeal carcinoma: a prospective trial," *Int. J. Radiat. Oncol. Biol. Phys.*, vol. 80, no. 1, pp. 148–153, May 2011.

[4] D. Pulte and H. Brenner, "Changes in survival in head and neck cancers in the late 20th and early 21st century: a period analysis," *Oncologist*, vol. 15, no. 9, pp. 994–1001, 2010.

[5] M. A. Deveau, S. R. Bowen, D. C. Westerly, and R. Jeraj, "Feasibility and sensitivity study of helical tomotherapy for dose painting plans," *Acta Oncol.*, vol. 49, no. 7, pp. 991–996, Oct. 2010.

[6] S. M. Bentzen and V. Gregoire, "Molecular-imaging-based dose painting - a novel paradigm for radiation therapy prescription," *Semin. Radiat. Oncol.*, vol. 21, no. 2, pp. 101–110, Apr. 2011.

[7] A. Pugachev, S. Ruan, S. Carlin, S. M. Larson, J. Campa, C. C. Ling, and J. L. Humm, "Dependence of FDG uptake on tumor microenvironment," *Int. J. Radiat. Oncol. Biol. Phys.*, vol. 62, no. 2, pp. 545–553, Jun. 2005.

[8] M. Axente, J. He, C. P. Bass, J. I. Hirsch, G. Sundaresan, J. Williamson, J. Zweit, and A. Pugachev, "Tumour microenvironment heterogeneity affects the perceived spatial concordance between the intratumoural patterns of cell proliferation and 18F-fluorothymidine uptake," *Radiother. Oncol. J. Eur. Soc. Ther. Radiol. Oncol.*, vol. 105, no. 1, pp. 49–56, Oct. 2012.

[9] C. C. Ling, J. Humm, S. Larson, H. Amols, Z. Fuks, S. Leibel, and J. A. Koutcher, "Towards multidimensional radiotherapy (MD-CRT): biological imaging and biological conformality," *Int. J. Radiat. Oncol. Biol. Phys.*, vol. 47, no. 3, pp. 551–560, Jun. 2000.

[10] A. Rahmim and H. Zaidi, "PET versus SPECT: strengths, limitations and challenges," *Nucl. Med. Commun.*, vol. 29, no. 3, pp. 193–207, Mar. 2008.

[11] C. S. Levin and E. J. Hoffman, "Calculation of positron range and its effect on the fundamental limit of positron emission tomography system spatial resolution," *Phys. Med. Biol.*, vol. 44, no. 3, p. 781, Mar. 1999.

[12] T. Barwick, B. Bencherif, J. M. Mountz, and N. Avril, "Molecular PET and PET/CT imaging of tumour cell proliferation using F-18 fluoro-L-thymidine: a comprehensive evaluation," *Nucl. Med. Commun.*, vol. 30, no. 12, pp. 908–917, Dec. 2009.

[13] K. Herrmann, K. Ott, A. K. Buck, F. Lordick, D. Wilhelm, M. Souvatzoglou, K. Becker, T. Schuster, H.-J. Wester, J. R. Siewert, M. Schwaiger, and B. J. Krause, "Imaging gastric cancer with PET and the radiotracers 18F-FLT and 18F-FDG: a comparative analysis," *J. Nucl. Med. Off. Publ. Soc. Nucl. Med.*, vol. 48, no. 12, pp. 1945–1950, Dec. 2007.

[14] S. M. Larson and H. Schoder, "New PET tracers for evaluation of solid tumor response to therapy," *Q. J. Nucl. Med. Mol. Imaging Off. Publ. Ital. Assoc. Nucl. Med. Aimn Int. Assoc. Radiopharm. Iar Sect. Soc. Radiopharm. Chem. Biol.*, vol. 53, no. 2, pp. 158–166, Apr. 2009.

[15] K. A. Krohn, F. O'Sullivan, J. Crowley, J. F. Eary, H. M. Linden, J. M. Link, D. A. Mankoff, M. Muzi, J. G. Rajendran, A. M. Spence, and K. R. Swanson, "Challenges in clinical studies with multiple imaging probes," *Nucl. Med. Biol.*, vol. 34, no. 7, pp. 879–885, Oct. 2007.
[16] D. De Ruysscher, S. Wanders, A. Minken, A. Lumens, J. Schiffelers, C. Stultiens, S. Halders, L. Boersma, A. van Baardwijk, T. Verschueren, M. Hochstenbag, G. Snoep, B. Wouters, S. Nijsten, S. M. Bentzen, M. van Kroonenburgh, M. Ollers, and P. Lambin, "Effects of radiotherapy planning with a dedicated combined PET-CT-simulator of patients with non-small cell lung cancer on dose limiting normal tissues and radiation dose-escalation: a planning study," *Radiother. Oncol. J. Eur. Soc. Ther. Radiol. Oncol.*, vol. 77, no. 1, pp. 5–10, Oct. 2005.
[17] A. van Der Wel, S. Nijsten, M. Hochstenbag, R. Lamers, L. Boersma, R. Wanders, L. Lutgens, M. Zimny, S. M. Bentzen, B. Wouters, P. Lambin, and D. De Ruysscher, "Increased therapeutic ratio by 18FDG-PET CT planning in patients with clinical CT stage N2-N3M0 non-small-cell lung cancer: a modeling study," *Int. J. Radiat. Oncol. Biol. Phys.*, vol. 61, no. 3, pp. 649–655, Mar. 2005.
[18] D. L. Schwartz, E. C. Ford, J. Rajendran, B. Yueh, M. D. Coltrera, J. Virgin, Y. Anzai, D. Haynor, B. Lewellen, D. Mattes, P. Kinahan, J. Meyer, M. Phillips, M. Leblanc, K. Krohn, J. Eary, and G. E. Laramore, "FDG-PET/CT-guided intensity modulated head and neck radiotherapy: a pilot investigation," *Head Neck*, vol. 27, no. 6, pp. 478–487, Jun. 2005.
[19] K. S. Tralins, J. G. Douglas, K. J. Stelzer, D. A. Mankoff, D. L. Silbergeld, R. C. Rostomily, S. Hummel, J. Scharnhorst, K. A. Krohn, A. M. Spence, and R. Rostomilly, "Volumetric analysis of 18F-FDG PET in glioblastoma multiforme: prognostic information and possible role in definition of target volumes in radiation dose escalation," *J. Nucl. Med. Off. Publ. Soc. Nucl. Med.*, vol. 43, no. 12, pp. 1667–1673, Dec. 2002.
[20] D. A. Mankoff and F. Dehdashti, "Imaging Tumor Phenotype: 1 Plus 1 Is More Than 2," *J. Nucl. Med.*, vol. 50, no. 10, pp. 1567–1569, Oct. 2009.
[21] V. Wyawahare, P. Patil, and H. Abhyankar, "Image Registration Techniques: An overview," *Int. J. Signal Process. Process.*, vol. 2, no. 3, Sep. 2009.
[22] B. Zitová and J. Flusser, "Image registration methods: a survey," *Image Vis. Comput.*, vol. 21, pp. 977–1000, 2003.
[23] W. Crum, "Non-rigid image registration: theory and practice.," *Br. J. Radiol.*, vol. 77, pp. S140 – S153, 2004.
[24] R. M. Kessler, J. R. Ellis Jr, and M. Eden, "Analysis of emission tomographic scan data: limitations imposed by resolution and background," *J. Comput. Assist. Tomogr.*, vol. 8, no. 3, pp. 514–522, Jun. 1984.
[25] M. R. Kaus, K. K. Brock, V. Pekar, L. A. Dawson, A. M. Nichol, and D. A. Jaffray, "Assessment of a Model-Based Deformable Image Registration Approach for Radiation Therapy Planning," *Int. J. Radiat. Oncol. Biol. Phys.*, vol. 68, no. 2, Jun. 2007.
[26] L. Veugen, "Image Registration Techniques, Benchmarking, Strategy," Brigham and Women's Hospital, Boston, MA, Jul-2010.
[27] J. P. Thirion, "Image matching as a diffusion process: an analogy with Maxwell's demons," *Med. Image Anal.*, vol. 2, no. 3, pp. 243–260, Sep. 1998.
[28] D. L. G. Hill, P. G. Batchelor, M. Holden, and D. J. Hawkes, "Medical image registration," *Phys. Med. Biol.*, vol. 46, no. 3, p. R1, Mar. 2001.

[29] S. Klein, M. Staring, and J. P. W. Pluim, "Evaluation of optimization methods for nonrigid medical image registration using mutual information and B-splines," *Ieee Trans. Image Process. Publ. Ieee Signal Process. Soc.*, vol. 16, no. 12, pp. 2879–2890, Dec. 2007.
[30] F. Maes, A. Collignon, D. Vandermeulen, G. Marchal, and P. Suetens, "Multimodality image registration by maximization of mutual information," *Ieee Trans. Med. Imaging*, vol. 16, no. 2, pp. 187–198, 1997.
[31] P. A. Andres and R. A. Isoardi, "Using ITK platform for medical image registration," *J. Phys. Conf. Ser.*, vol. 90, no. 1, p. 012056, Nov. 2007.
[32] H. Ólafsdóttir, T. A. Darvann, N. V. Hermann, E. Oubel, B. K. Ersbøll, A. F. Frangi, P. Larsen, C. A. Perlyn, G. M. Morriss-Kay, and S. Kreiborg, "Computational mouse atlases and their application to automatic assessment of craniofacial dysmorphology caused by the Crouzon mutation Fgfr2C342Y," *J. Anat.*, vol. 211, no. 1, pp. 37–52, 2007.
[33] S. K. Boyd, S. Moser, M. Kuhn, R. J. Klinck, P. L. Krauze, R. Müller, and J. A. Gasser, "Evaluation of Three-dimensional Image Registration Methodologies for In Vivo Micro-computed Tomography," *Ann. Biomed. Eng.*, vol. 34, no. 10, pp. 1587–1599, Sep. 2006.
[34] R. Kashani, M. Hub, J. M. Balter, M. L. Kessler, L. Dong, L. Zhang, L. Xing, Y. Xie, D. Hawkes, J. A. Schnabel, J. McClelland, S. Joshi, Q. Chen, and W. Lu, "Objective assessment of deformable image registration in radiotherapy: a multi-institution study," *Med. Phys.*, vol. 35, no. 12, pp. 5944–5953, Dec. 2008.
[35] S. Klein, M. Staring, K. Murphy, M. A. Viergever, and J. Pluim, "elastix: A Toolbox for Intensity-Based Medical Image Registration," *Ieee Trans. Med. Imaging*, vol. 29, no. 1, pp. 196–205, Jan. 2010.
[36] A. F. Shields, J. R. Grierson, B. M. Dohmen, H.-J. Machulla, J. C. Stayanoff, J. M. Lawhorn-Crews, J. E. Obradovich, O. Muzik, and T. J. Mangner, "Imaging proliferation in vivo with [F-18]FLT and positron emission tomography," *Nat. Med.*, vol. 4, no. 11, pp. 1334–1336, Nov. 1998.
[37] A. F. Shields, "PET Imaging with 18F-FLT and Thymidine Analogs: Promise and Pitfalls," *J. Nucl. Med.*, vol. 44, no. 9, pp. 1432–1434, Sep. 2003.
[38] J. Toyohara, A. Waki, S. Takamatsu, Y. Yonekura, Y. Magata, and Y. Fujibayashi, "Basis of FLT as a cell proliferation marker: comparative uptake studies with [3H]thymidine and [3H]arabinothymidine, and cell-analysis in 22 asynchronously growing tumor cell lines," *Nucl. Med. Biol.*, vol. 29, no. 3, pp. 281–287, Apr. 2002.
[39] M. Muzi, H. Vesselle, J. R. Grierson, D. A. Mankoff, R. A. Schmidt, L. Peterson, J. M. Wells, and K. A. Krohn, "Kinetic Analysis of 3′-Deoxy-3′-Fluorothymidine PET Studies: Validation Studies in Patients with Lung Cancer," *J. Nucl. Med.*, vol. 46, no. 2, pp. 274–282, Feb. 2005.
[40] E. G. C. Troost, J. Bussink, P. J. Slootweg, W. J. M. Peeters, M. A. W. Merkx, A. J. van der Kogel, W. J. G. Oyen, and J. H. A. M. Kaanders, "Histopathologic validation of 3'-deoxy-3'-18F-fluorothymidine PET in squamous cell carcinoma of the oral cavity," *J. Nucl. Med. Off. Publ. Soc. Nucl. Med.*, vol. 51, no. 5, pp. 713–719, May 2010.
[41] C. C. Zhang, Z. Yan, W. Li, K. Kuszpit, C. L. Painter, Q. Zhang, P. B. Lappin, T. Nichols, M. E. Lira, T. Affolter, N. R. Fahey, C. Cullinane, M. Spilker, K. Zasadny, P. O'Brien, D. Buckman, A. Wong, and J. G. Christensen, "[18F]FLT–PET Imaging Does Not Always 'Light Up' Proliferating Tumor Cells," *Clin. Cancer Res.*, vol. 18, no. 5, pp. 1303–1312, Mar. 2012.

[42] D. C. P. Cobben, P. H. Elsinga, H. J. Hoekstra, A. J. H. Suurmeijer, W. Vaalburg, B. Maas, P. L. Jager, and H. M. J. Groen, "Is 18F-3'-fluoro-3'-deoxy-L-thymidine useful for the staging and restaging of non-small cell lung cancer?," *J. Nucl. Med. Off. Publ. Soc. Nucl. Med.*, vol. 45, no. 10, pp. 1677–1682, Oct. 2004.
[43] A. van Waarde, D. C. P. Cobben, A. J. H. Suurmeijer, B. Maas, W. Vaalburg, E. F. J. de Vries, P. L. Jager, H. J. Hoekstra, and P. H. Elsinga, "Selectivity of 18F-FLT and 18F-FDG for differentiating tumor from inflammation in a rodent model," *J. Nucl. Med. Off. Publ. Soc. Nucl. Med.*, vol. 45, no. 4, pp. 695–700, Apr. 2004.
[44] H. Dittmann, B. M. Dohmen, F. Paulsen, K. Eichhorn, S. M. Eschmann, M. Horger, M. Wehrmann, H. J. Machulla, and R. Bares, "[18F]FLT PET for diagnosis and staging of thoracic tumours," *Eur. J. Nucl. Med. Mol. Imaging*, vol. 30, no. 10, pp. 1407–1412, Oct. 2003.
[45] J. R. Bading and A. F. Shields, "Imaging of cell proliferation: status and prospects," *J. Nucl. Med. Off. Publ. Soc. Nucl. Med.*, vol. 49 Suppl 2, p. 64S–80S, Jun. 2008.
[46] B. Xu, Z. Guan, C. Liu, R. Wang, D. Yin, J. Zhang, Y. Chen, S. Yao, M. Shao, H. Wang, and J. Tian, "Can multimodality imaging using 18F-FDG/18F-FLT PET/CT benefit the diagnosis and management of patients with pulmonary lesions?," *Eur. J. Nucl. Med. Mol. Imaging*, vol. 38, no. 2, pp. 285–292, Feb. 2011.
[47] A. Salskov, V. S. Tammisetti, J. Grierson, and H. Vesselle, "FLT: measuring tumor cell proliferation in vivo with positron emission tomography and 3'-deoxy-3'-[18F]fluorothymidine," *Semin. Nucl. Med.*, vol. 37, no. 6, pp. 429–439, Nov. 2007.
[48] H. L. van Westreenen, D. C. P. Cobben, P. L. Jager, H. M. van Dullemen, J. Wesseling, P. H. Elsinga, and J. T. Plukker, "Comparison of 18F-FLT PET and 18F-FDG PET in esophageal cancer," *J. Nucl. Med. Off. Publ. Soc. Nucl. Med.*, vol. 46, no. 3, pp. 400–404, Mar. 2005.
[49] W. Chen, T. Cloughesy, N. Kamdar, N. Satyamurthy, M. Bergsneider, L. Liau, P. Mischel, J. Czernin, M. E. Phelps, and D. H. S. Silverman, "Imaging proliferation in brain tumors with 18F-FLT PET: comparison with 18F-FDG," *J. Nucl. Med. Off. Publ. Soc. Nucl. Med.*, vol. 46, no. 6, pp. 945–952, Jun. 2005.
[50] H. Hoshikawa, Y. Nishiyama, T. Kishino, Y. Yamamoto, R. Haba, and N. Mori, "Comparison of FLT-PET and FDG-PET for visualization of head and neck squamous cell cancers," *Mol. Imaging Biol. Mib Off. Publ. Acad. Mol. Imaging*, vol. 13, no. 1, pp. 172–177, Feb. 2011.
[51] S. R. Bowen, R. J. Chappell, S. M. Bentzen, M. A. Deveau, L. J. Forrest, and R. Jeraj, "Spatially resolved regression analysis of pre-treatment FDG, FLT and Cu-ATSM PET from post-treatment FDG PET: An exploratory study," *Radiother. Oncol.*, vol. 105, no. 1, pp. 41–48, Oct. 2012.
[52] B. Vanderstraeten, W. Duthoy, W. De Gersem, W. De Neve, and H. Thierens, "[18F]fluoro-deoxy-glucose positron emission tomography ([18F]FDG-PET) voxel intensity-based intensity-modulated radiation therapy (IMRT) for head and neck cancer," *Radiother. Oncol. J. Eur. Soc. Ther. Radiol. Oncol.*, vol. 79, no. 3, pp. 249–258, Jun. 2006.
[53] I. Madani, W. Duthoy, C. Derie, W. De Gersem, T. Boterberg, M. Saerens, F. Jacobs, V. Grégoire, M. Lonneux, L. Vakaet, B. Vanderstraeten, W. Bauters, K. Bonte, H. Thierens, and W. De Neve, "Positron emission tomography-guided, focal-dose escalation using intensity-modulated radiotherapy for head and neck cancer," *Int. J. Radiat. Oncol. Biol. Phys.*, vol. 68, no. 1, pp. 126–135, May 2007.

[54] J. Wong, E. Armour, P. Kazanzides, I. Iordachita, E. Tryggestad, H. Deng, M. Matinfar, C. Kennedy, Z. Liu, T. Chan, O. Gray, F. Verhaegen, T. McNutt, E. Ford, and T. L. DeWeese, "A high resolution small animal radiation research platform (SARRP) with x-ray tomographic guidance capabilities," *Int. J. Radiat. Oncol. Biol. Phys.*, vol. 71, no. 5, pp. 1591–1599, Aug. 2008.
[55] R. Jacques, R. Taylor, J. Wong, and T. McNutt, "Towards real-time radiation therapy: GPU accelerated superposition/convolution," *Comput. Methods Programs Biomed.*, vol. 98, no. 3, pp. 285–292, Jun. 2010.
[56] M. Baumann, W. DuBois, and H. D. Suit, "Response of Human Squamous Cell Carcinoma Xenografts of Different Sizes to Irradiation: Relationship of Clonogenic Cells, Cellular Radiation Sensitivity in Vivo, and Tumor Rescuing Units," *Radiation Research: Official Journal of the Radiation Research Society*, 07-May-2010. [Online]. Available: http://www.rrjournal.org/doi/abs/10.2307/3577740. [Accessed: 26-Jun-2013].
[57] A. L. Zietman, H. D. Suit, K. N. Tomkinson, H. D. Thames, and R. S. Sedlacek, "The response of two human tumor xenografts to fractionated irradiation. The derivation of alpha/beta ratios from growth delay, tumor control, and in vitro cell survival assays," *Int. J. Radiat. Oncol. Biol. Phys.*, vol. 18, no. 3, pp. 569–575, Mar. 1990.
[58] M. Stuschke, V. Budach, W. Budach, H. J. Feldmann, and H. Sack, "Radioresponsiveness, sublethal damage repair and stem cell rate in spheroids from three human tumor lines: comparison with xenograft data," *Int. J. Radiat. Oncol. Biol. Phys.*, vol. 24, no. 1, pp. 119–126, 1992.
[59] E. C. Ford, P. Achanta, D. Purger, M. Armour, J. Reyes, J. Fong, L. Kleinberg, K. Redmond, J. Wong, M. H. Jang, H. Jun, H.-J. Song, and A. Quinones-Hinojosa, "Localized CT-guided irradiation inhibits neurogenesis in specific regions of the adult mouse brain," *Radiat. Res.*, vol. 175, no. 6, pp. 774–783, Jun. 2011.

Appendix I

In order to appropriately quantify the success of deformable registration algorithms within a tumor, external markers had to be introduced to the tumor. The selection of an appropriate marker is outlined in this appendix. Table I lists the tested materials, the linear attenuation coefficients, the material thicknesses, the exponential photon attenuation for various energies.

		energy	(KeV)					
	40	60	80	70			att at 60 KeV	att at 70 KeV
material	m/p(40)	m/p(60)	m/p(80)	m/p(70)	Density	width(for 22g)	N/No	N/No
al	0.565	0.277	0.201	0.239	2.69	0.04	0.941017069	0.97461145
si	0.693	0.319	0.233	0.276	2.32	0.04	0.937713888	0.974712425
cu	4.88	1.6	0.768	1.184	8.94	0.04	0.174629621	0.654817702
h2o	0.267	0.205	0.185	0.195	1	0.04	0.989376829	0.992230341
bone	0.511	0.273	0.209	0.241	1.85	0.04	0.962892022	0.982324085
poly	0.216	0.186	0.173	0.1795	1.06	0.04	0.99088341	0.992418089
Polyvinylidene Flouride	0.256	0.189	0.167	0.178	1.78	0.017	0.992283367	0.9946282
Nylon	0.247	0.19	0.169	0.1795	1.15	0.023	0.993488145	0.995263478
AL .9 and Cu .1	0.998	0.409	0.257	0.333	3.315	0.04	0.876047645	0.956804876
thin copper	4.88	1.6	0.768	1.184	8.94	0.037	0.199048573	0.675945032
titanium dioxide	1.43	0.536	0.31	0.423	4.23	0.02	0.886053453	0.964846942
copper&zinc mix	1.84	0.748	0.461	0.6045	3.684	0.01	0.9344608	0.977976361
steel								
Aluminum Manganese	5.60E-01	2.76E-01	2.01E-01	2.38E-01	2.69	0.04	0.94148295	0.974674373

Table 1: The percent transmission for a photon beam of a specified energy through a marker material

In addition to the listed markers, catheters filled solutions of cesium iodine were also tested. All markers were injected into the center of a phantom comprised of approximately 5 mm of steak.

Phantoms were imaged at energies of 60 and 70 KeV for the purpose of establishing the extent of CT artifact. Figures 54 – 57 depict various markers imaged in the phantom.

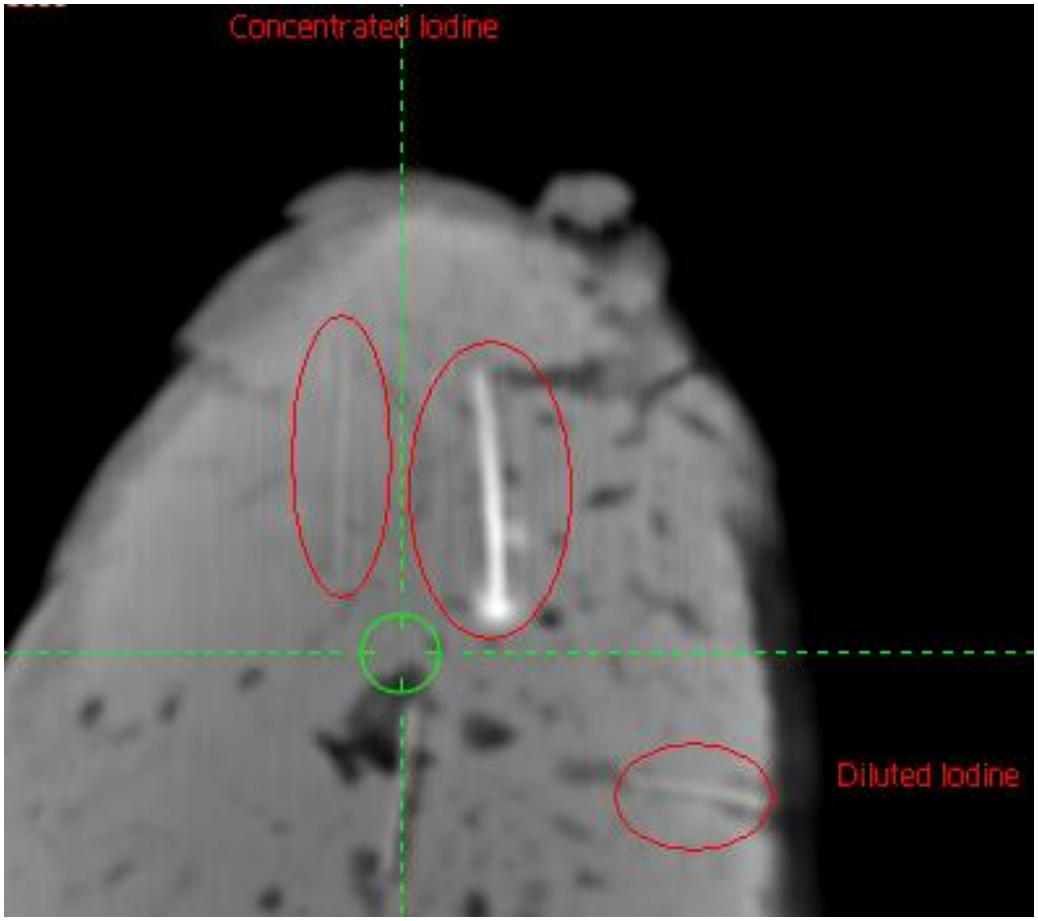

Figure 54: A CT image of catheters containing various concentrations of iodine

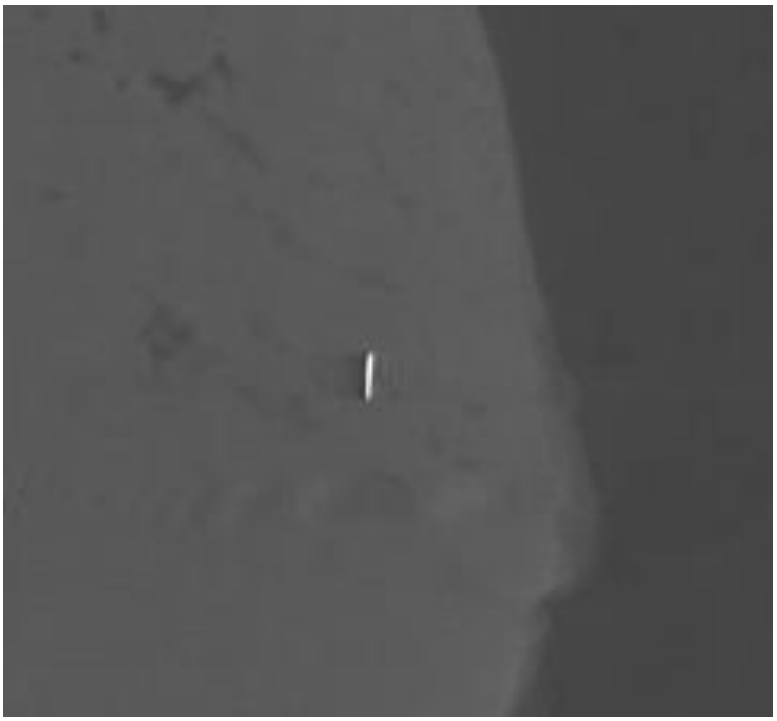

Figure 55: Metal artifact caused by a stainless steel acupuncture needle

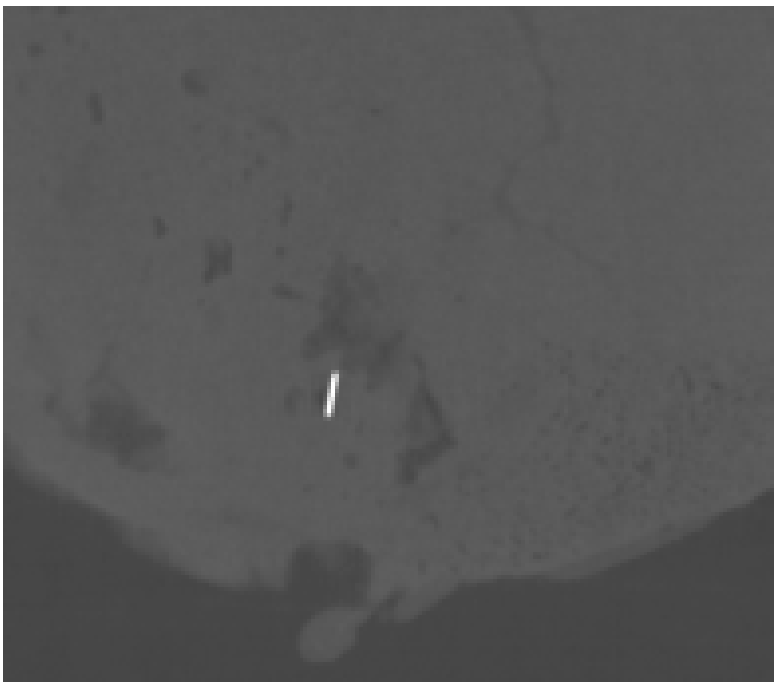

Figure 56: The image of a copper composite magnet wire

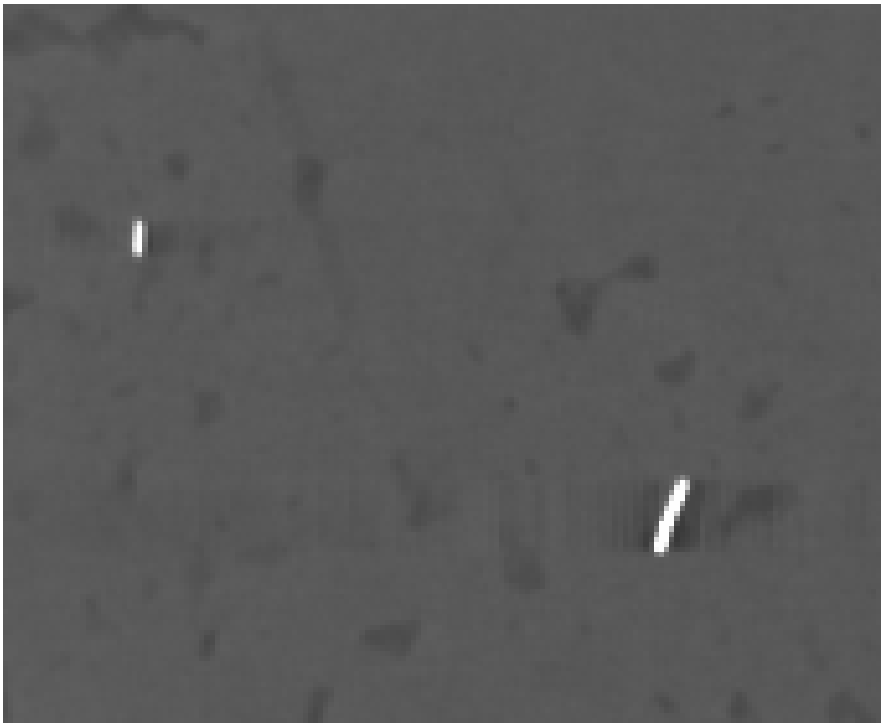

Figure 57: Metal artifact introduced by a 32 gauge steel wire (left) and a 22 gauge copper wire (right)

The composite copper wire was originally assumed to be completely copper and is used for very small scale electronics like headphones, mp3 players and cellphones. After comparing the images of the 22 gauge copper wire and the 22 gauge composite wire it became obvious that the wire was not as attenuating as the copper wire. The copper composite wire provided the least artifact and was the clearest marker with the exception of iodine. Unfortunately the difficulty of producing iodine filled catheters at sizes of approximately a millimeter and the difficulty implanting the flexible catheters in the tumors prevented their use. As such the composite copper was selected for experiments in chapter 2 of the dissertation.

Appendix II

This appendix shows the results of the voxel by voxel analysis of FDG and FLT images using the original reconstructed PET voxel size of .77 mm. These images were not used for primary analysis because they exhibit a pixel size smaller than the inherent resolution of the PET images. This could potentially cause problems in the correlation analysis. The analysis, however, was performed on these images retrospectively for the purposes of comparison.

Slicer 3 scatterplots using the original .77 mm voxel sizes

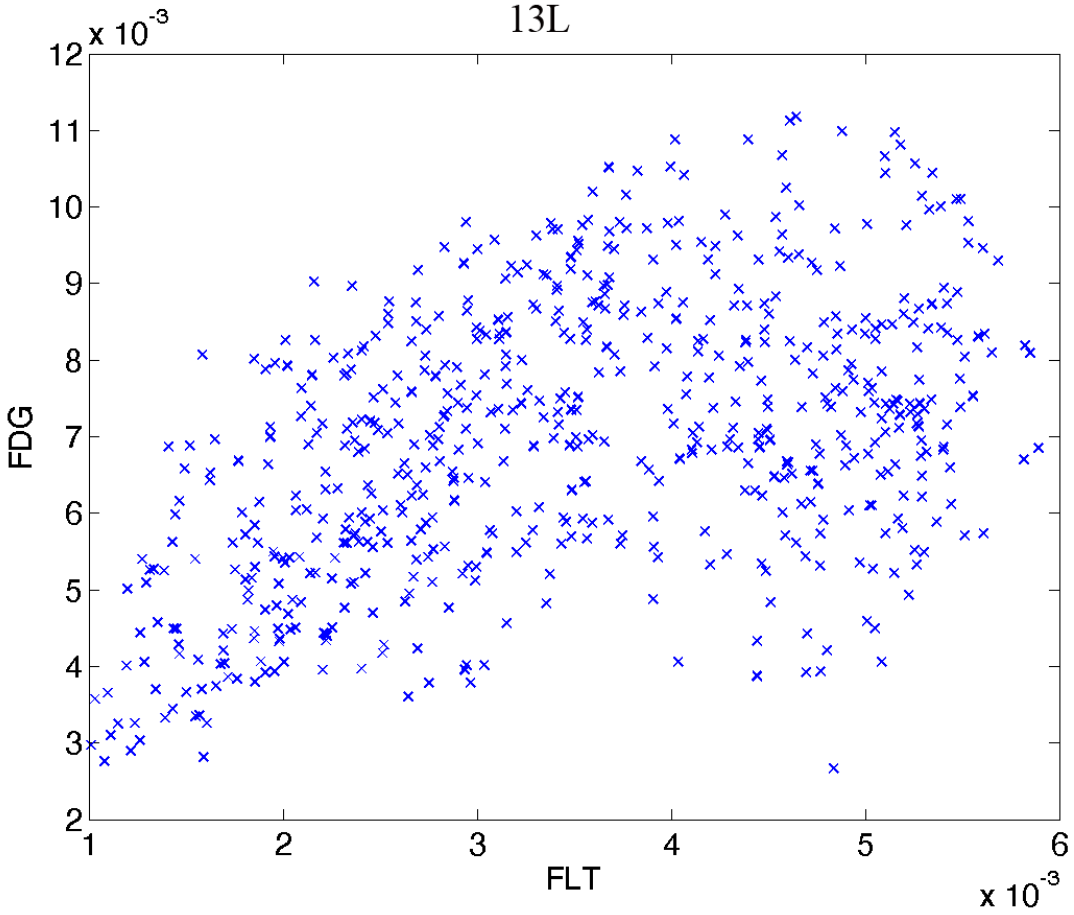

Figure 1: A scatterplot showing the changes in FDG and FLT on a voxel by voxel scale for tumor 13L with a reconstructed PET resolution of .77 mm

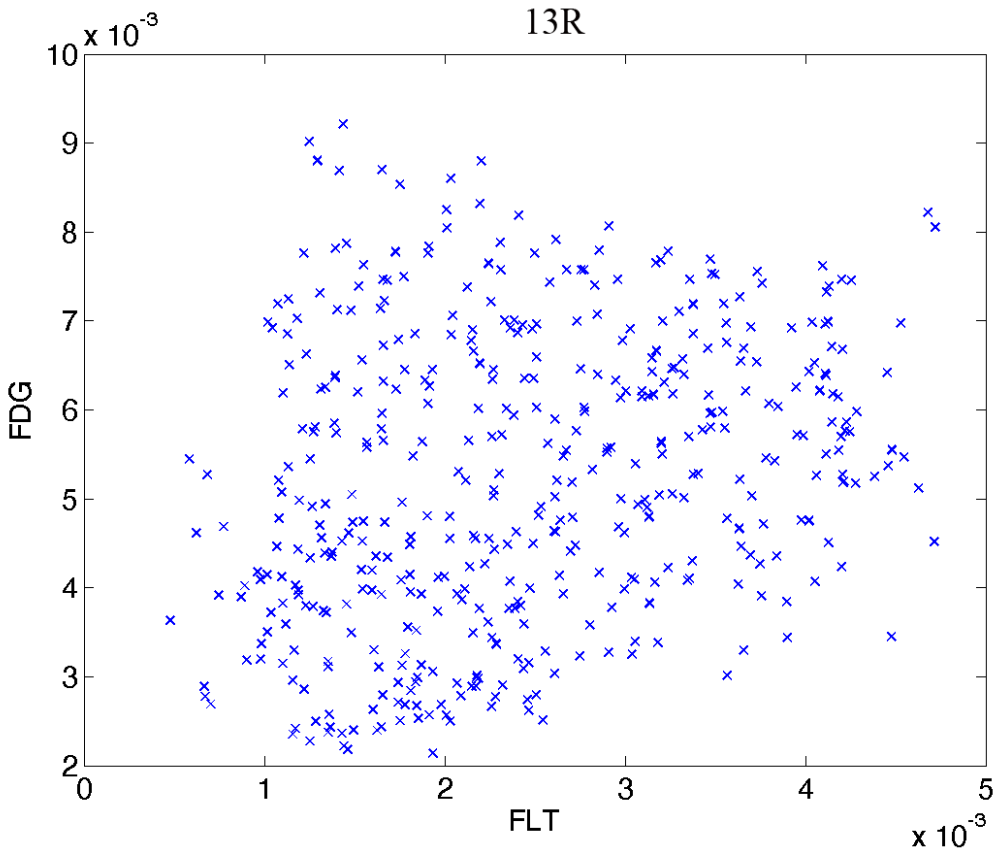

Figure 2: A scatterplot showing the changes in FDG and FLT on a voxel by voxel scale for tumor 13R with a reconstructed PET resolution of .77 mm

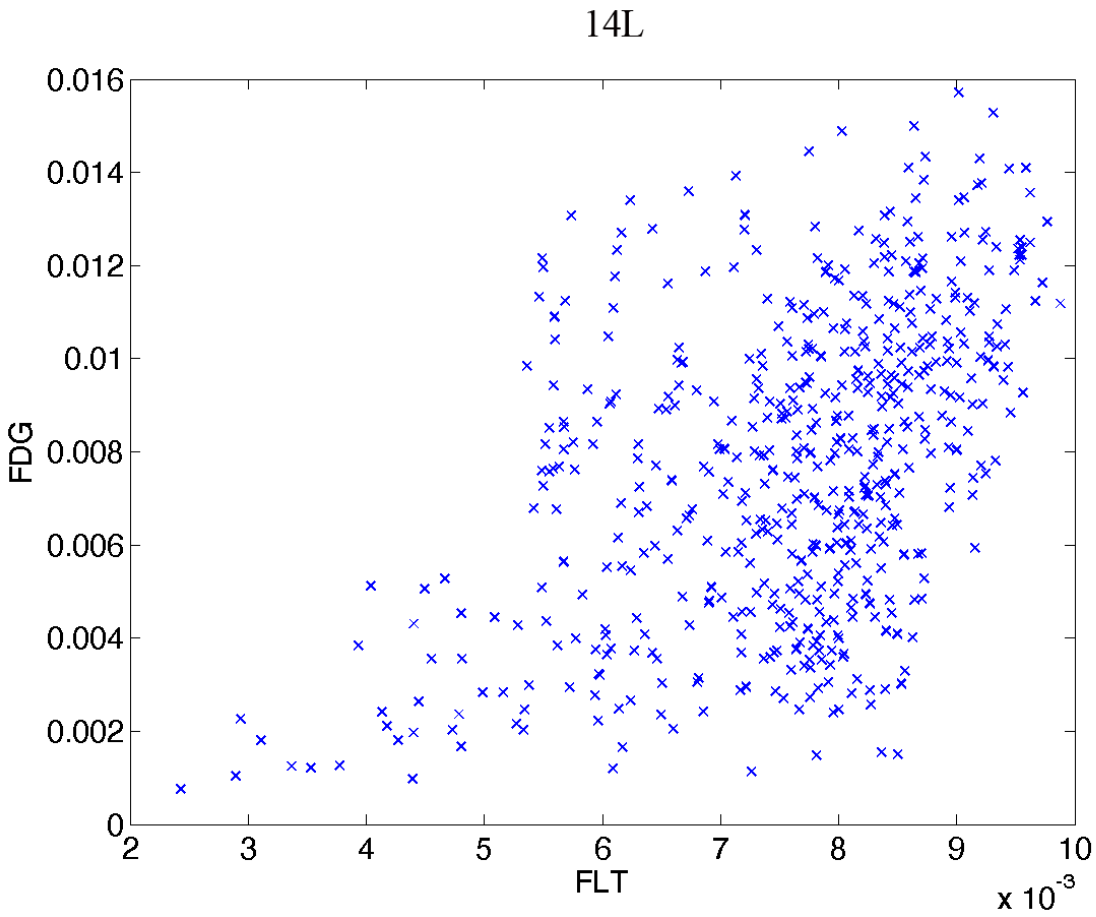

Figure 3: A scatterplot showing the changes in FDG and FLT on a voxel by voxel scale for tumor 14L with a reconstructed PET resolution of .77 mm

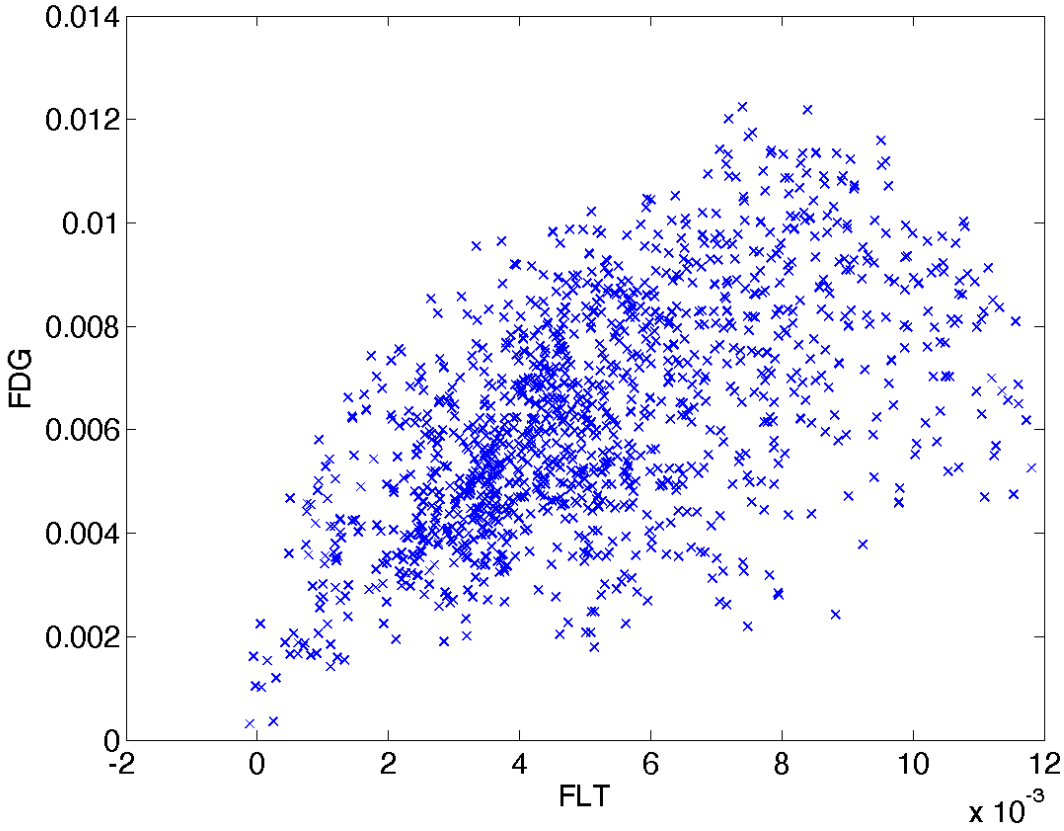

Figure 4: A scatterplot showing the changes in FDG and FLT on a voxel by voxel scale for tumor 14R with a reconstructed PET resolution of .77 mm

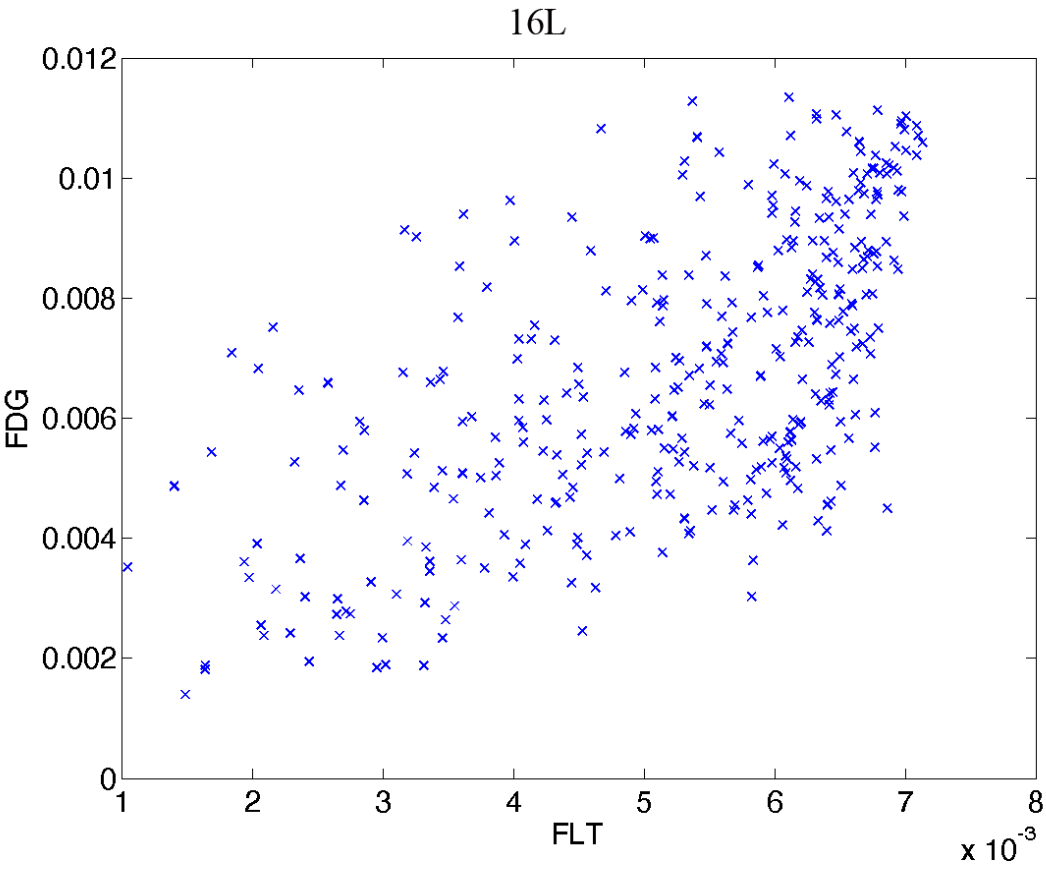

Figure 5: A scatterplot showing the changes in FDG and FLT on a voxel by voxel scale for tumor 16L with a reconstructed PET resolution of .77 mm

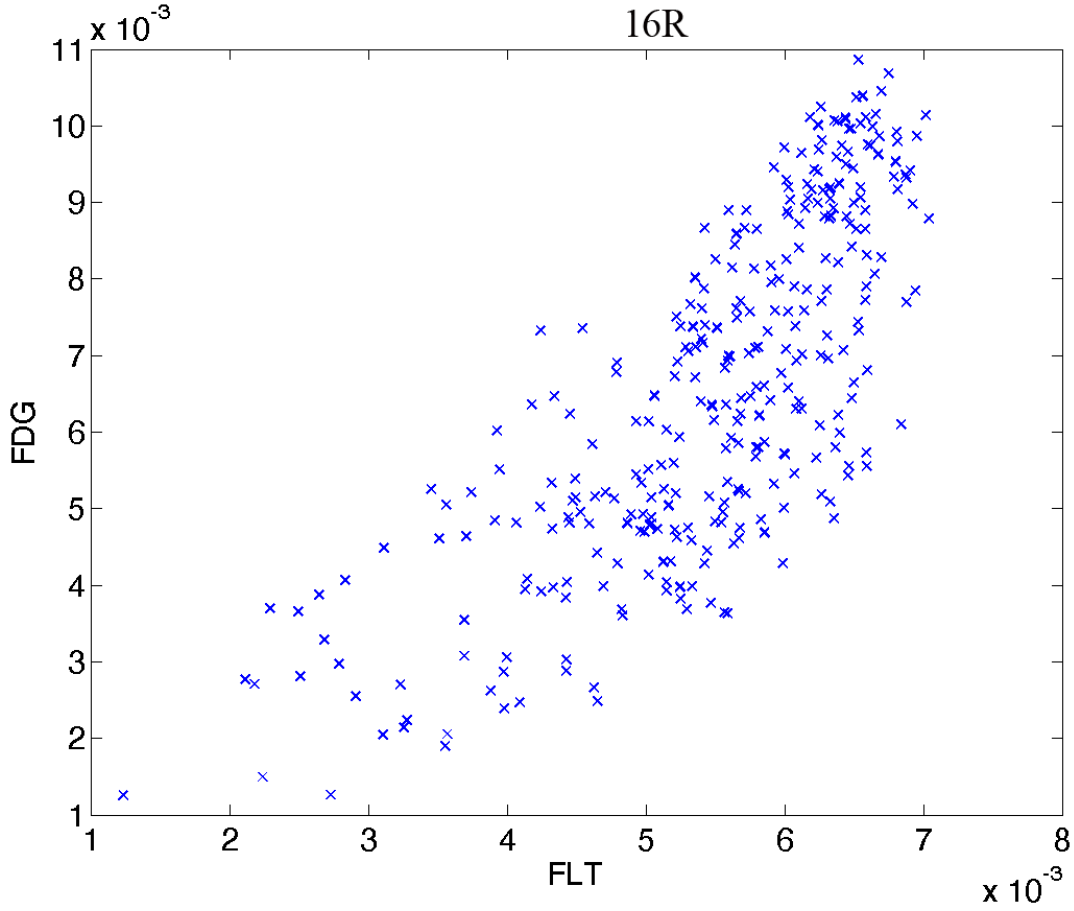

Figure 6: A scatterplot showing the changes in FDG and FLT on a voxel by voxel scale for tumor 16R with a reconstructed PET resolution of .77 mm

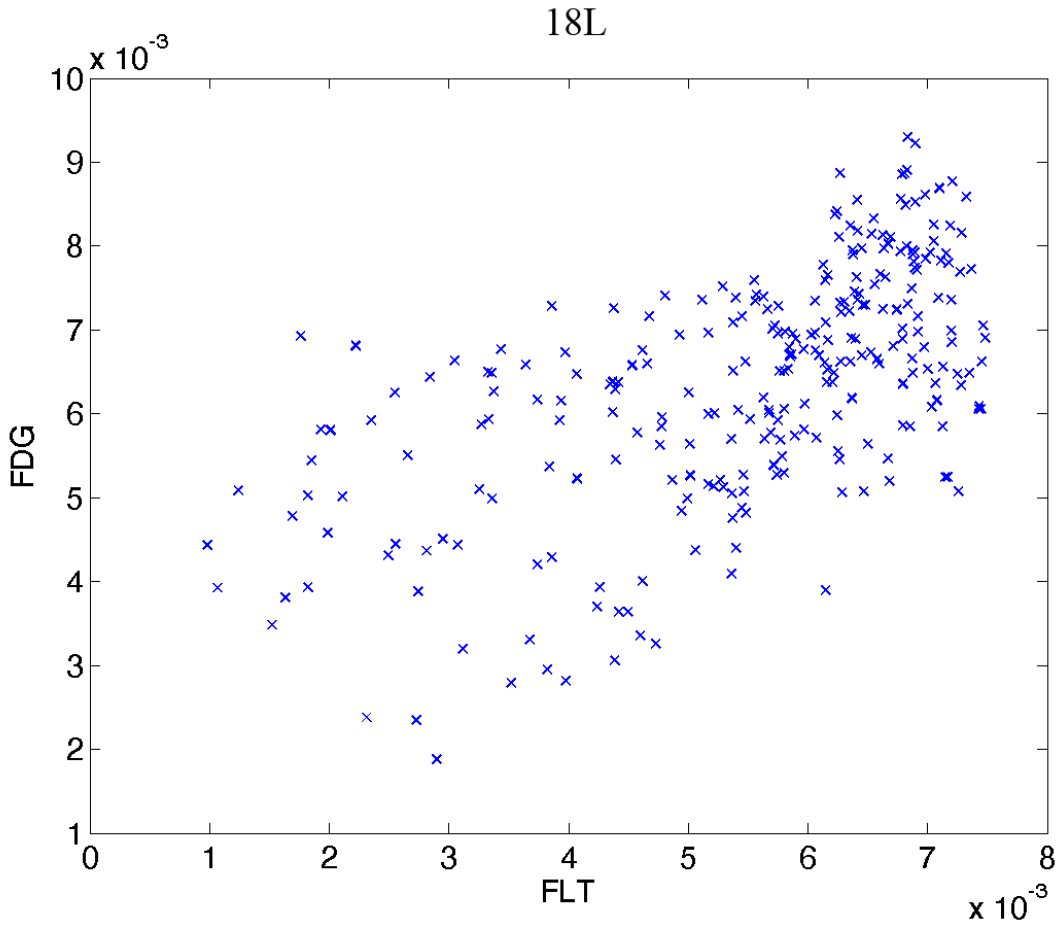

Figure 7: A scatterplot showing the changes in FDG and FLT on a voxel by voxel scale for tumor 18L with a reconstructed PET resolution of .77 mm

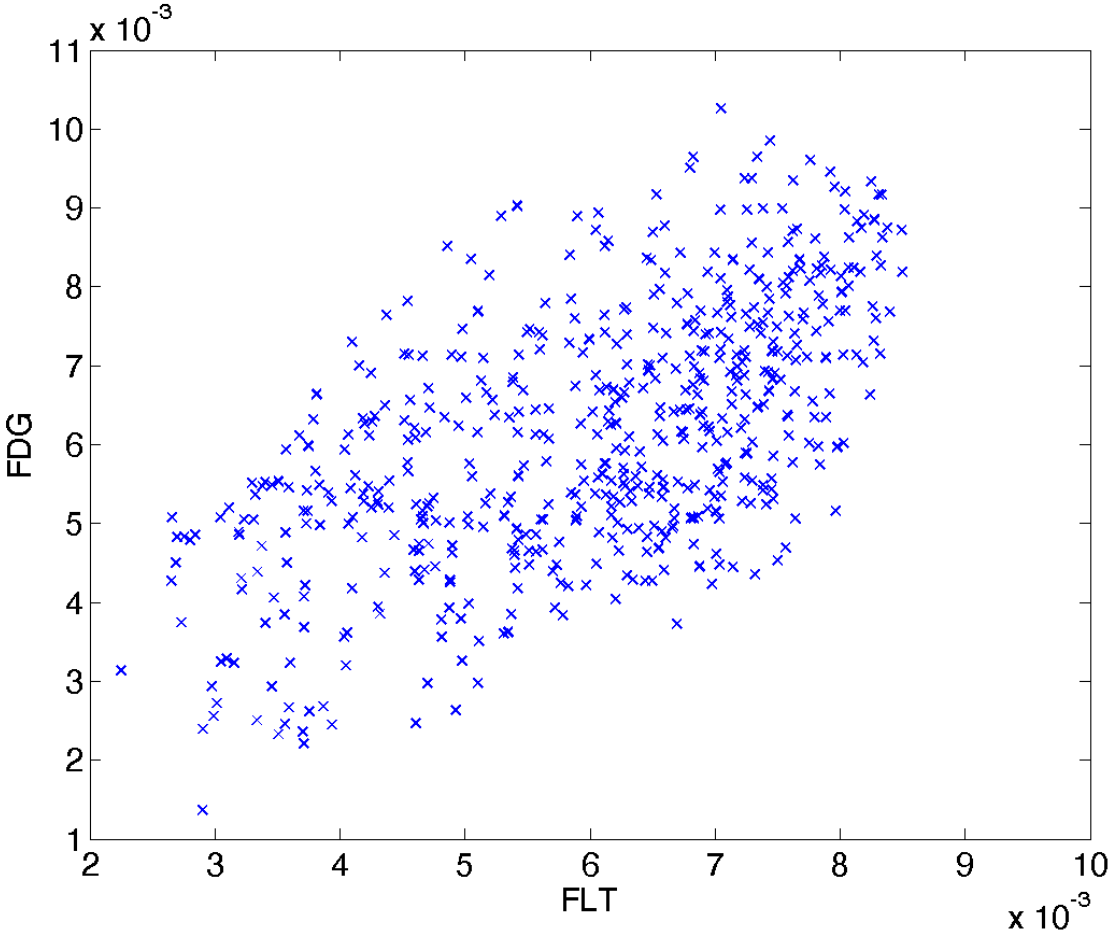

Figure 8: A scatterplot showing the changes in FDG and FLT on a voxel by voxel scale for tumor 18R with a reconstructed PET resolution of .77 mm

Slicer 3 binned graphs using the original .77 mm voxel sizes

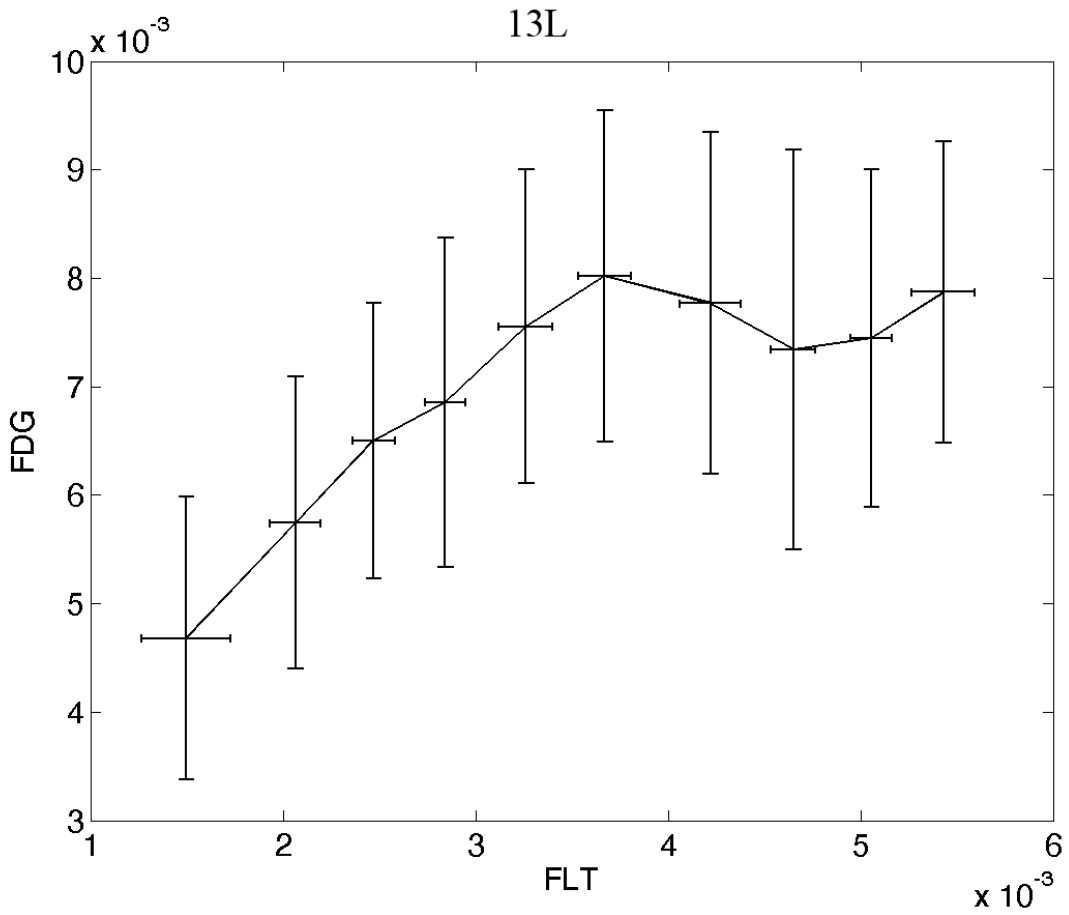

Figure 9: A binned graph showing the changes in FDG and FLT on a voxel by voxel scale for tumor 13L with a reconstructed PET resolution of .77 mm

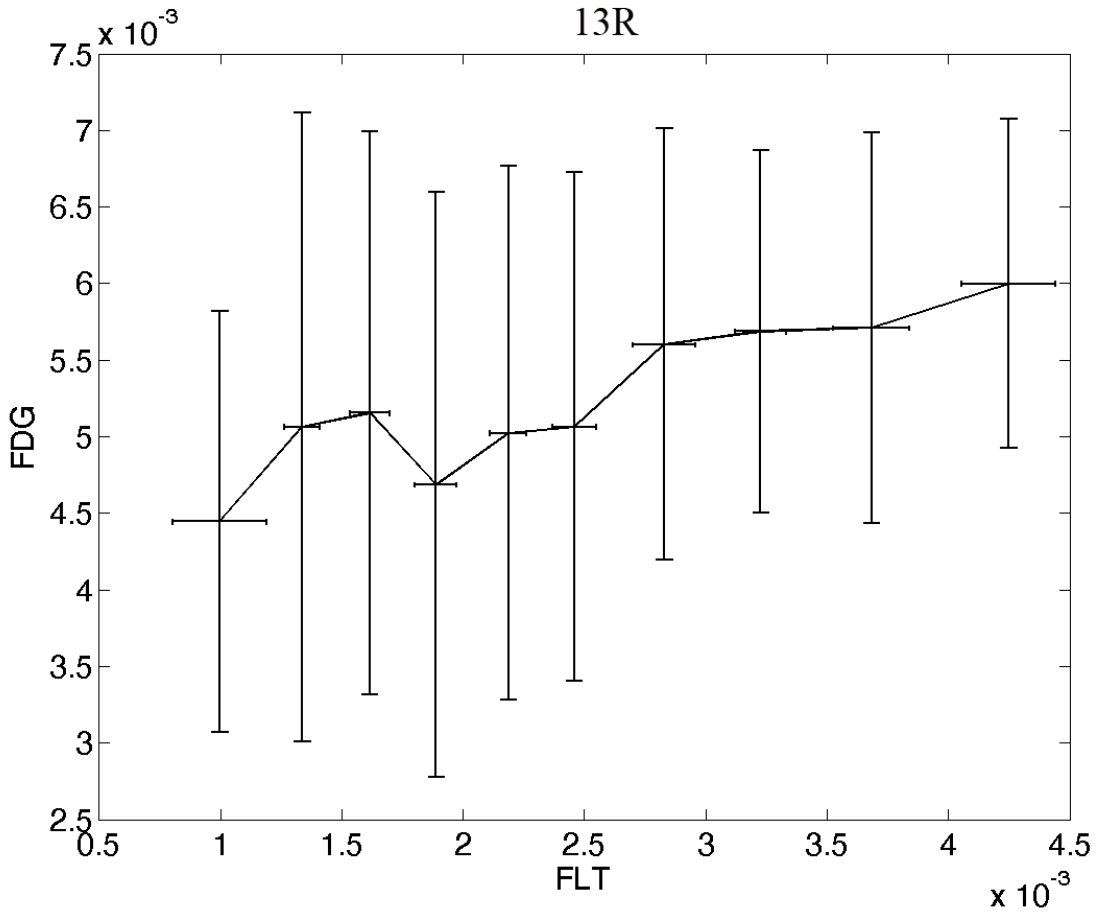

Figure 10: A binned graph showing the changes in FDG and FLT on a voxel by voxel scale for tumor 13R with a reconstructed PET resolution of .77 mm

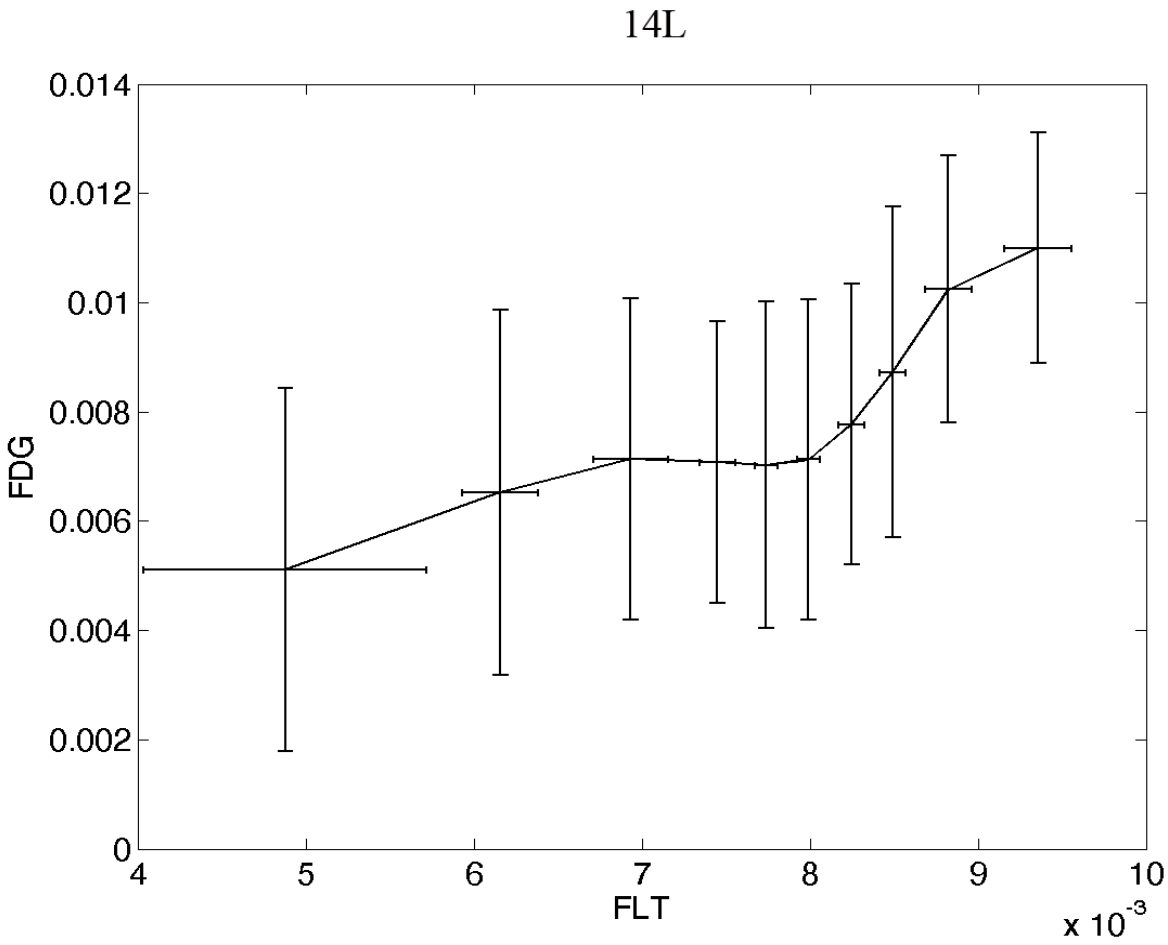

Figure 11: A binned graph showing the changes in FDG and FLT on a voxel by voxel scale for tumor 14L with a reconstructed PET resolution of .77 mm

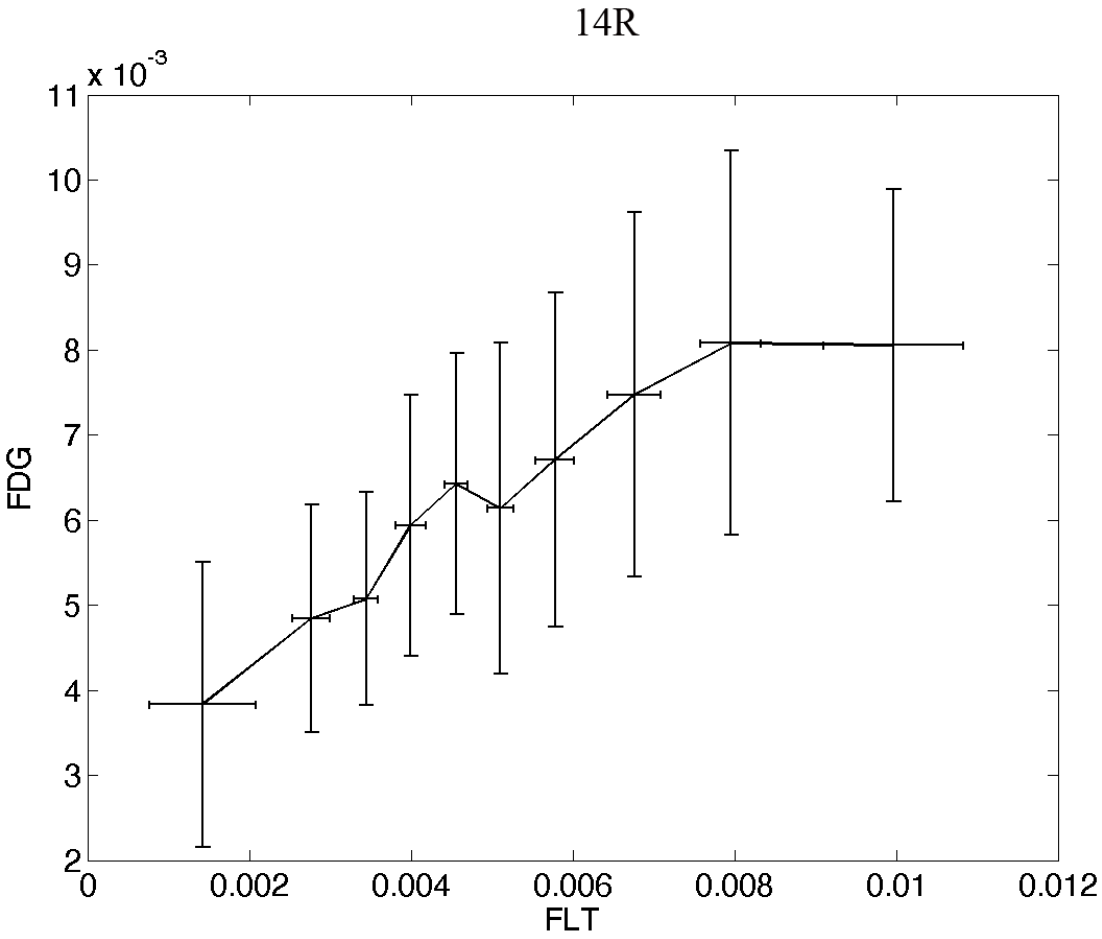

Figure 12: A binned graph showing the changes in FDG and FLT on a voxel by voxel scale for tumor 14R with a reconstructed PET resolution of .77 mm

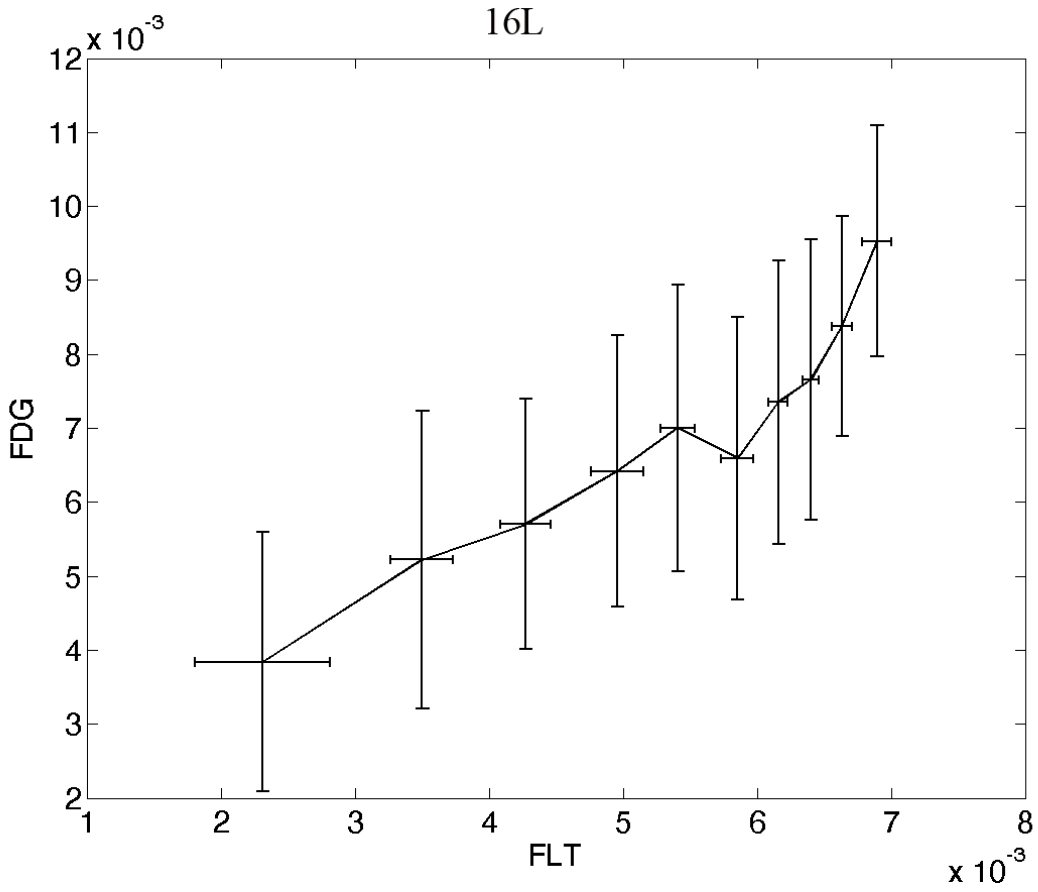

Figure 13: A binned graph showing the changes in FDG and FLT on a voxel by voxel scale for tumor 16L with a reconstructed PET resolution of .77 mm

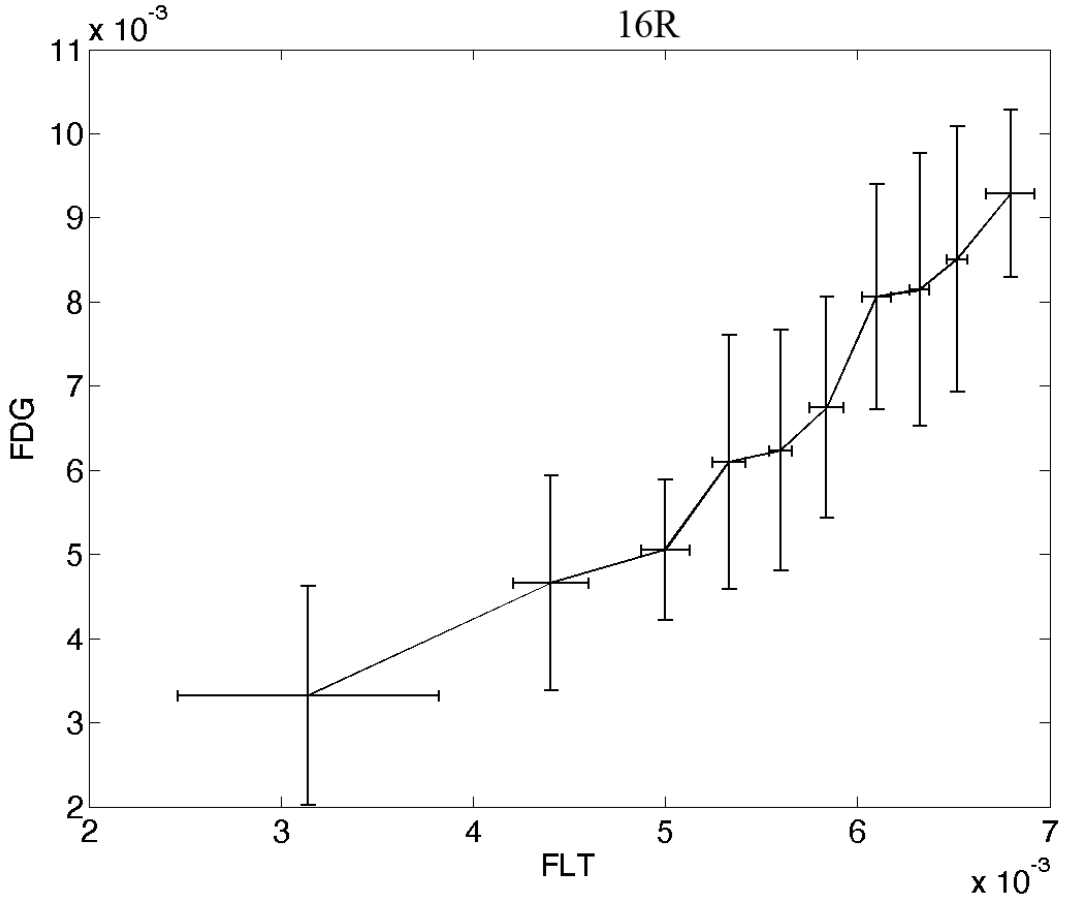

Figure 14: A binned graph showing the changes in FDG and FLT on a voxel by voxel scale for tumor 16R with a reconstructed PET resolution of .77 mm

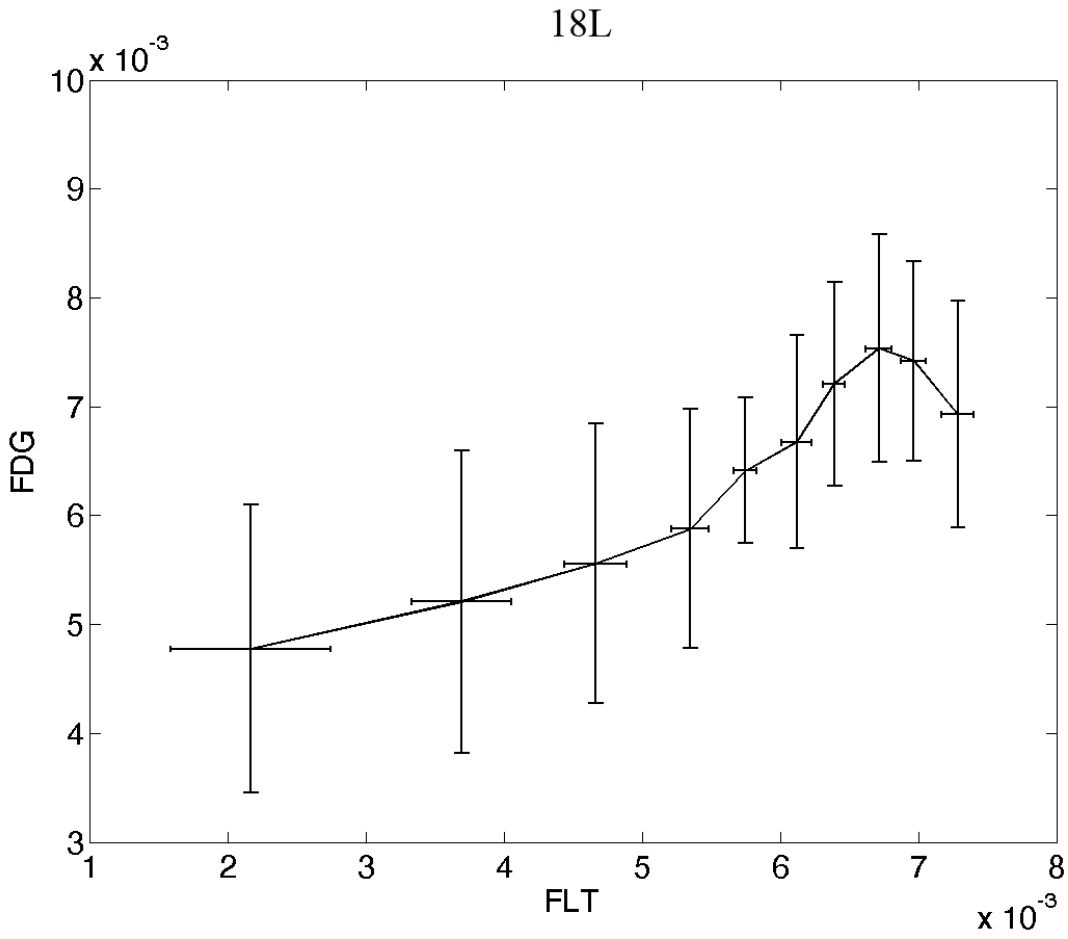

Figure 15: A binned graph showing the changes in FDG and FLT on a voxel by voxel scale for tumor 18L with a reconstructed PET resolution of .77 mm

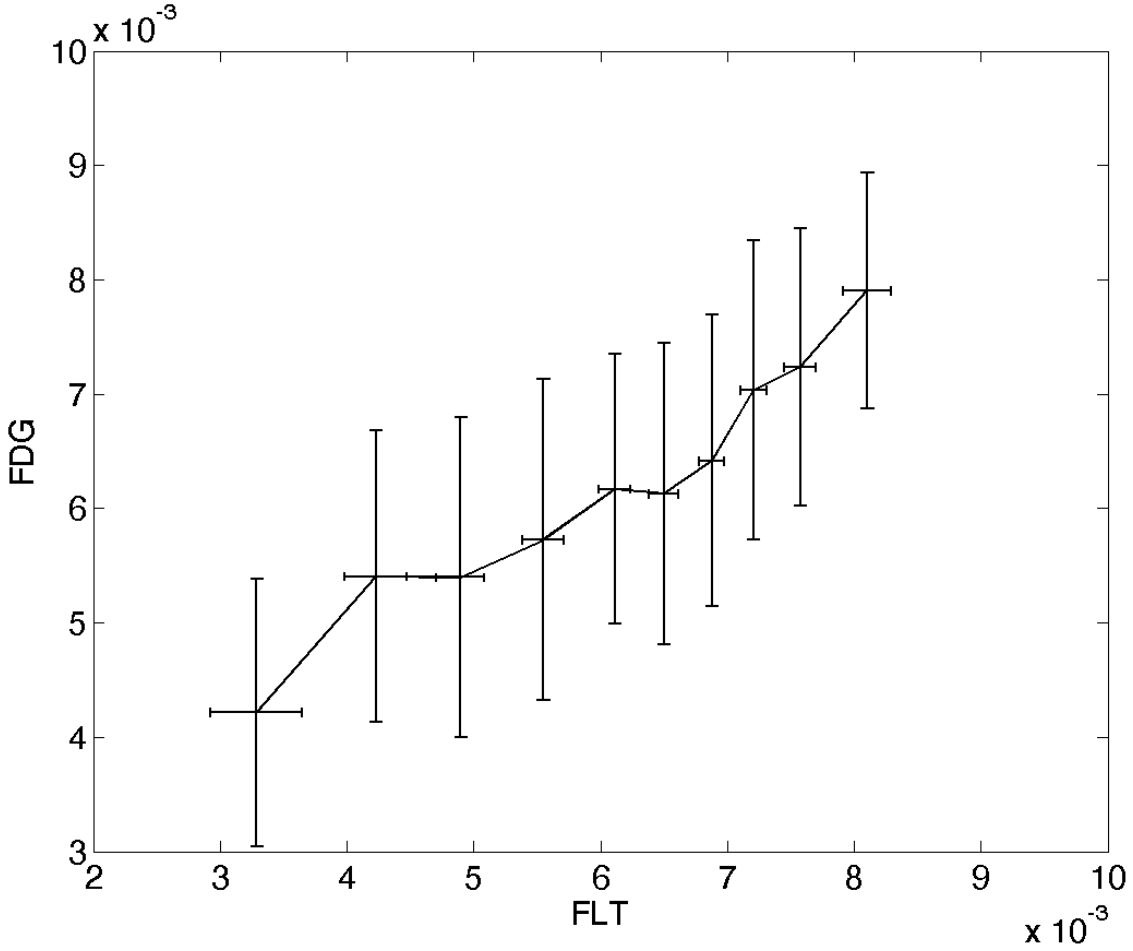

Figure 16: A binned graph showing the changes in FDG and FLT on a voxel by voxel scale for tumor 18R with a reconstructed PET resolution of .77 mm

Appendix III

Since the analysis of these images is dependant upon the image registration method used to register the FDG and FLT image sets the analysis was also performed using a Demon's deformation algorithm available in the research version of Pinnacle 9. This algorithm was chosen because of its availability in a patient-based treatment planning system as opposed to an open source image analysis environment. The analysis used the exact images as the slicer 3 analysis in chapter 4 of the dissertation as inputs to image registration. After registration, images were processed using the matlab code from the slicer 3 analysis. Binned graphs and scatterplots were generated for images at .77 mm and the 1.5 mm voxel sizes. In addition the Dice coefficient overlap analysis was also carried out for these data sets. All data analysis and image post processing was preformed in the same manner as in the Slicer 3 B-spline analysis. The following sections show the results of analyzing images registered using the pinnacle 9 Demon's deformation algorithm. Image sets of both .77 mm voxel size and the rebinned 1.5 mm voxel size were analyzed.

Scatterplots of 1.5mm voxel size images registered using Pinnacle 9 Demon's algorithm

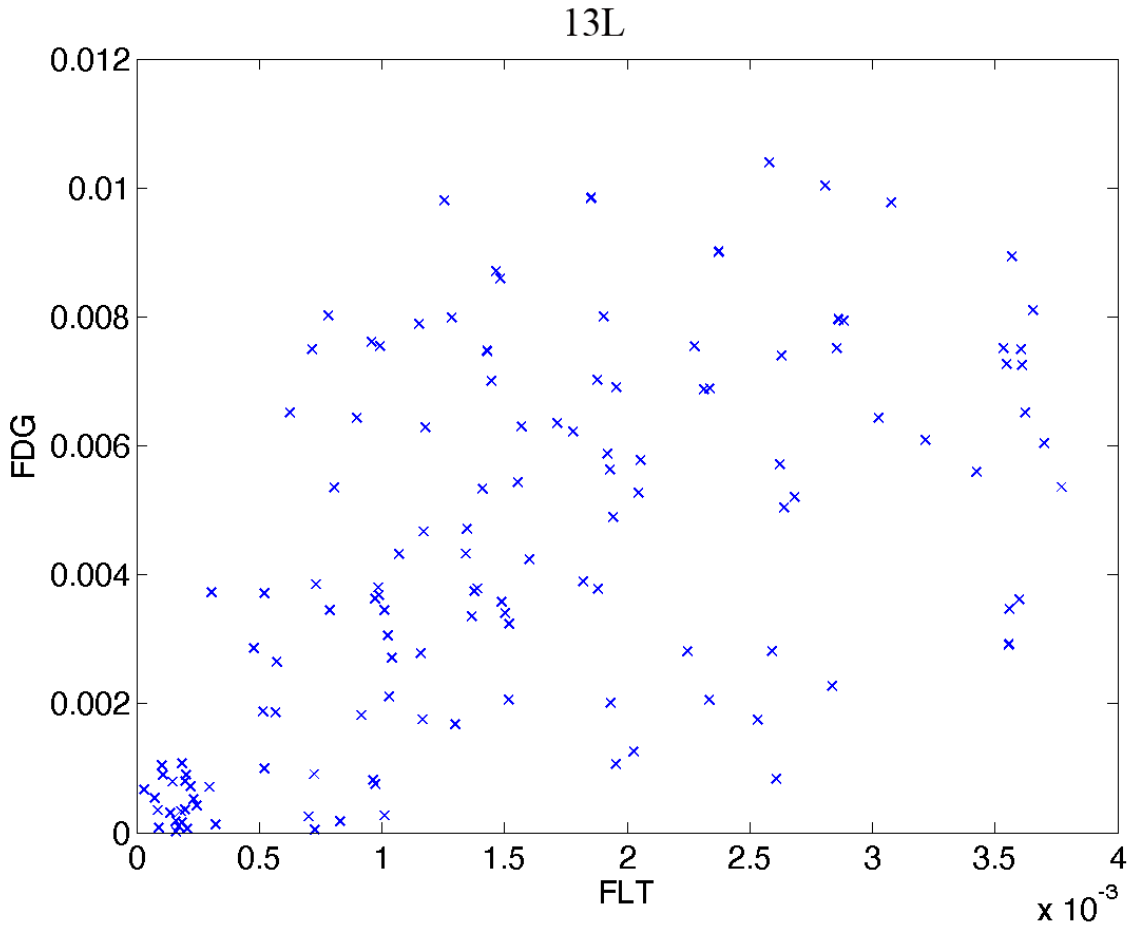

Figure 1: Scatterplot showing the changes in FLT and FDG uptake in each voxel of the PET image for the FaDu tumor 13L

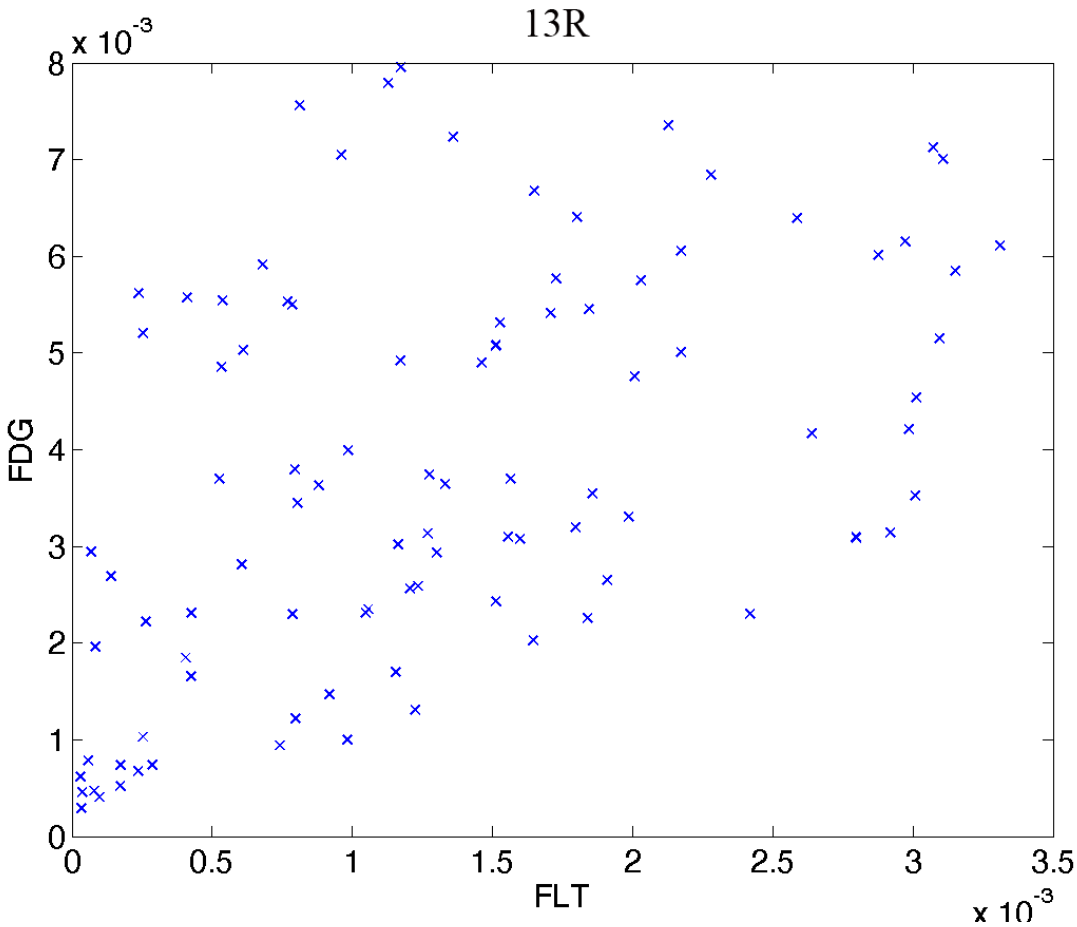

Figure 2: Scatterplot showing the changes in FLT and FDG uptake in each voxel of the PET image for the FaDu tumor 13R

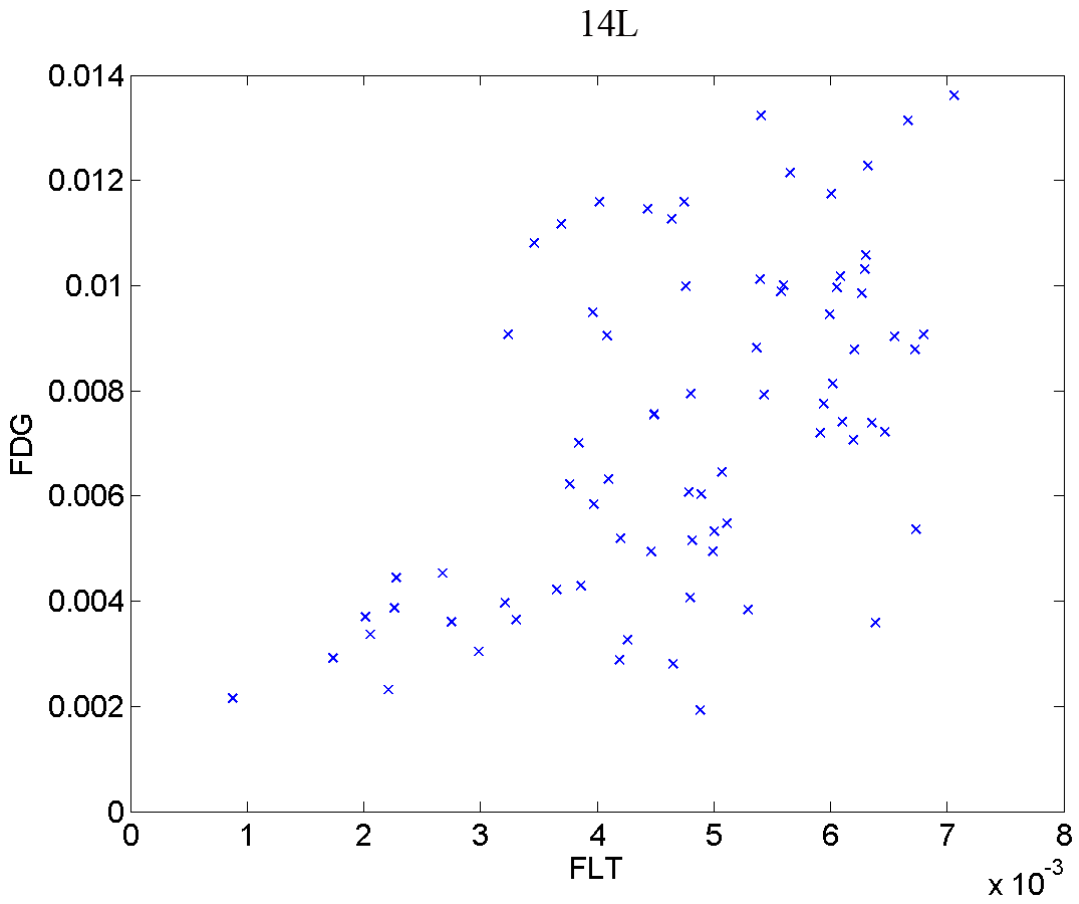

Figure 3: Scatterplot showing the changes in FLT and FDG uptake in each voxel of the PET image for the FaDu tumor 14L

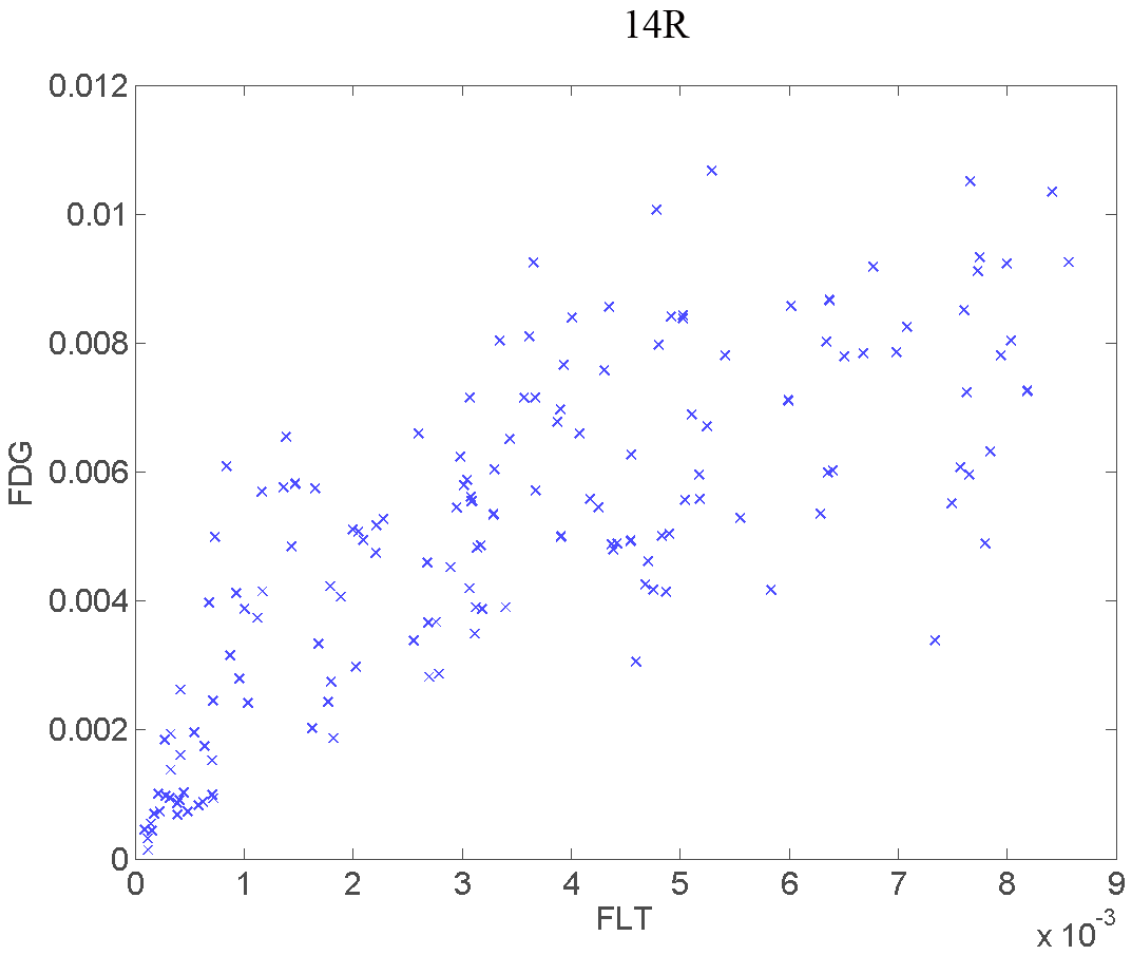

Figure 4: Scatterplot showing the changes in FLT and FDG uptake in each voxel of the PET image for the FaDu tumor 14R

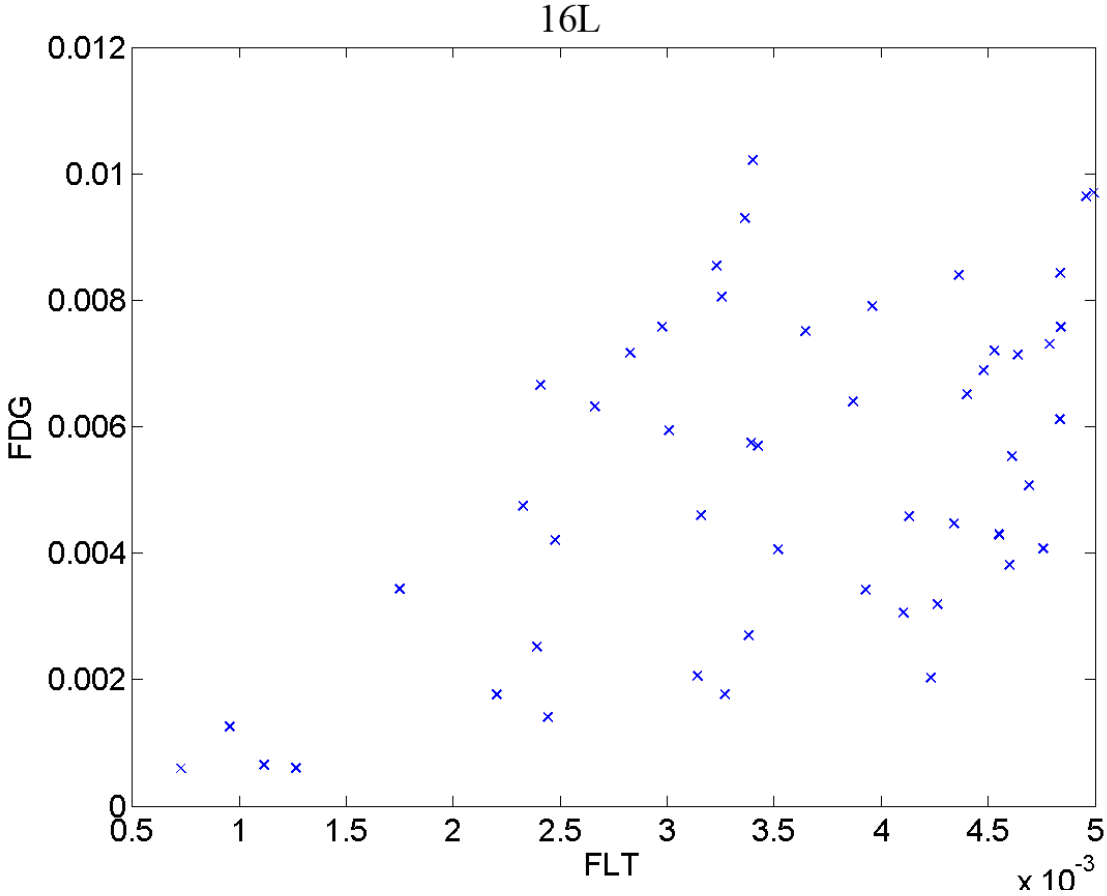

Figure 5: Scatterplot showing the changes in FLT and FDG uptake in each voxel of the PET image for the SQ20B tumor 16L

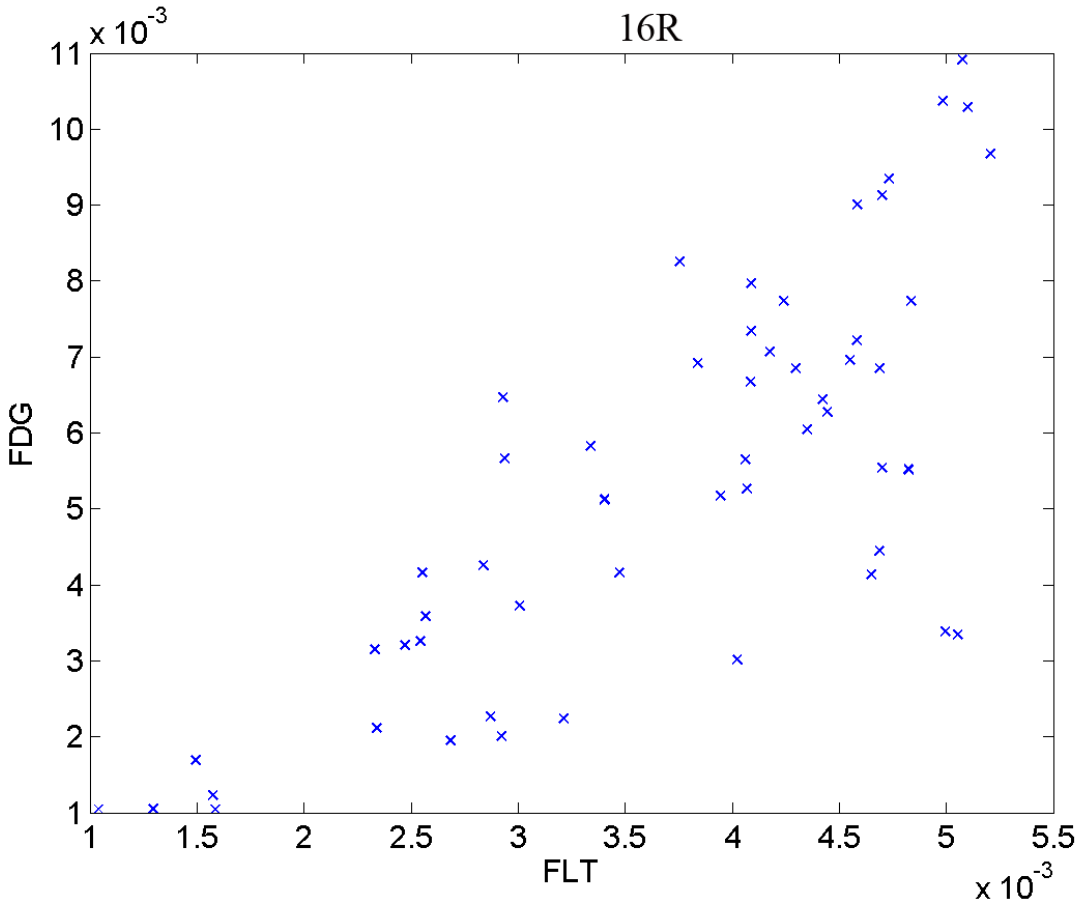

Figure 6: Scatterplot showing the changes in FLT and FDG uptake in each voxel of the PET image for the SQ20B tumor 16R

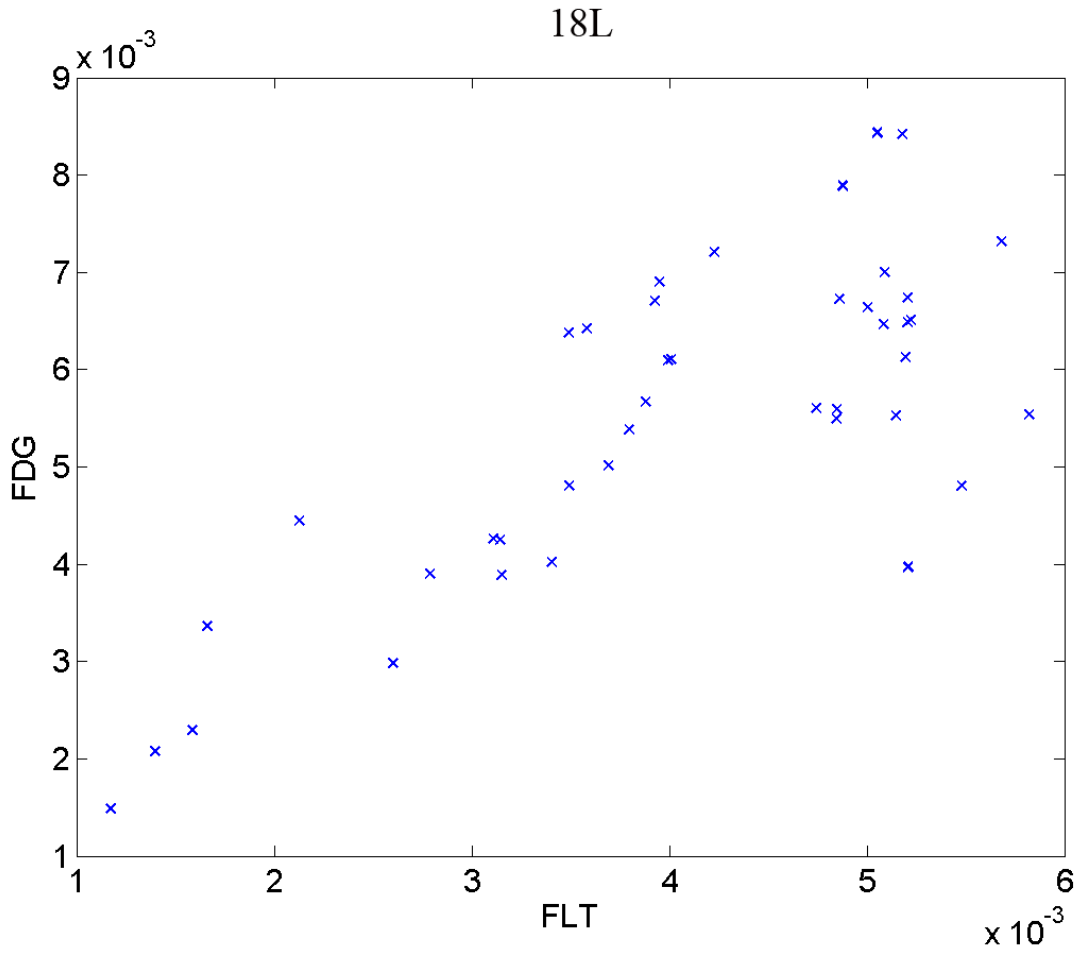

Figure 7: Scatterplot showing the changes in FLT and FDG uptake in each voxel of the PET image for the SQ20B tumor 18L

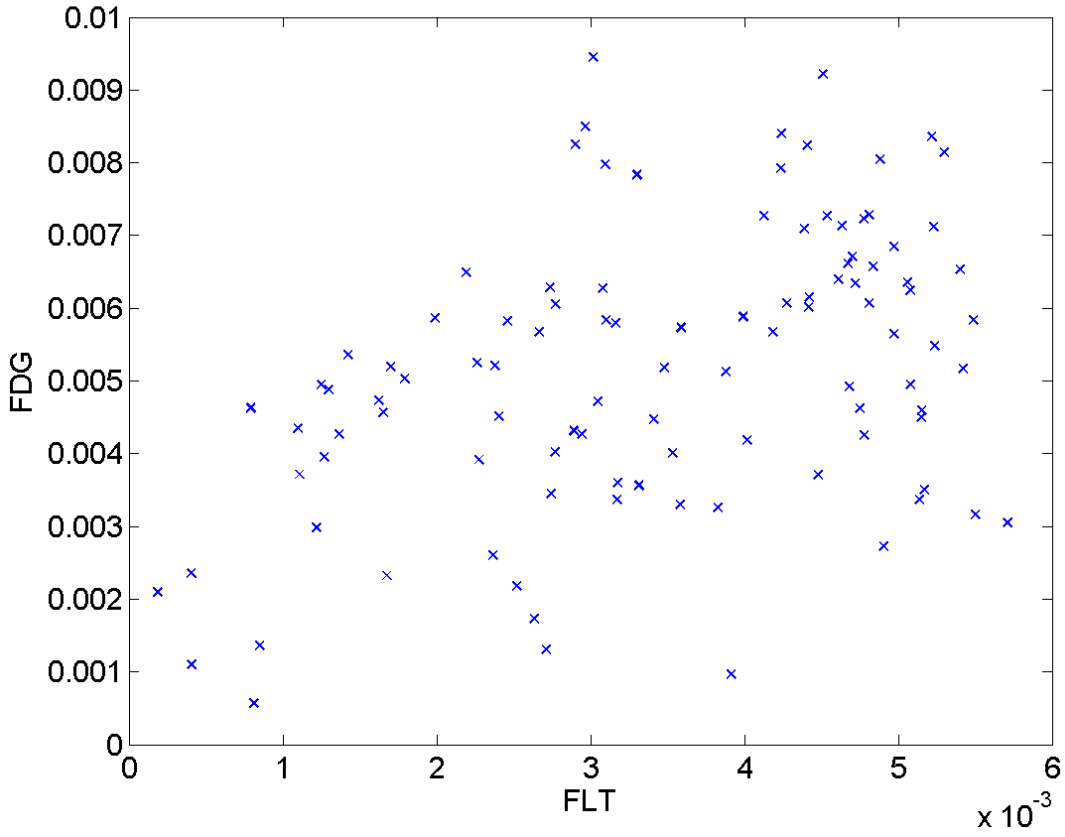

Figure 8: Scatterplot showing the changes in FLT and FDG uptake in each voxel of the PET image for the SQ20B tumor 18R

Binned graphs of 1.5mm voxel size images registered using Pinnacle 9 Demon's algorithm

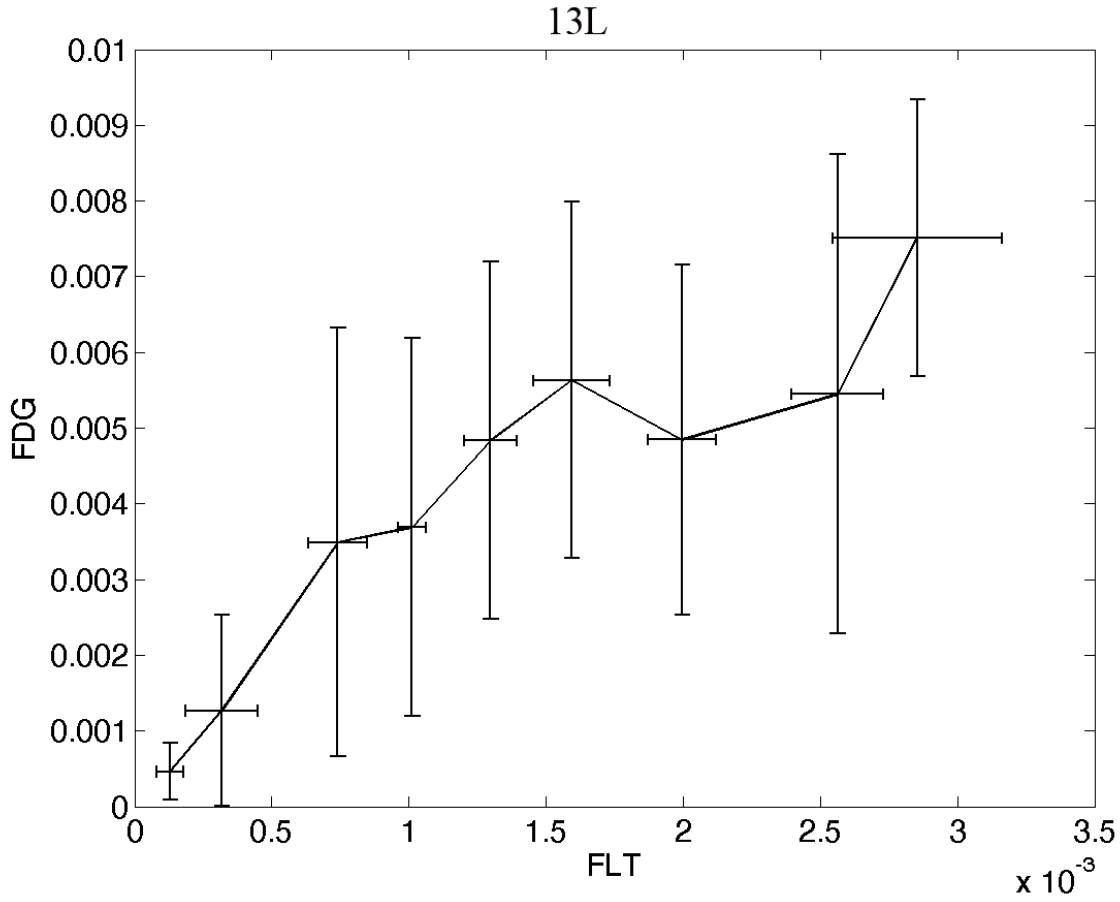

Figure 9: Binned graph showing the changes in FLT and FDG uptake in each voxel of the PET image for the FaDu tumor 13L

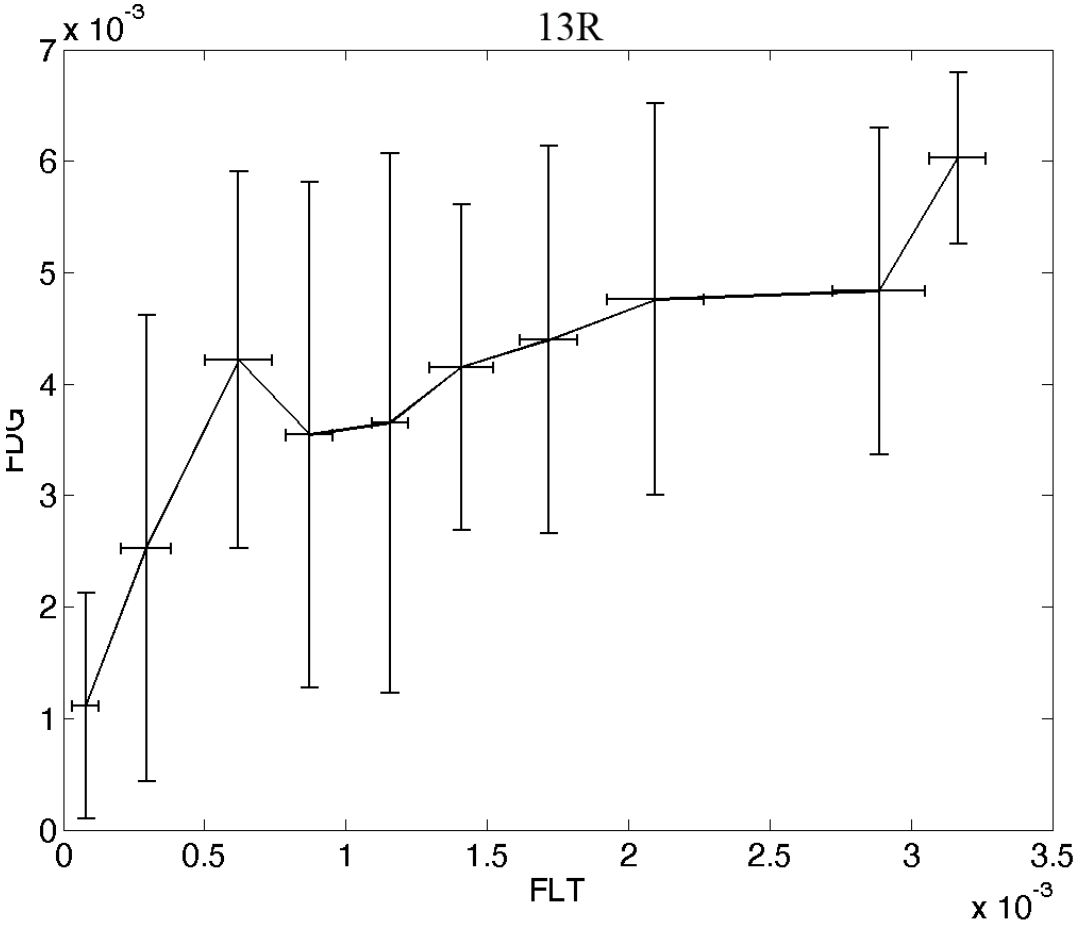

Figure 10: Binned graph showing the changes in FLT and FDG uptake in each voxel of the PET image for the FaDu tumor 13R

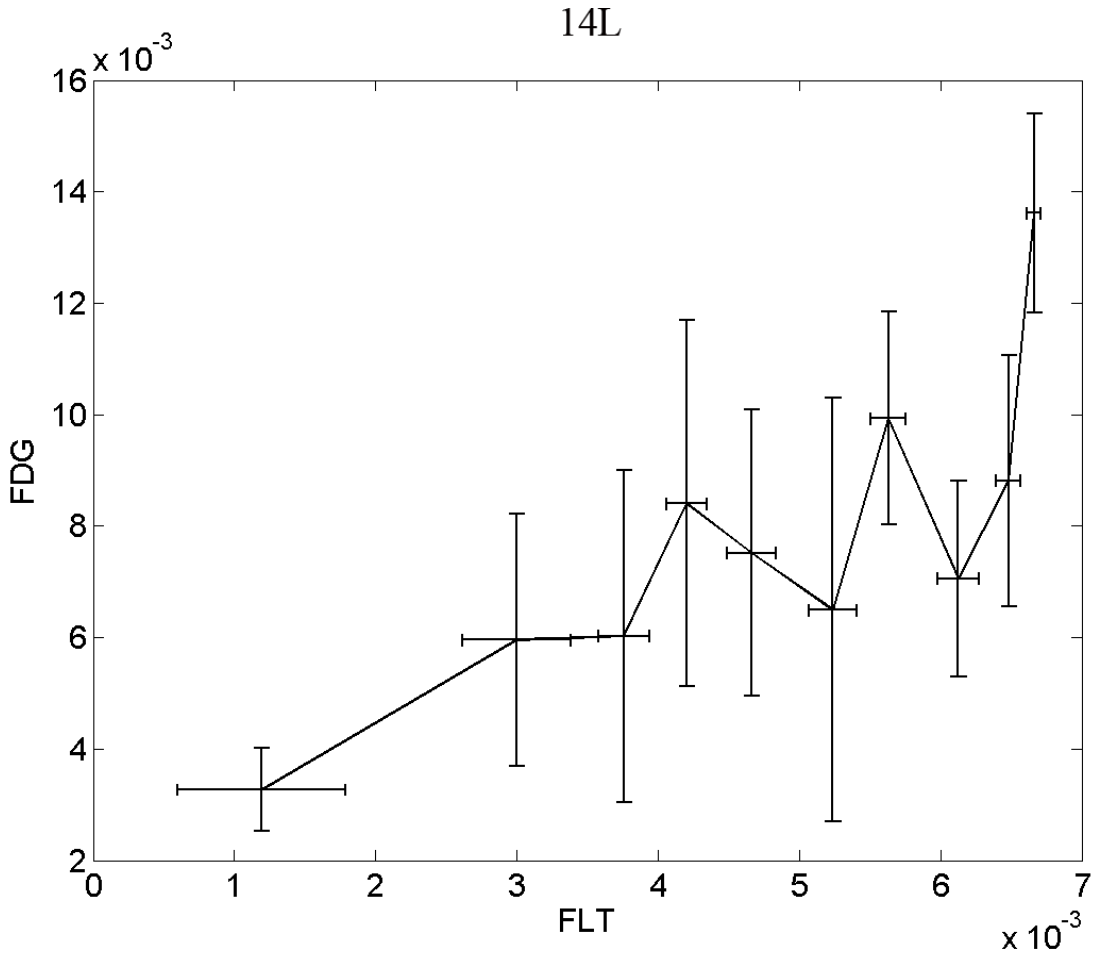

Figure 11: Binned graph showing the changes in FLT and FDG uptake in each voxel of the PET image for the FaDu tumor 14L

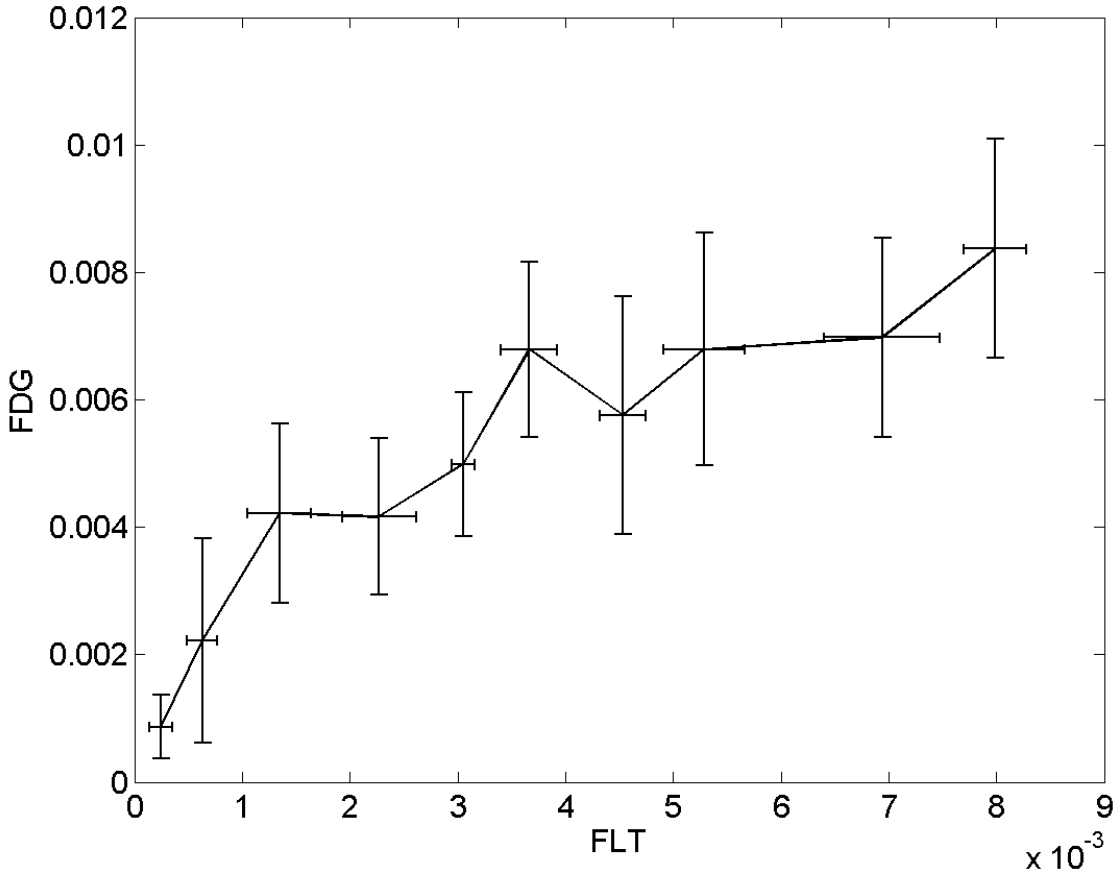

Figure 12: Binned graph showing the changes in FLT and FDG uptake in each voxel of the PET image for the FaDu tumor 14R

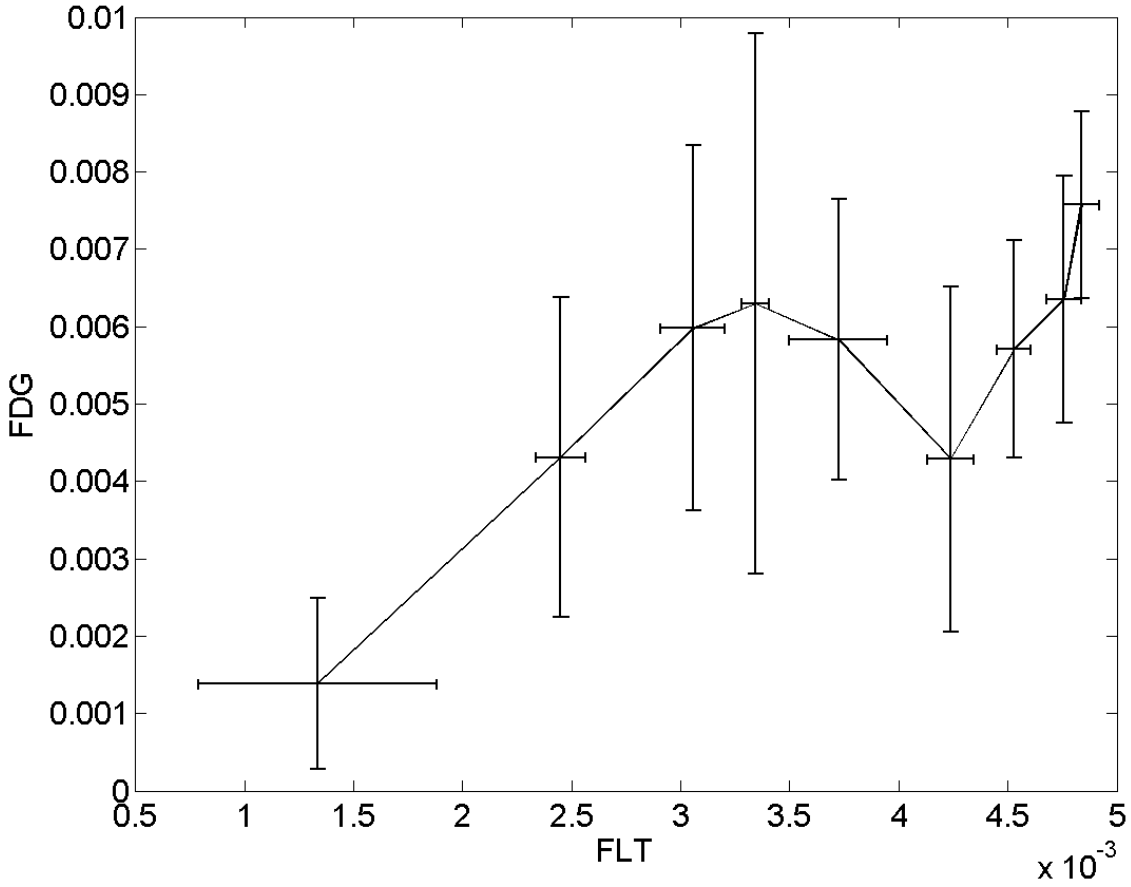

Figure 13: Binned graph showing the changes in FLT and FDG uptake in each voxel of the PET image for the SQ20B tumor 16L

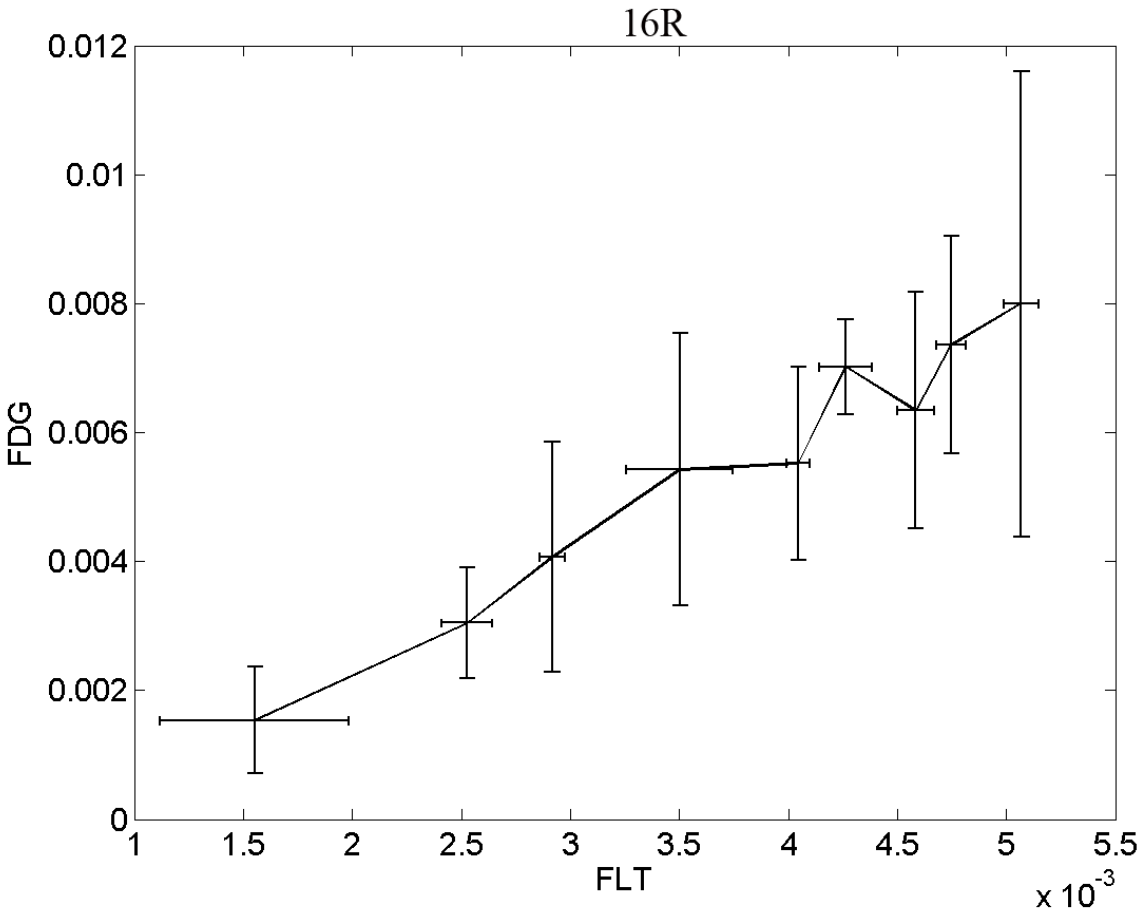

Figure 14: Binned graph showing the changes in FLT and FDG uptake in each voxel of the PET image for the SQ20B tumor 16R

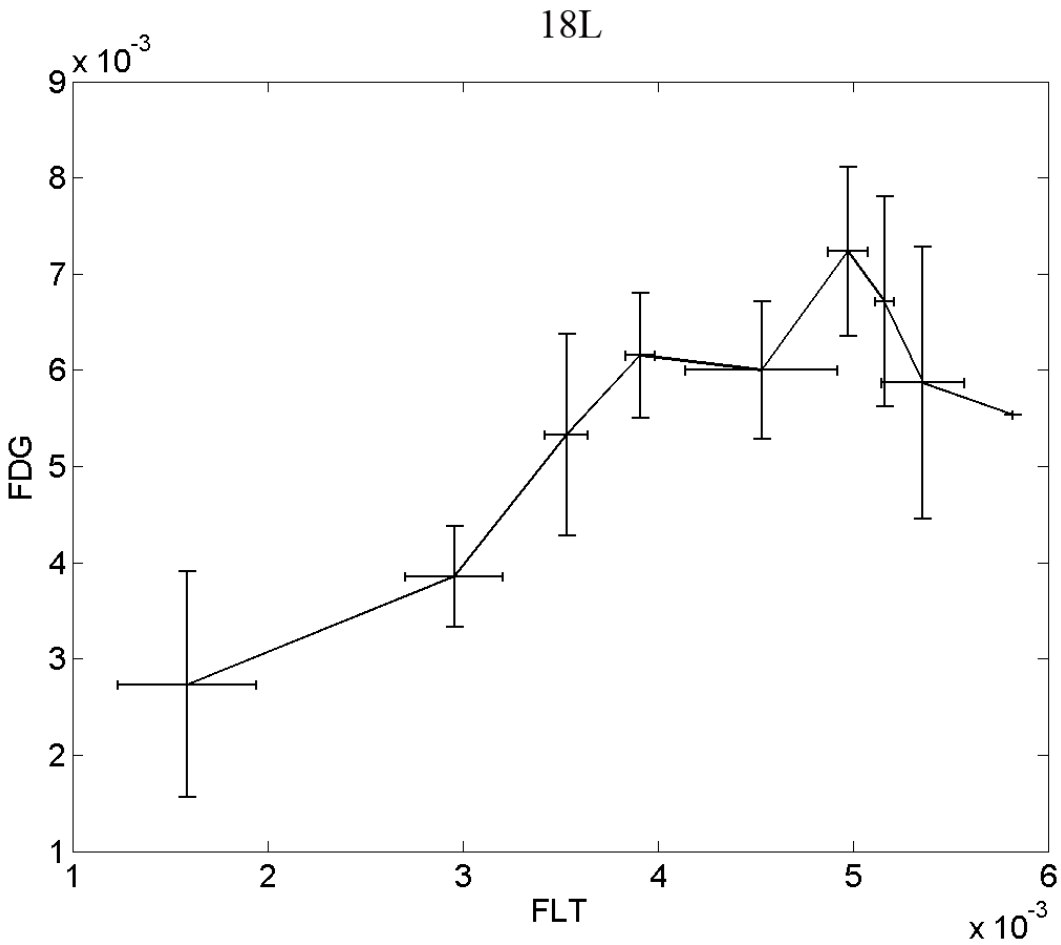

Figure 15: Binned graph showing the changes in FLT and FDG uptake in each voxel of the PET image for the SQ20B tumor 18L

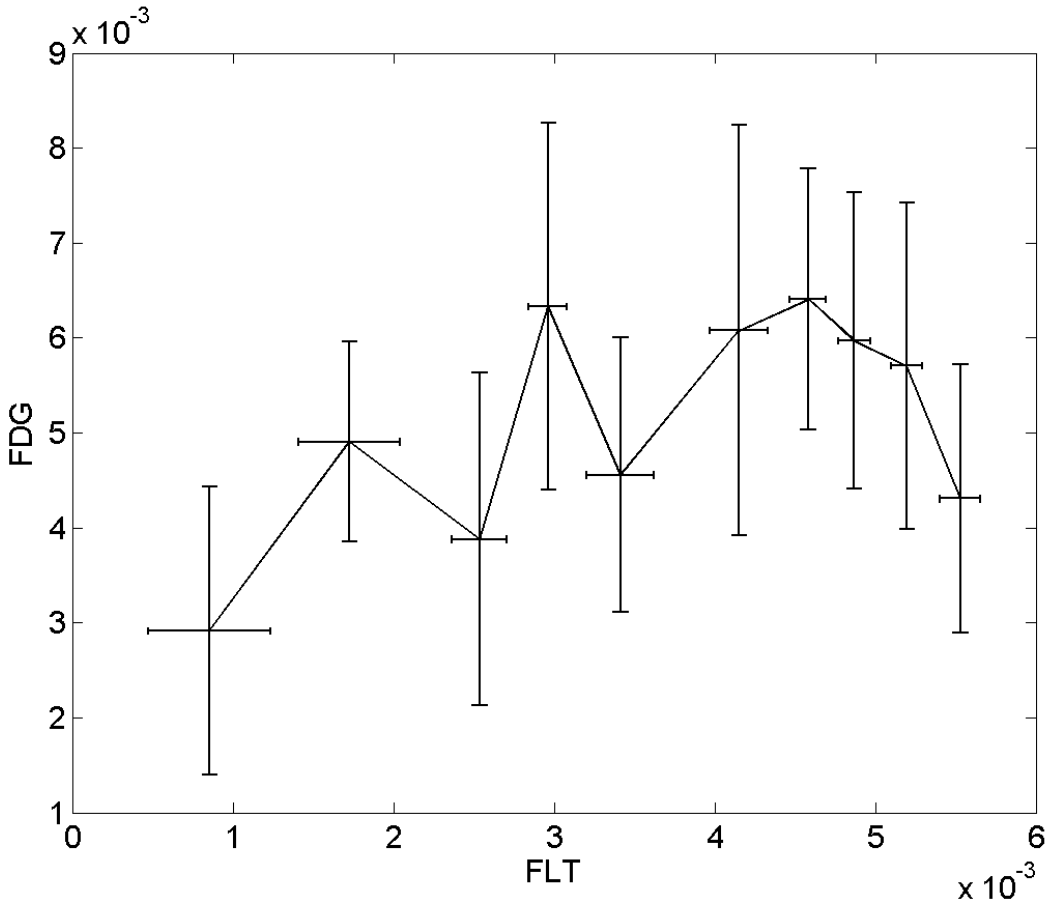

Figure 16: Binned graph showing the changes in FLT and FDG uptake in each voxel of the PET image for the SQ20B tumor 18R

Scatterplot of .77 voxel size images registered using Pinnacle 9 Demon's algorithm

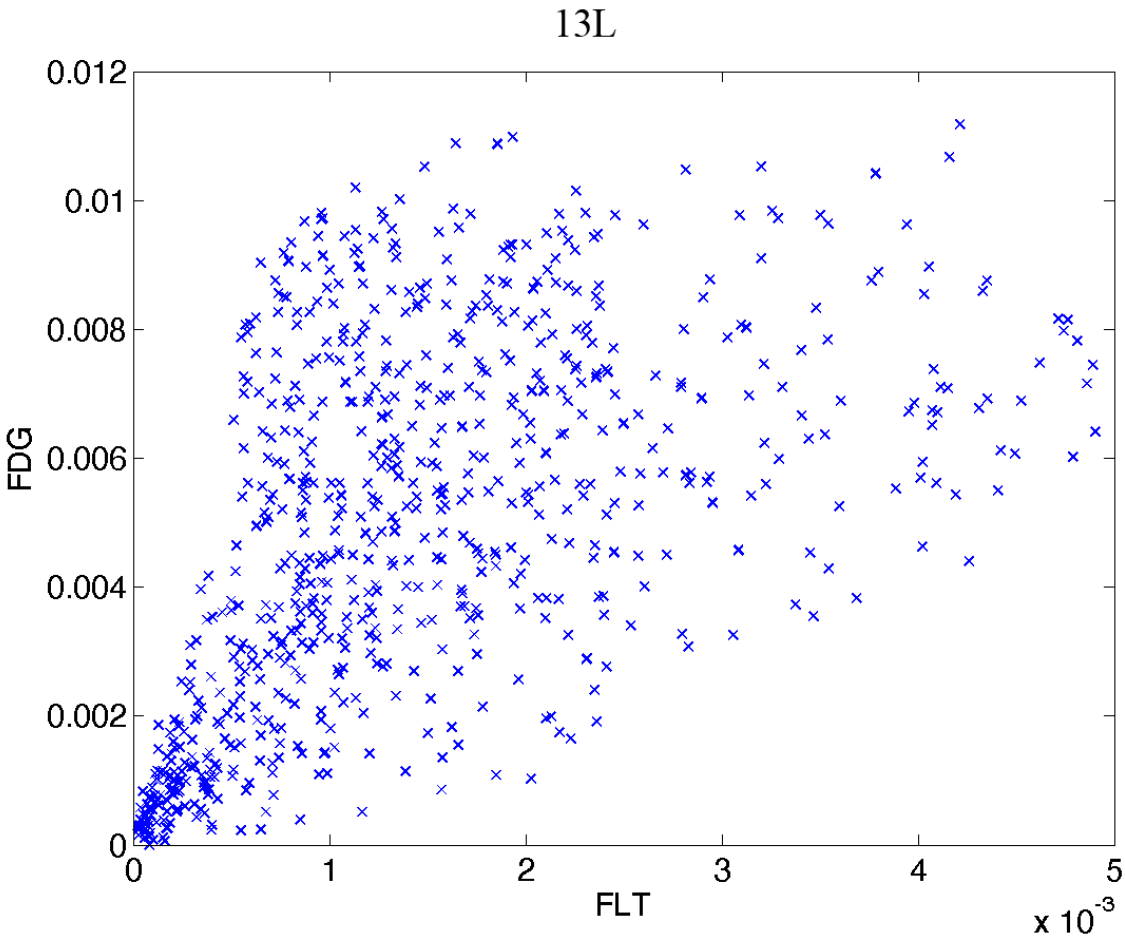

Figure 16: Scatterplot showing the changes in FLT and FDG uptake in each voxel of the PET image for the FaDu tumor 13L with a reconstructed voxel size of .77 mm

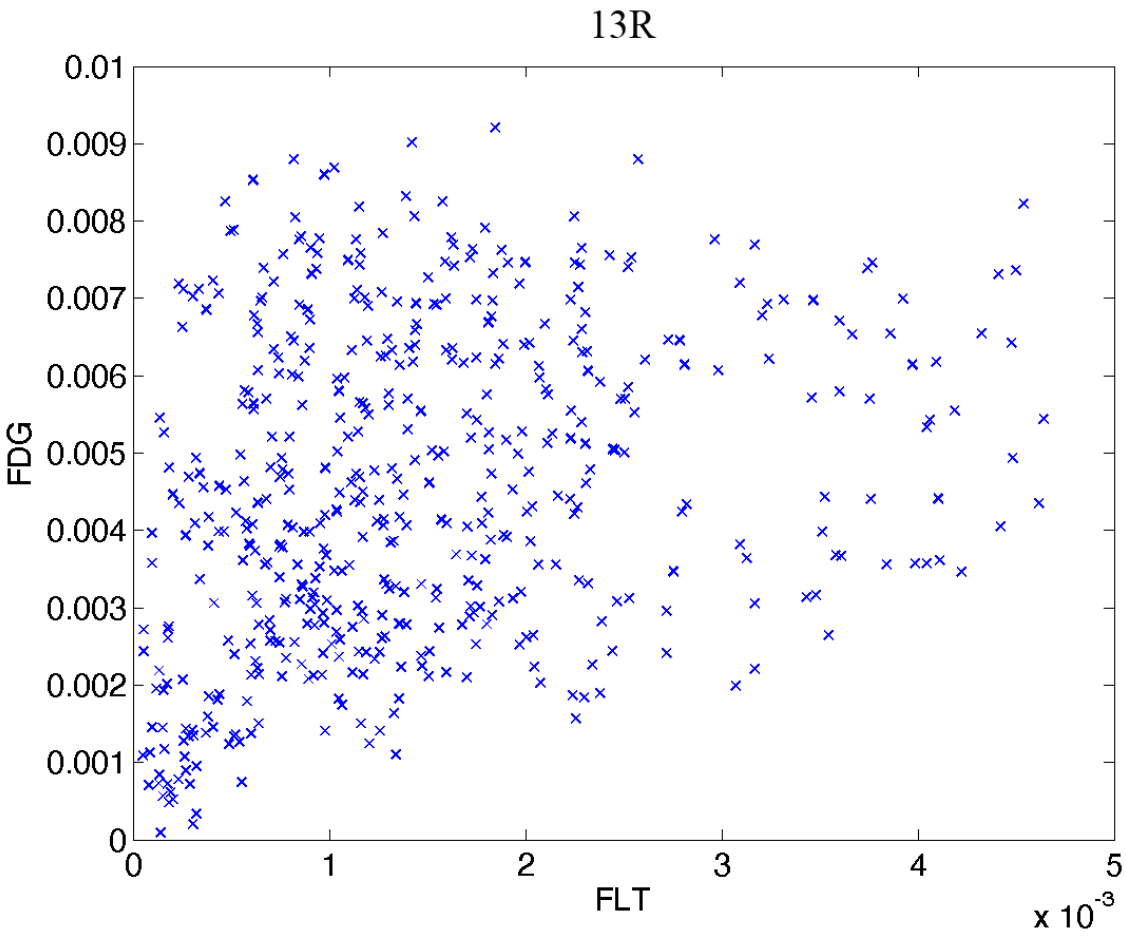

Figure 17: Scatterplot showing the changes in FLT and FDG uptake in each voxel of the PET image for the FaDu tumor 13R with a reconstructed voxel size of .77 mm

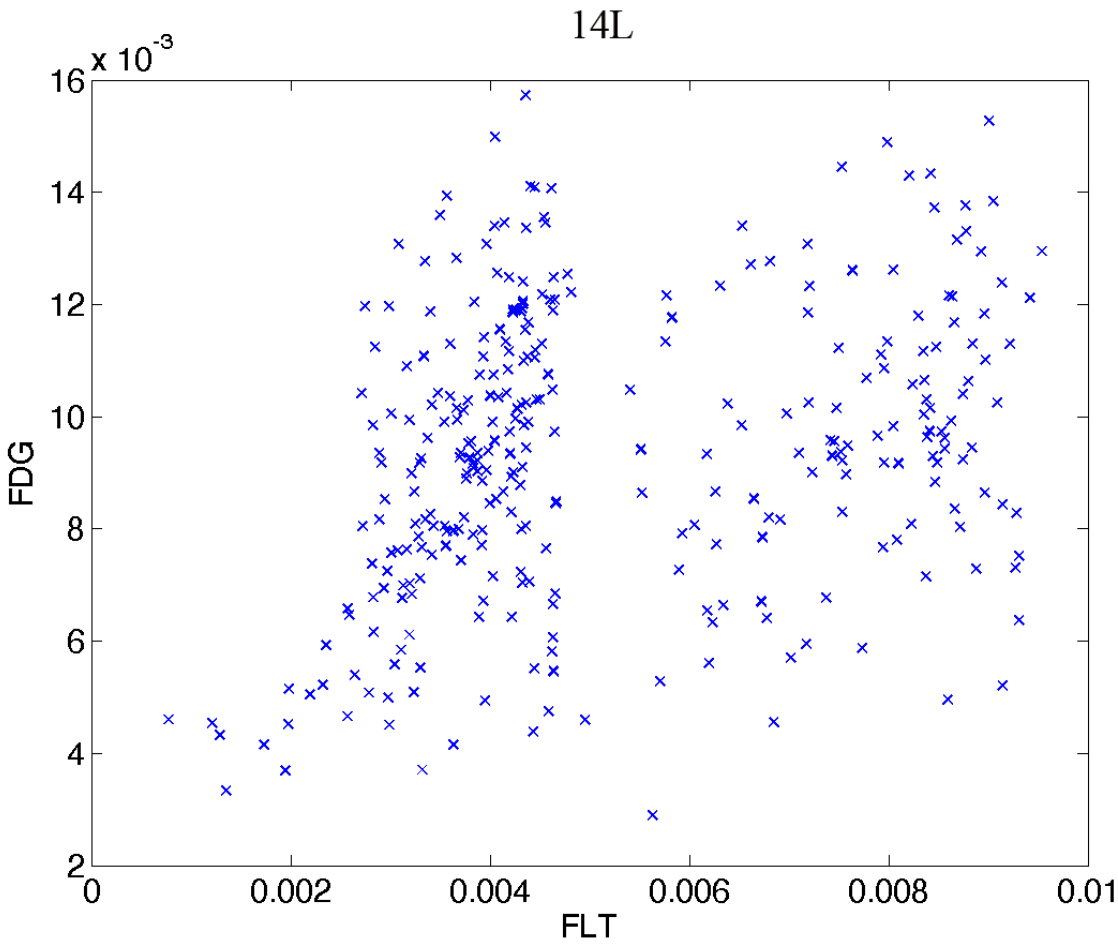

Figure 18: Scatterplot showing the changes in FLT and FDG uptake in each voxel of the PET image for the FaDu tumor 14L with a reconstructed voxel size of .77 mm

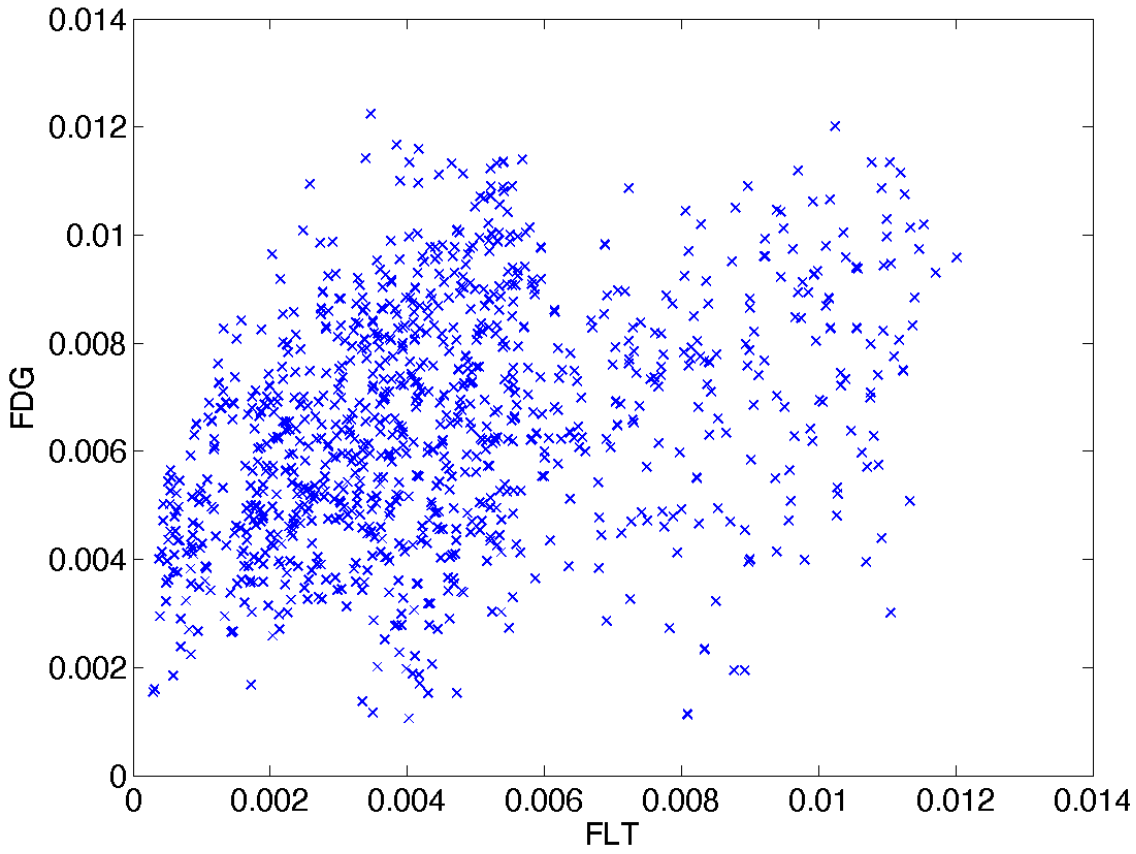

Figure 19: Scatterplot showing the changes in FLT and FDG uptake in each voxel of the PET image for the FaDu tumor 14R with a reconstructed voxel size of .77 mm

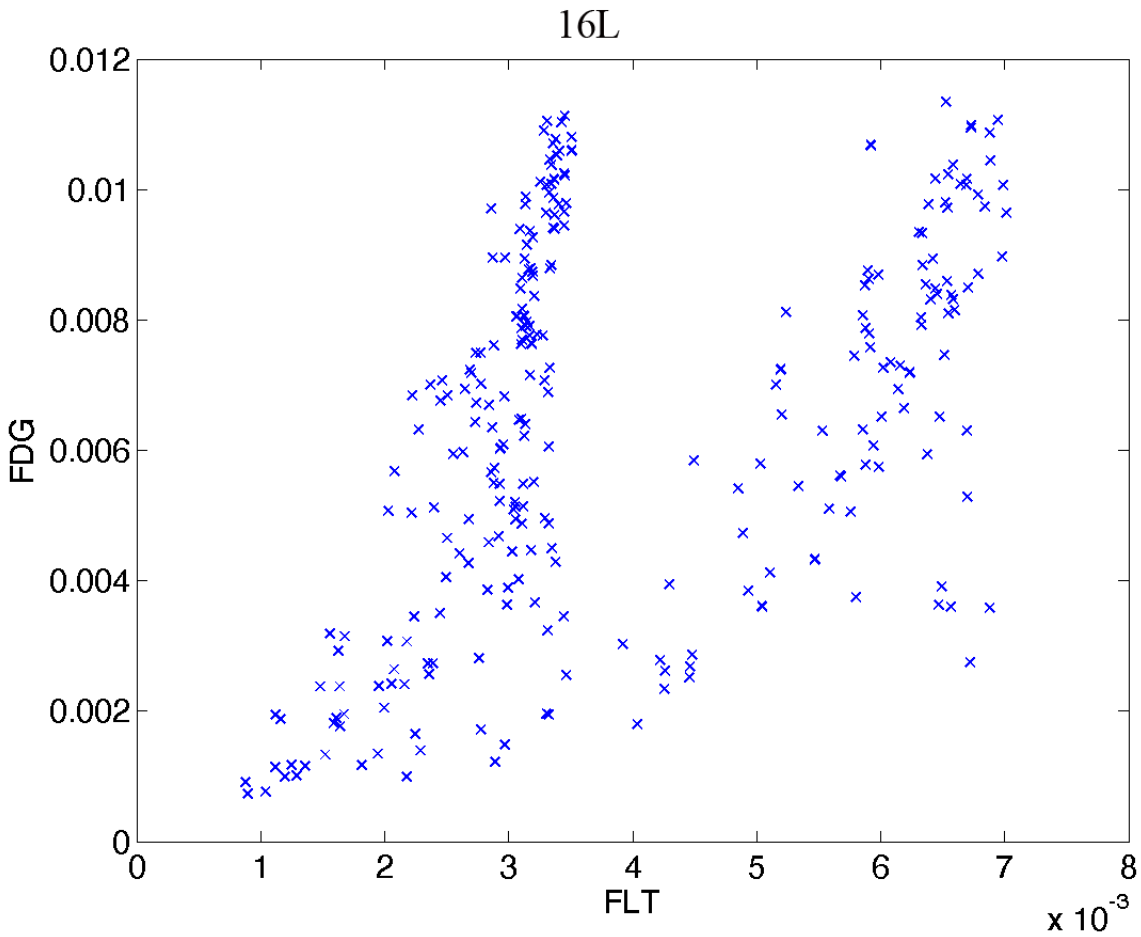

Figure 20: Scatterplot showing the changes in FLT and FDG uptake in each voxel of the PET image for the SQ20B tumor 16L with a reconstructed voxel size of .77 mm

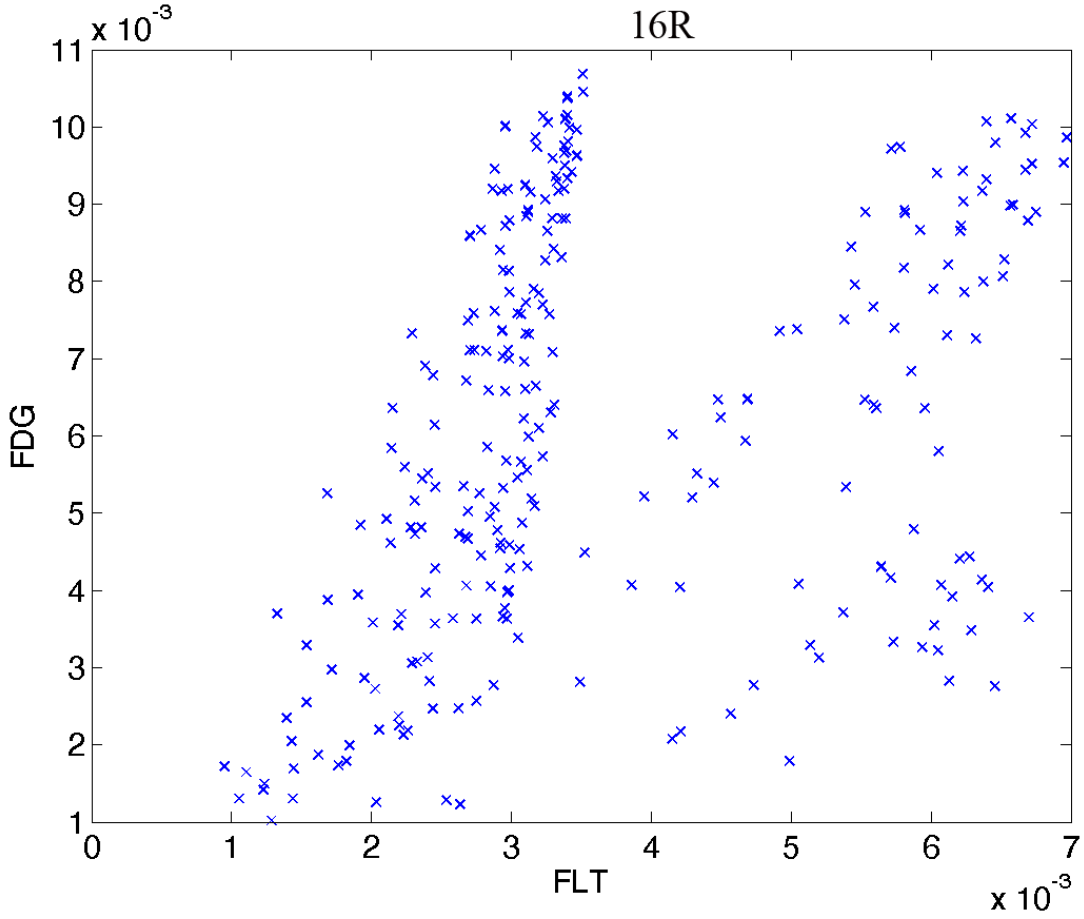

Figure 21: Scatterplot showing the changes in FLT and FDG uptake in each voxel of the PET image for the SQ20B tumor 16R with a reconstructed voxel size of .77 mm

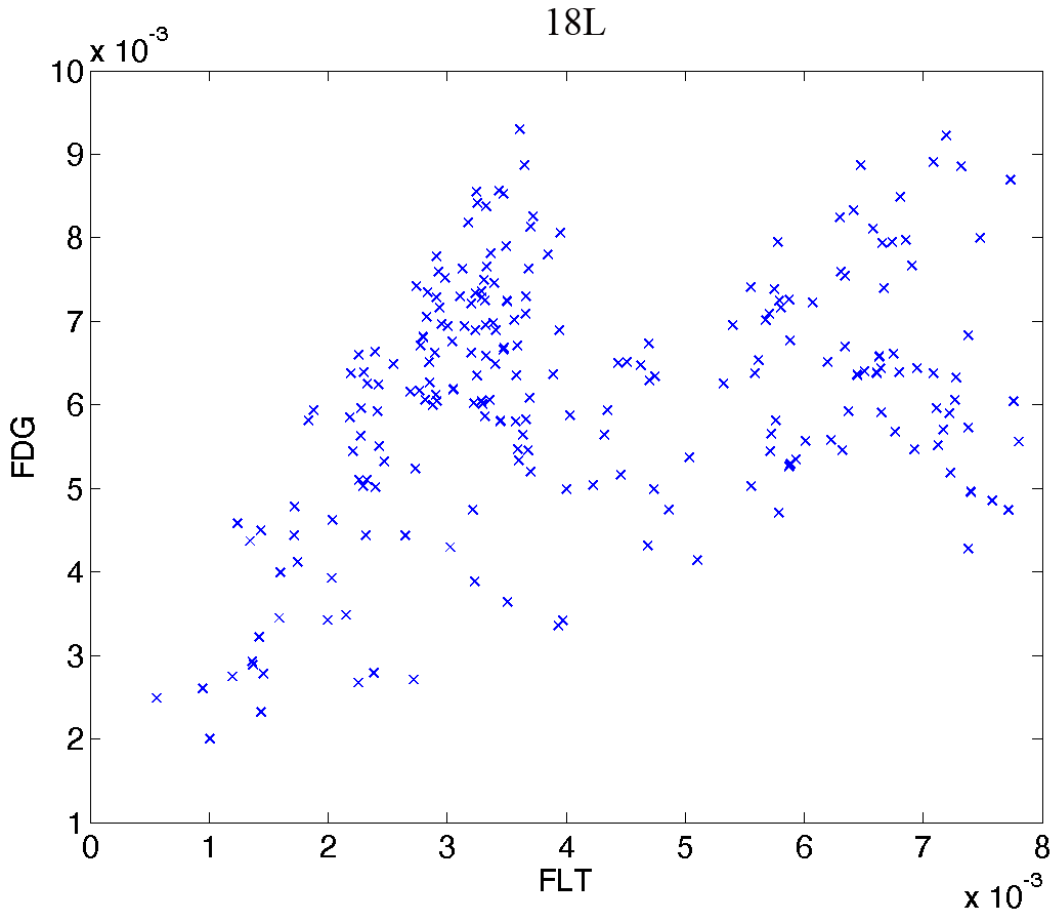

Figure 22: Scatterplot showing the changes in FLT and FDG uptake in each voxel of the PET image for the SQ20B tumor 18L with a reconstructed voxel size of .77 mm

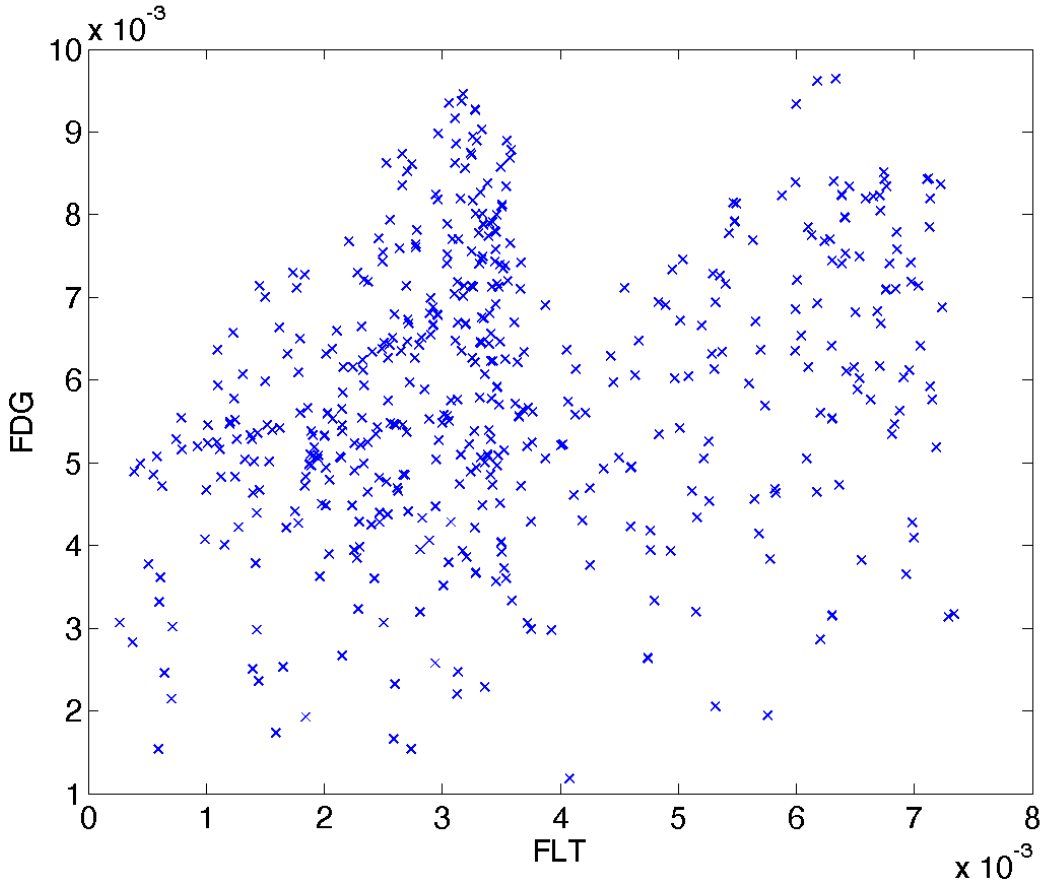

Figure 23: Scatterplot showing the changes in FLT and FDG uptake in each voxel of the PET image for the SQ20B tumor 18R with a reconstructed voxel size of .77 mm

Binned graphs of .77 voxel size images registered using Pinnacle 9 Demon's algorithm

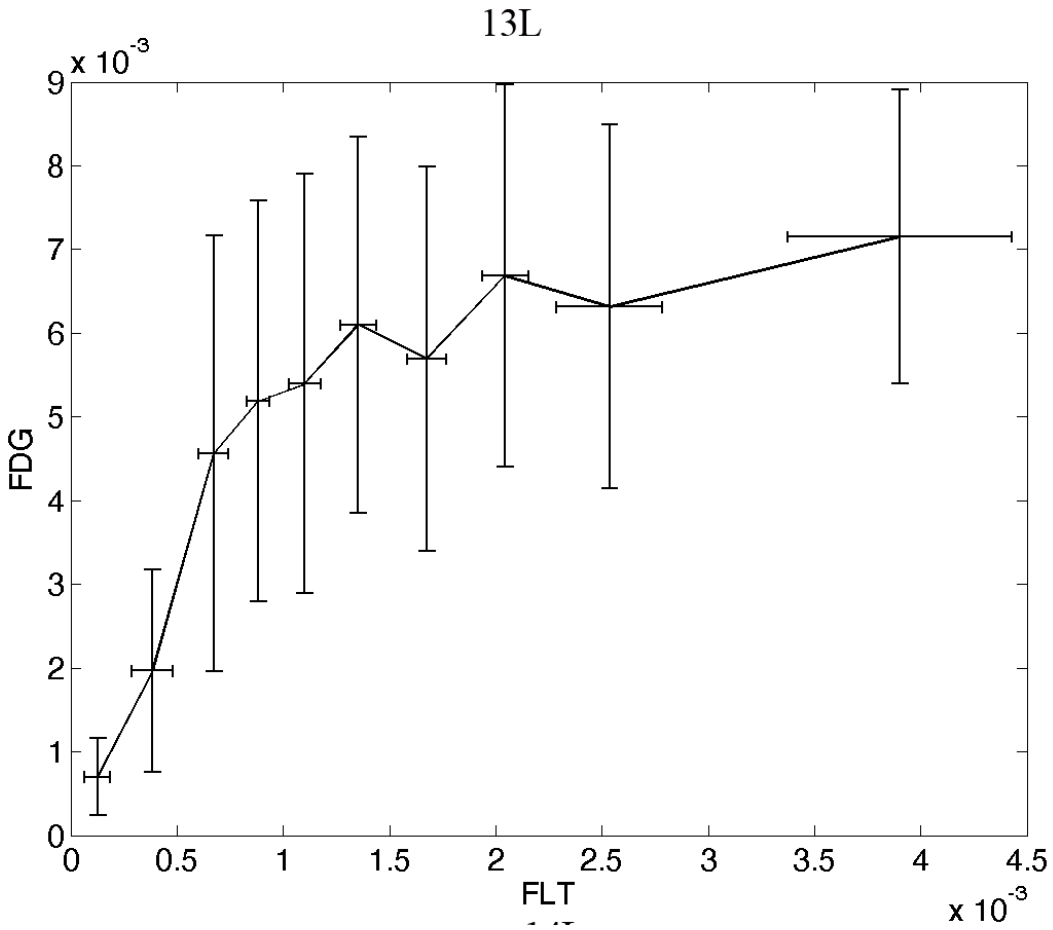

Figure 24: Binned graph showing the changes in FLT and FDG uptake in each voxel of the PET image for the FaDu tumor 13L with a reconstructed voxel size of .77 mm

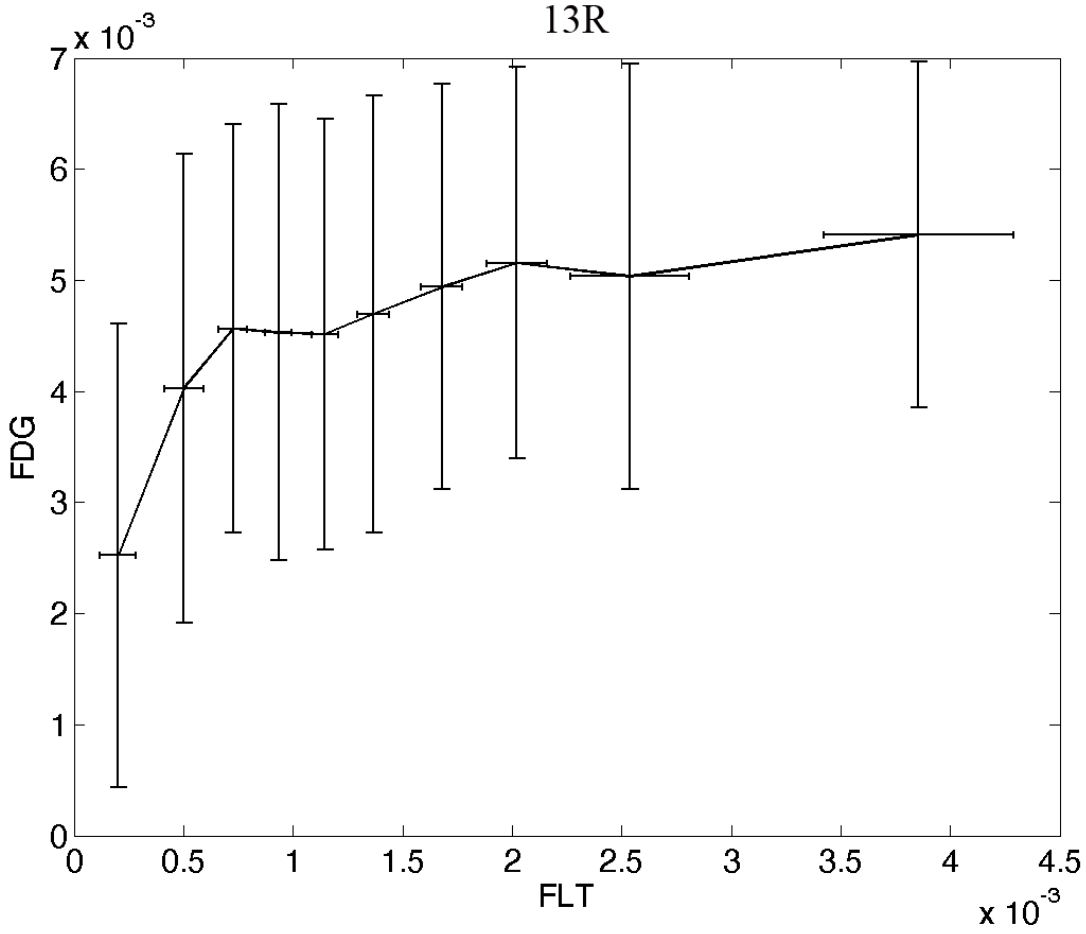

Figure 25: Binned graph showing the changes in FLT and FDG uptake in each voxel of the PET image for the FaDu tumor 13R with a reconstructed voxel size of .77 mm

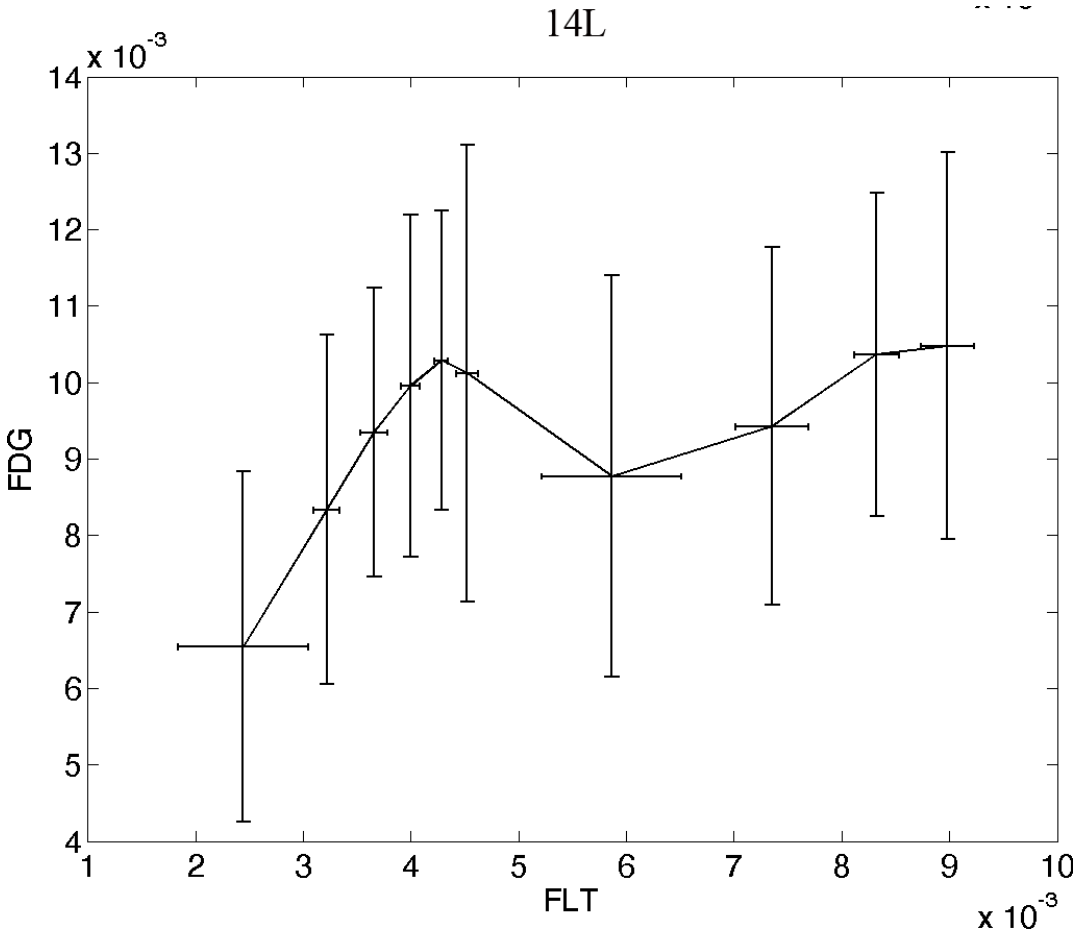

Figure 26: Binned graph showing the changes in FLT and FDG uptake in each voxel of the PET image for the FaDu tumor 14L with a reconstructed voxel size of .77 mm

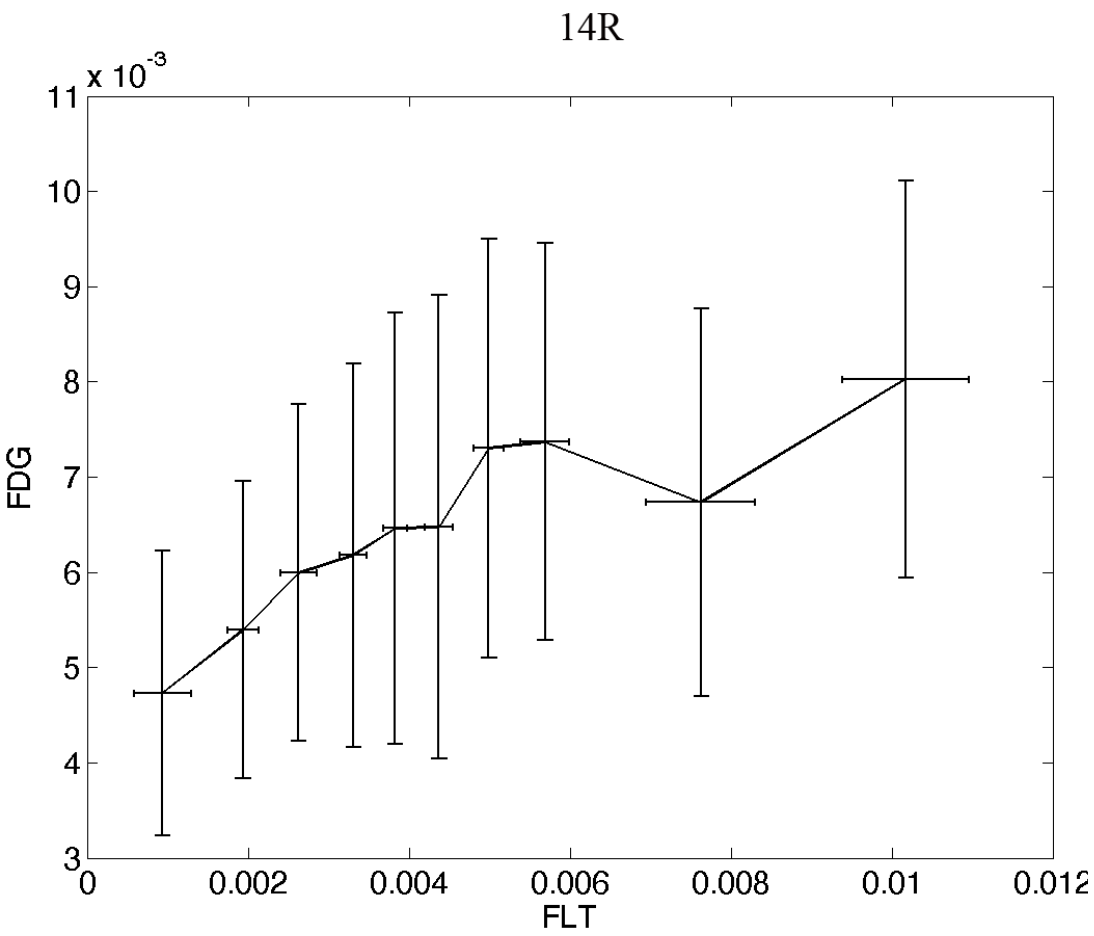

Figure 27: Binned graph showing the changes in FLT and FDG uptake in each voxel of the PET image for the FaDu tumor 14R with a reconstructed voxel size of .77 mm

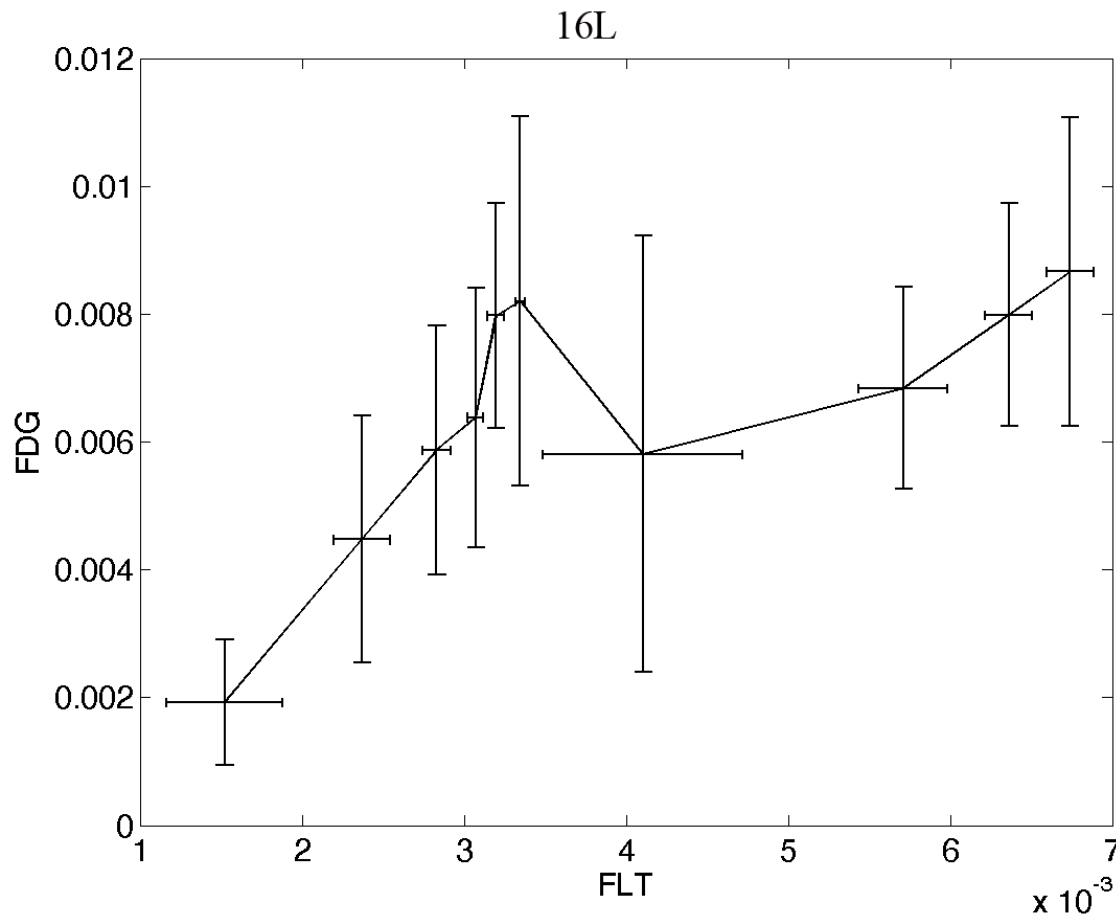

Figure 28: Binned graph showing the changes in FLT and FDG uptake in each voxel of the PET image for the SQ20B tumor 16L with a reconstructed voxel size of .77 mm

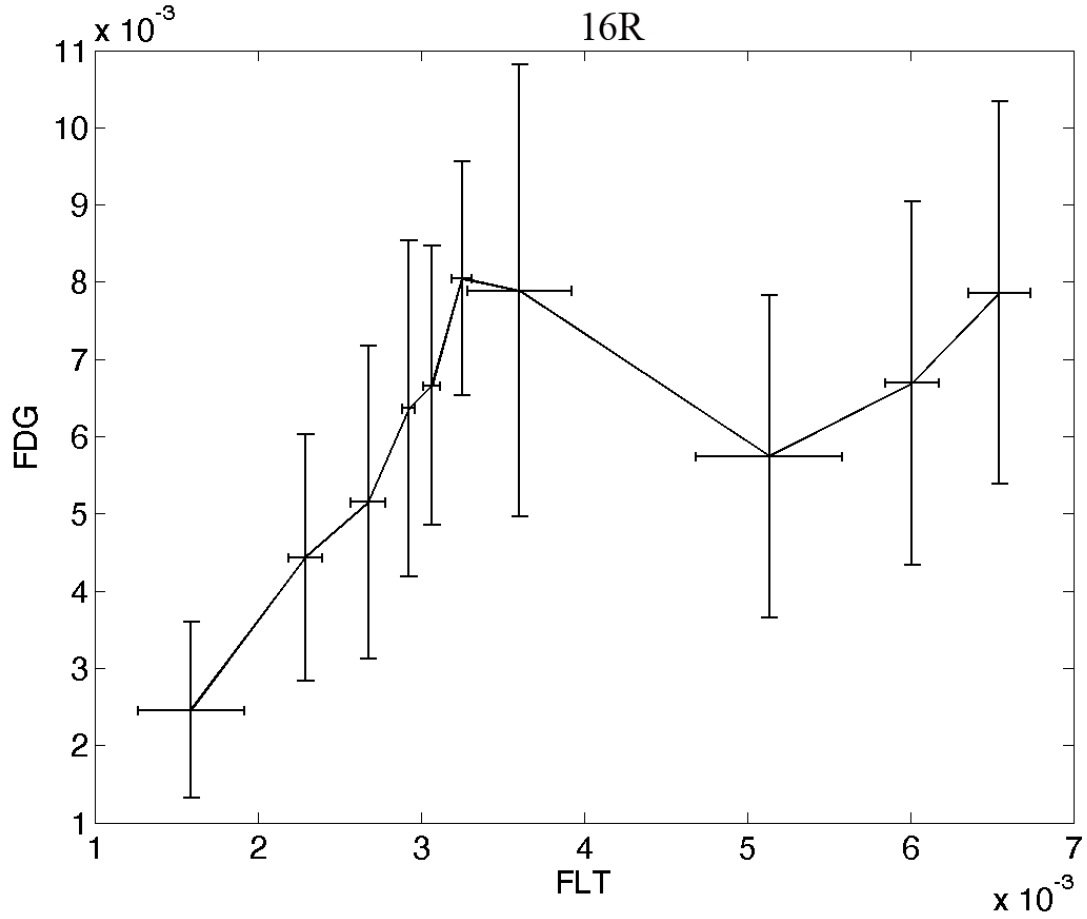

Figure 29: Binned graph showing the changes in FLT and FDG uptake in each voxel of the PET image for the SQ20B tumor 16R with a reconstructed voxel size of .77 mm

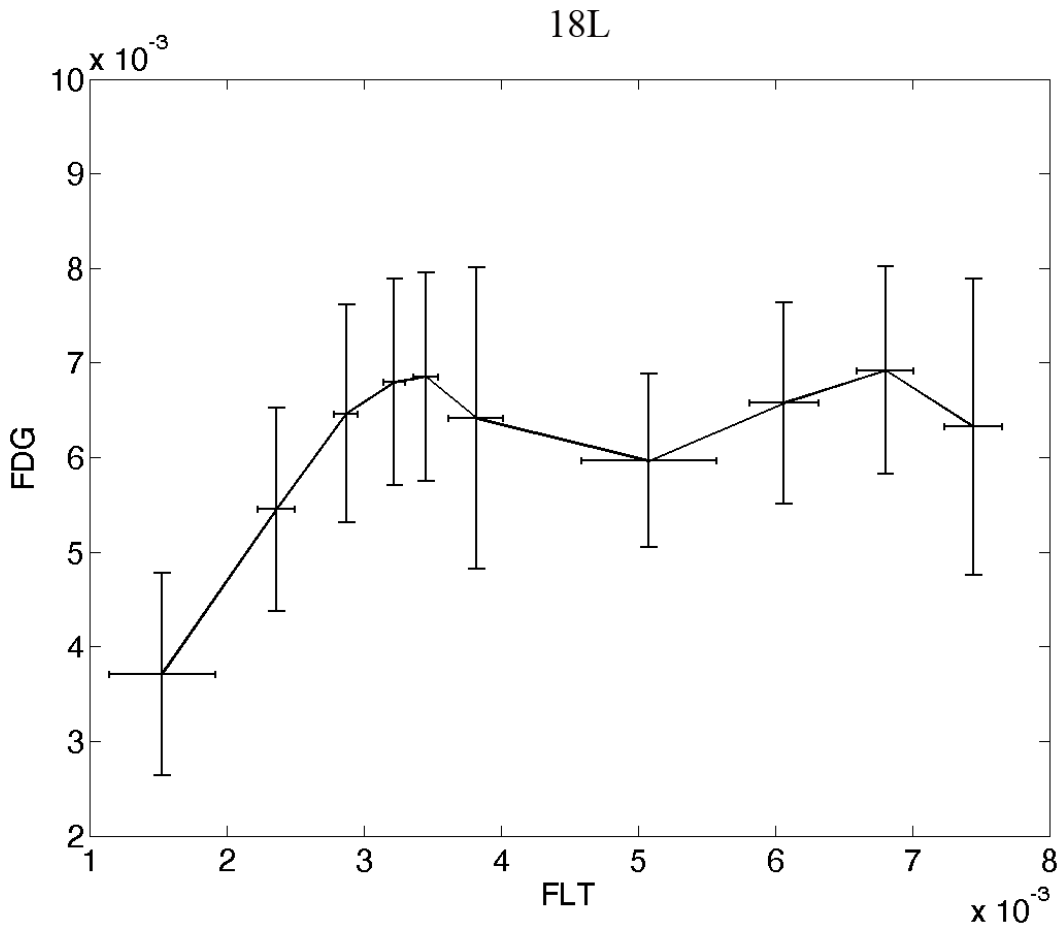

Figure 30: Binned graph showing the changes in FLT and FDG uptake in each voxel of the PET image for the SQ20B tumor 18L with a reconstructed voxel size of .77 mm

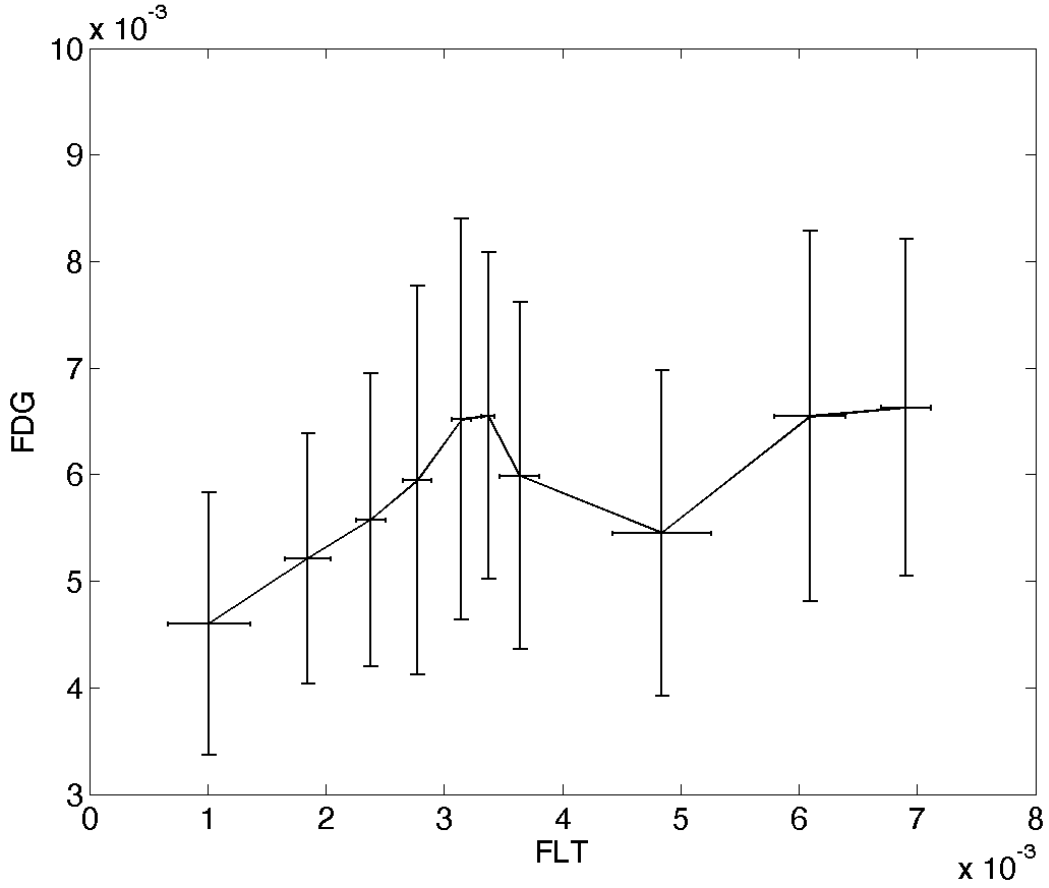

Figure 31: Binned graph showing the changes in FLT and FDG uptake in each voxel of the PET image for the SQ20B tumor 18R with a reconstructed voxel size of .77 mm

The voxel-by-voxel correlation analysis for Pinnacle 9 revealed an average correlation coefficient of .562 for FaDu tumors and .625 for SQ20B tumors. Unlike the Slicer 3 analysis, however, there was no statistical difference between the strengths of correlation between FaDu and SQ20B in the Pinnacle 9 analysis. The Dice similarity volumes overlap analysis revealed similar results to those seen in the voxel-by-voxel analyses. The Dice analysis revealed that there were significant areas on non-overlap between FDG and FLT depending on how you threshold the images. On average using a 50% threshold for both images yielded an overlap of approximately 77%. These results imply that the popular idea of auto-segmentation or auto-thresholding PET images to achieve an ROI to target could potentially cause a geometric miss of areas of highly proliferating cells and must be done with extreme caution as you go beyond

threshold values excluding more than approximately 25% of the data. An analysis of the volume under the synthetic "Dice surface" yielded average "volume" of 6171.82, an average volume of 5572.35 for FaDu tumors only and a volume of 6771.3 for SQ20B with no statistical difference between the two data sets.

Dice similarity surfaces images registered using Pinnacle 9 Demon's algorithm

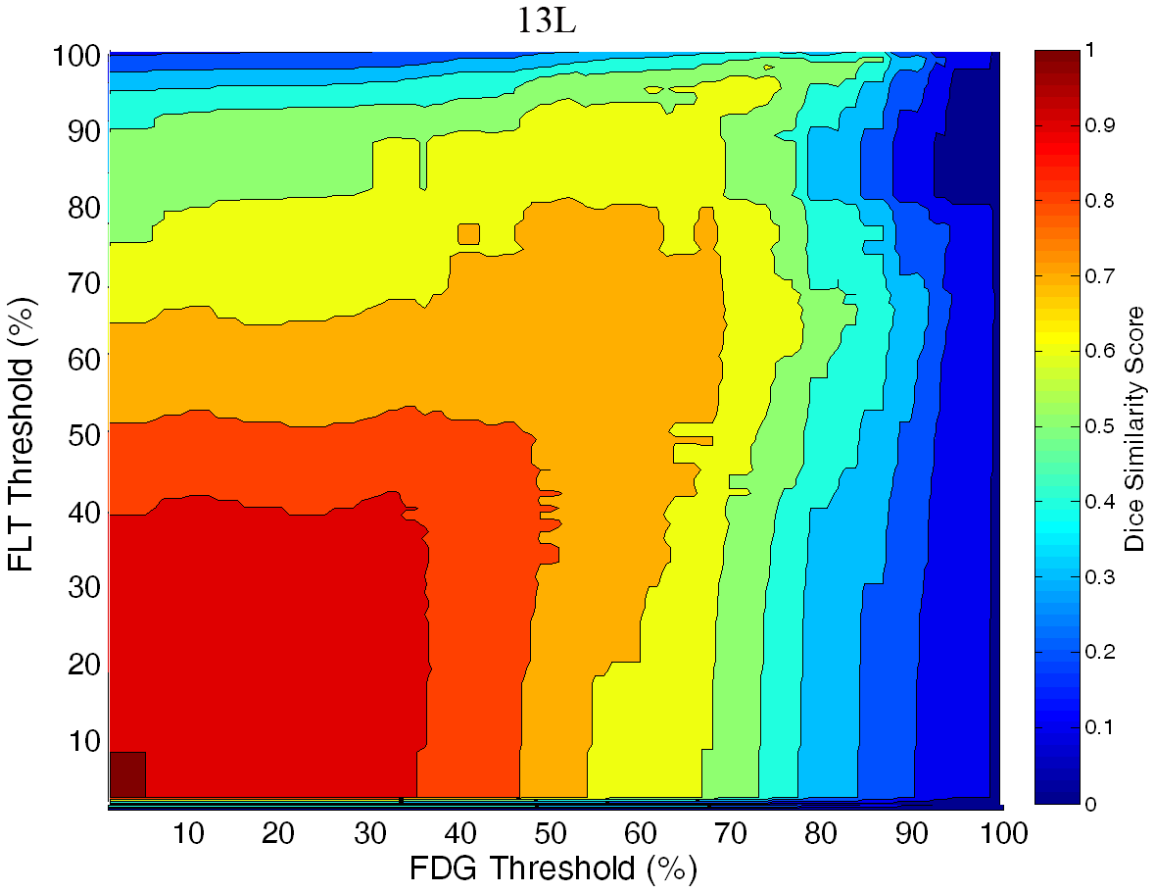

Figure 32: A plot showing the change the spatial overlap between FDG and FLT sub-volumes defined by thresholding PET images at different percentages of maximum intensity for FaDu tumor 13L

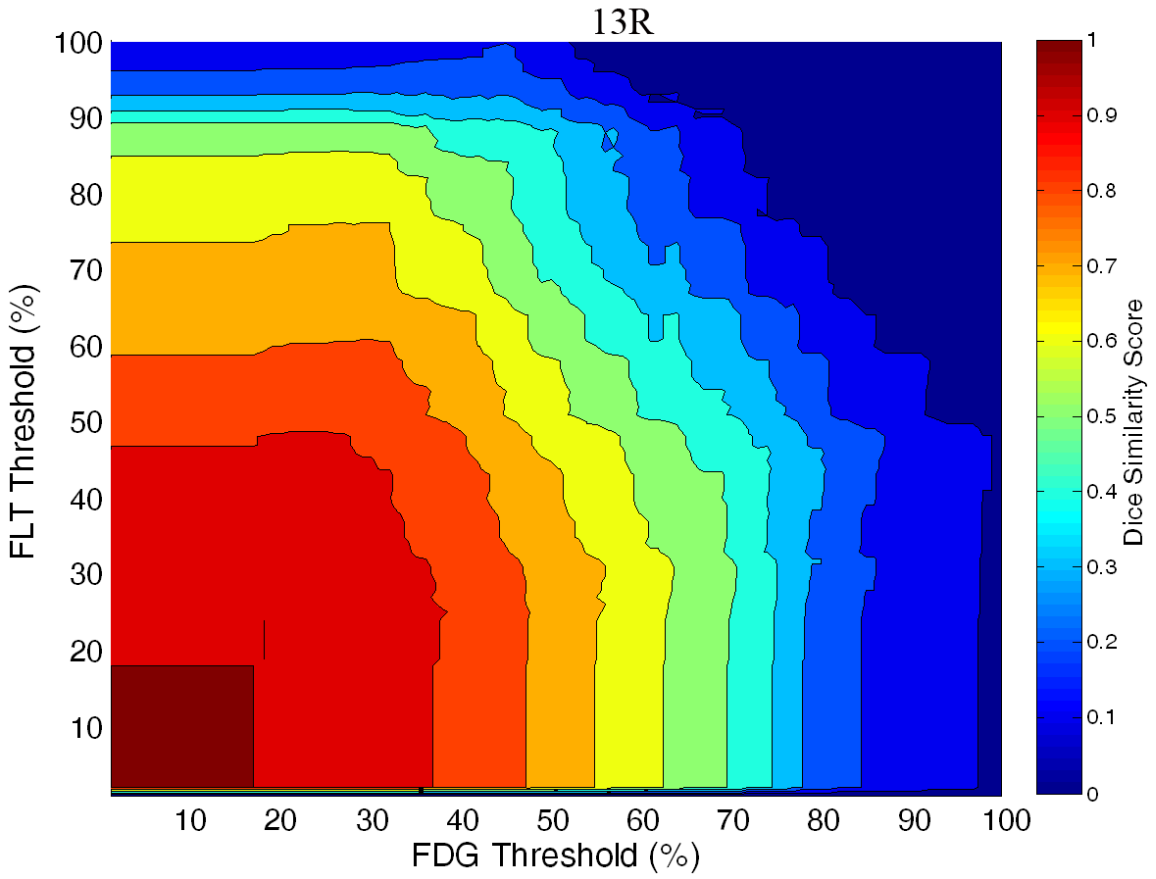

Figure 33: A plot showing the change the spatial overlap between FDG and FLT sub-volumes defined by thresholding PET images at different percentages of maximum intensity for FaDu tumor 13R

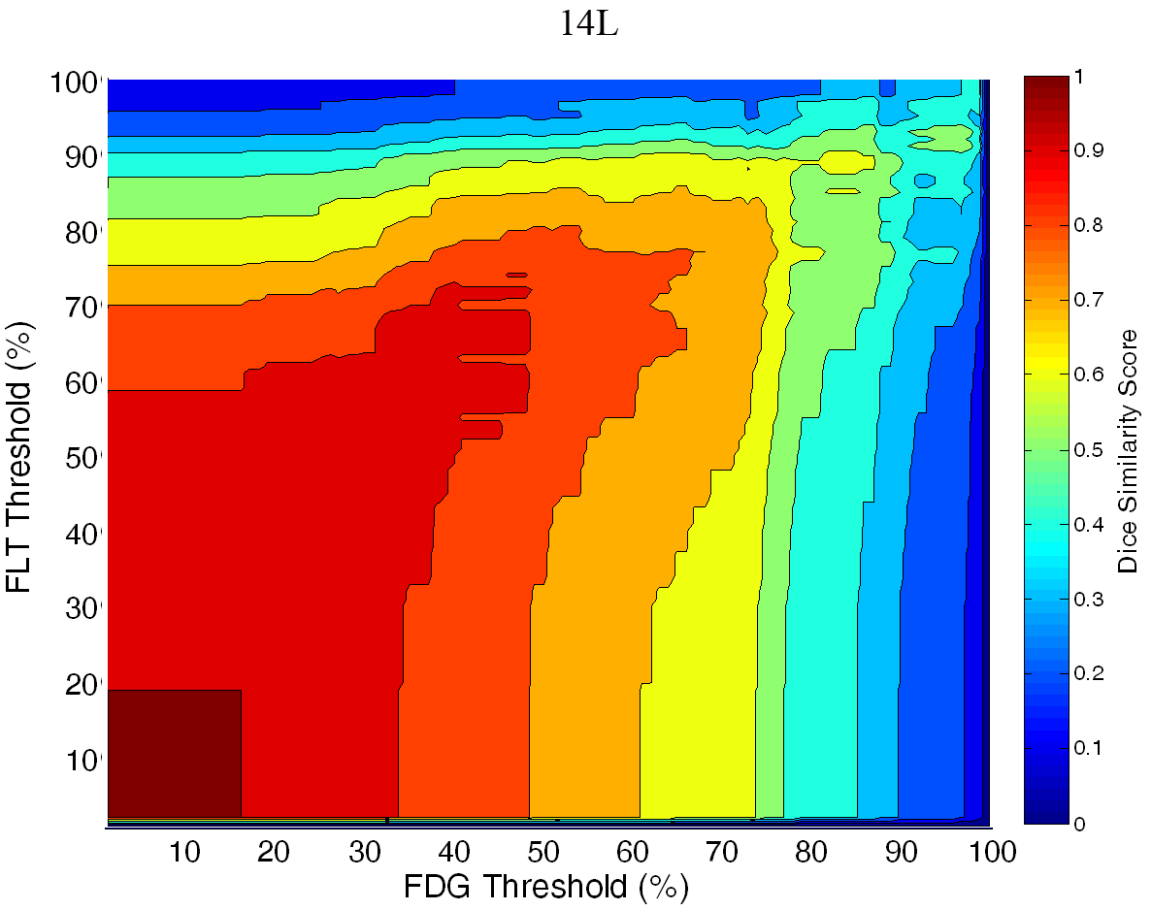

Figure 34: A plot showing the change the spatial overlap between FDG and FLT sub-volumes defined by thresholding PET images at different percentages of maximum intensity for FaDu tumor 14L

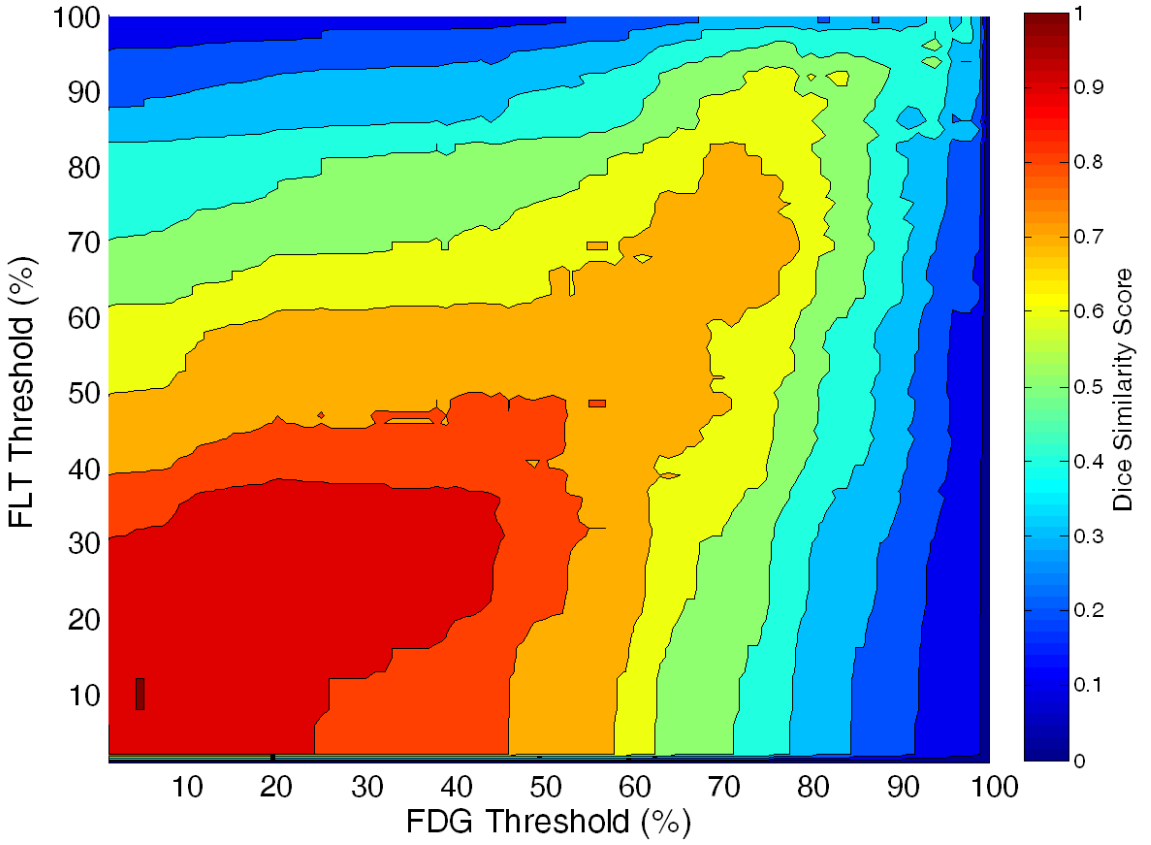

Figure 35: A plot showing the change the spatial overlap between FDG and FLT sub-volumes defined by thresholding PET images at different percentages of maximum intensity for FaDu tumor 14R

16L

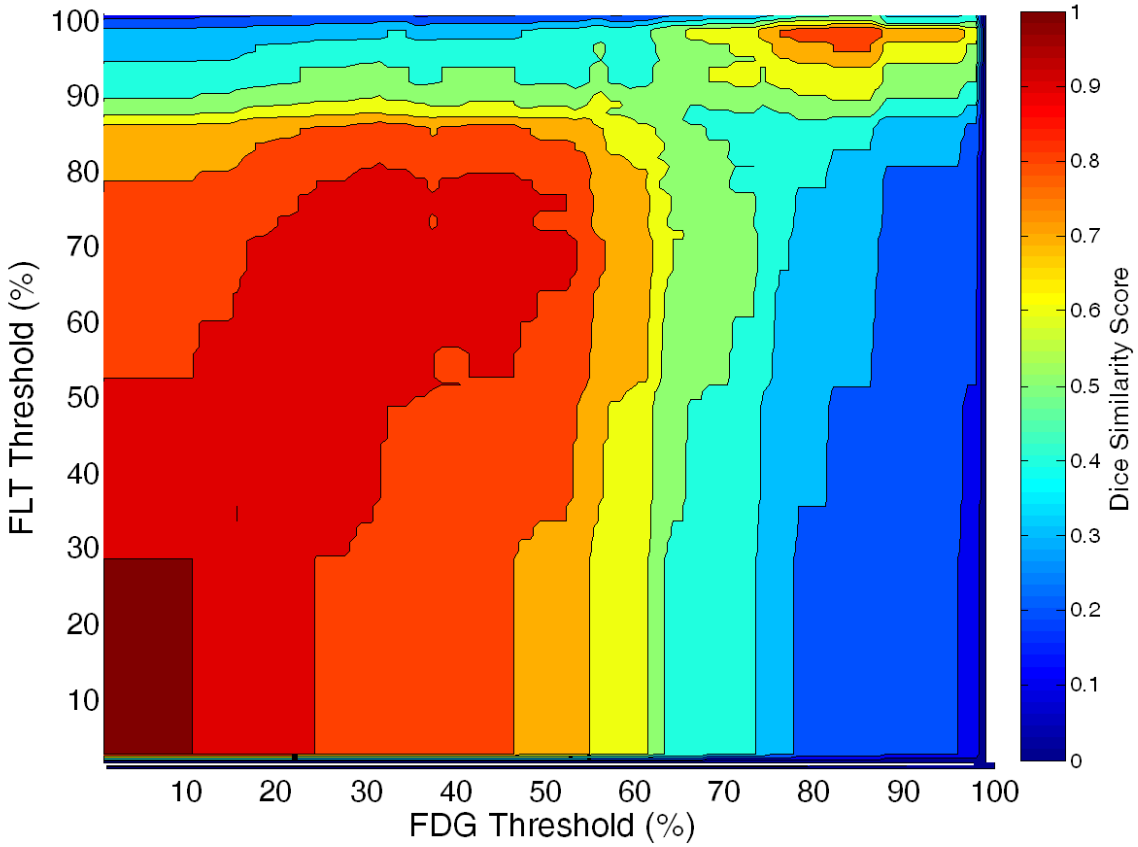

Figure 36: A plot showing the change the spatial overlap between FDG and FLT sub-volumes defined by thresholding PET images at different percentages of maximum intensity for SQ20B tumor 16L

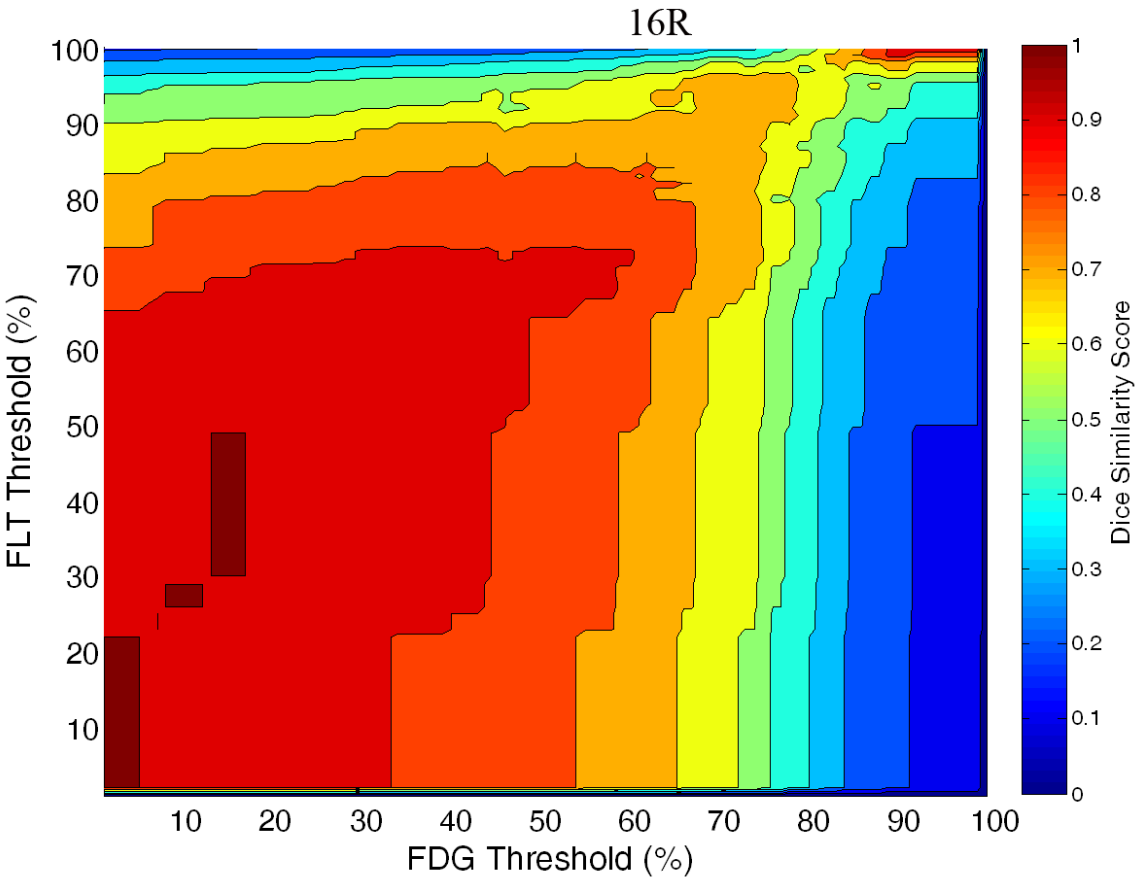

Figure 37: A plot showing the change the spatial overlap between FDG and FLT sub-volumes defined by thresholding PET images at different percentages of maximum intensity for SQ20B tumor 16R

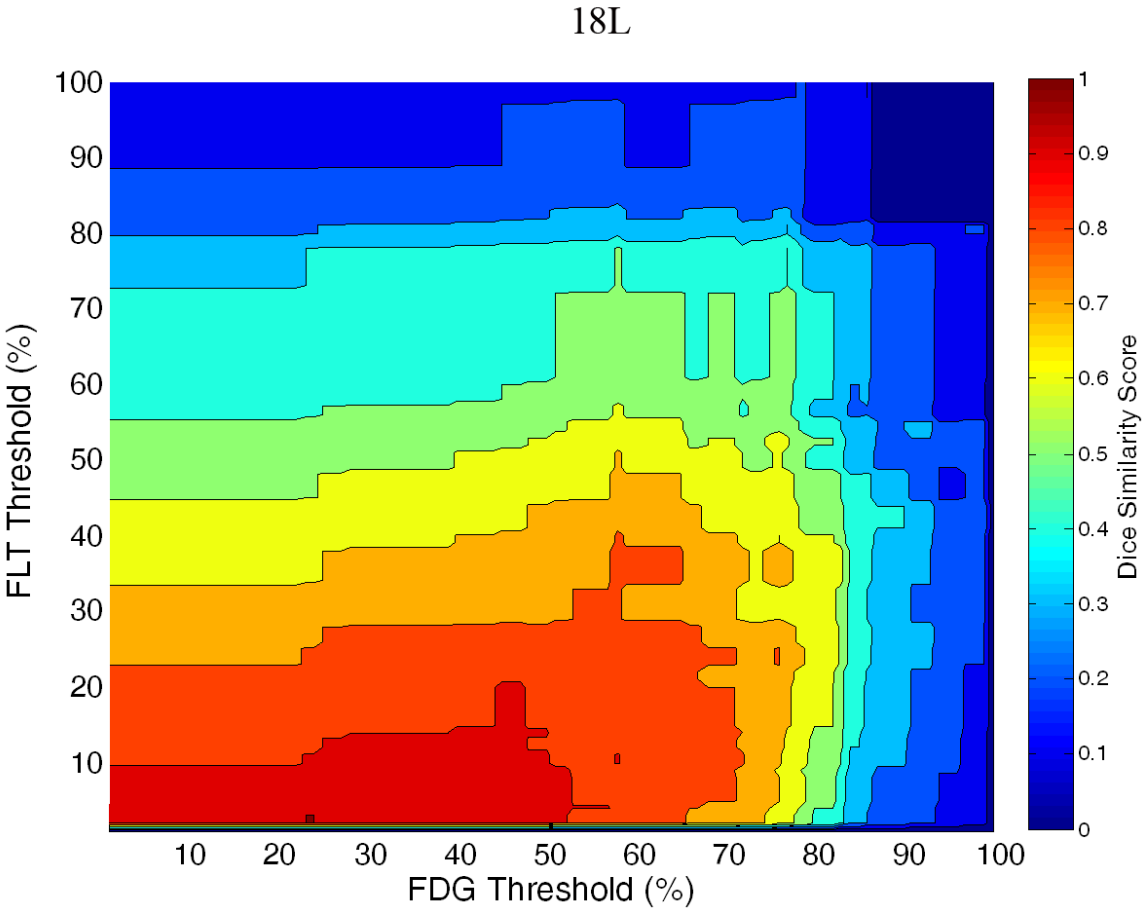

Figure 38: A plot showing the change the spatial overlap between FDG and FLT sub-volumes defined by thresholding PET images at different percentages of maximum intensity for SQ20B tumor 18L

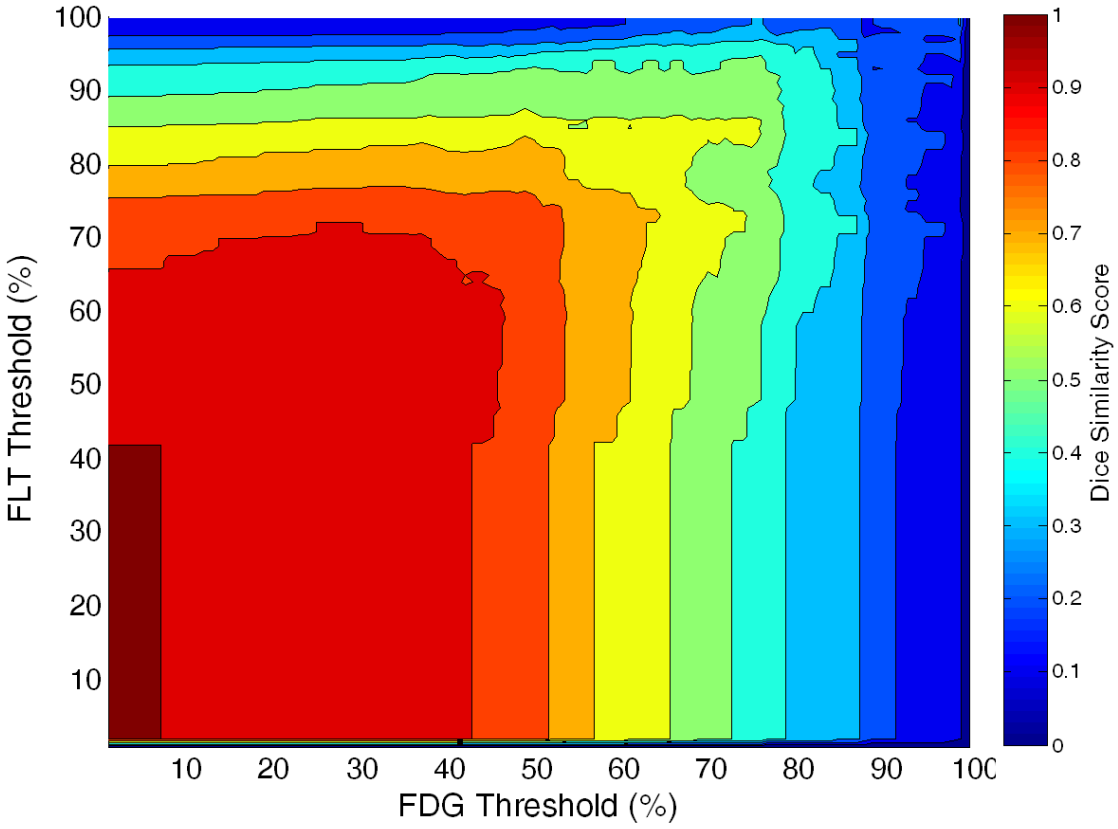

Figure 39: A plot showing the change the spatial overlap between FDG and FLT sub-volumes defined by thresholding PET images at different percentages of maximum intensity for SQ20B tumor 18R

The results of the Slicer analysis support the histological data while the results of the Pinnacle 9 analysis support the data but are not statistically significant. There are a number of reasons that the Pinnacle 9 analysis could differ. The generation and analysis of the various regions of interest, contours and image intensities were as objective as possible for the Slicer and Pinnacle analyses. All ROIs used for deformation were created using auto-thresholding for both methodologies. The tumor contours were generated manually using the CT data sets by the same researcher for both Pinnacle 9 and Slicer situations. The major differences between the two procedures involve the scaling of the images by Pinnacle 9 and the process of exporting and analyzing the images from both systems. In the case of the Slicer system, the images and

contours were saved in the same format and same resolutions each step of the way, this preserves the integrity of the user-generated contours across all steps. The deformed PET images produced using Pinnacle 9 are automatically scaled to the sizes of the CT image sets which are significantly larger and higher resolution than the original PET images. After export, these PET images and contours must be rescaled to match the original resolutions. The deformed image sets also do not include any rigid shifts applied by Pinnacle 9 once they are exported. This requires another registration after exportation of the image sets. In contrast, the Slicer results are all consistently kept at a single resolution and require no special exporting procedures. Pinnacle 9 also takes into account scaling factors in the PET images once they are loaded into the Pinnacle system. This scaling factor is produced by the small animal imaging device however, the two devices are designed by competing manufacturers and for different purposes and do not seem to handle scaling factors in the same manner.

The analysis of these image sets with a different algorithm verifies that the hypothesis that the results of comparing biological images are very sensitive to algorithm selection and image post processing. It is best to limit the amount of post processing of registered images as much as possible to prevent skewing of results. The B-spline registration available in Slicer registered all image sets successfully and produced the most accurate registrations.

Vita

Christopher Paul Bass was born on July 20th 1986 in Richmond, Virginia. He attended Atlee High School in Mechanicsville, Virginia where he graduated with honors in 2004. He graduated from Randolph-Macon College in 2008 with a Bachelors of Science in physics and a minor in mathematics. He interned in secondary education in 2008 with Hanover High School in Hanover, Virginia. Christopher held the positions of student liaison and secretary of the student chapter of the VCU medical physics society during his time at Virginia Commonwealth University. During this time he assisted in establishing a nuclear instrumentation course with Dr. Jeffery Siebers and conducted regular surveys of student approval of the program. He has been a speaker at the annual AAPM meeting for three consecutive years and has been a speaker at the Massey Cancer Center continuing education seminar.